Switching Control Strategies for the Robust Stabilization of a DC-DC Zeta Converter

Hafez Bin Sarkawi

Switching Control Strategies for the Robust Stabilization of a DC-DC Zeta Converter

Hafez Bin Sarkawi

Department of Applied Mathematics and Physics
Graduate School of Informatics
Kyoto University
Kyoto, Japan

August 2021

Doctoral dissertation
submitted to the Graduate School of Informatics, Kyoto University
in partial fulfillment of the requirement for the degree of
DOCTOR OF INFORMATICS
(Applied Mathematics and Physics)

Abstract

A DC-DC Zeta converter is a specific type of electrical circuit topology or configuration that transfers electrical power from the input to the output, producing a lower or higher direct-current (DC) output voltage than the DC input voltage. In practice, the input voltage and the load usually vary, either intentionally or otherwise; thus, a control subsystem is needed to ensure stable operation of the converter. In this thesis, to stabilize a DC-DC Zeta converter, we developed three switching control strategies based on two distinctive systems; an average-based system and a hybrid system.

For the average-based system control, a DC-DC Zeta converter under continuous conduction mode (CCM) operation is considered. We take into account the uncertain parameters, namely the input voltage and the load, and include the uncertainties of the Zeta converter model in a convex polytope formed by eight and 16 vertices. We rewrite a linear quadratic regulator (LQR) problem into a linear matrix inequality (LMI) representation; we term it an LMI-LQR approach, and solve the LMI-LQR problem for the eight and 16 vertices of the convex polytope model to find a state-feedback controller. On the other hand, for the hybrid system control, we derive two switching control strategies, each for the Zeta converter under CCM and discontinuous conduction mode (DCM) operations from a control Lyapunov function. For the CCM operation, the Zeta converter is modeled as a class of differential inclusions, and the local asymptotic stability of the operating point is established using LaSalle's invariance principle for this class of differential inclusions. Near the operating point, we allow the Lyapunov function to increase and bound it by a threshold that is related to the prescribed switching frequency. Later, we extend the hybrid system control to a three-mode system, instead of two-mode for the CCM operation, and formulate a switching control strategy for the Zeta converter in DCM operation.

As a result, both the average-based and the hybrid system controllers are robust and able to handle large input voltage and load perturbations. Compared to the conventional LQR control, under the non-nominal condition, our LMI-LQR control can stabilize the output voltage, whereas the conventional LQR control is unable to bring back the state-trajectory to its operating point. However, in CCM operation, it is shown that the hybrid system control is more robust than the LMI-LQR control, especially if the perturbations are outside the predefined uncertain parameters value. Likewise, for

the DCM operation, our hybrid system control can stabilize the output voltage while maintaining the desired switching frequency requires for the DCM operation.

Acknowledgment

First and foremost, my highest gratitude goes to my supervisor, *Professor Dr. Yoshito Ohta*, for his willingness to accept me as a research student back in 2015, and later as a PhD student in 2016. His tremendous guidance and support, as well as invaluable input and comment throughout my PhD journey, will always be remembered. Without a doubt, I will never be where I am now without his excellent supervision.

I want to express my appreciation to *Professor Dr. Nobuo Yamashita* and *Professor Dr. Toshiyuki Ohtsuka,* where both are the professors at the Graduate School of Informatics, Kyoto University, for serving as the committee members of my dissertation. Their highly useful comment and recommendation help me improve the dissertation.

I would like to thank the Control System Theory laboratory secretaries, *Ms. Atsuko Kimura* who has helped me a lot with my official and personal matters, and *Ms. Nobuko Nishikawa* who has helped me prepared the important documents for the dissertation matter.

Special thanks to the *Malaysia Ministry of Education* (*Department of Higher Education*) and *Universiti Teknikal Malaysia Melaka* (*UTeM*) for the much needed financial support. Without them, it would be impossible for me to further studies at this prestigious Kyoto University.

My deepest and most emotional thanks go to my beloved wife *Noridah Mohd Ridzuan*, and my four adorable children *Aqeela Hafez*, *Ashraf Hafez*, *Arsyad Hafez*, and *Amsyar Hafez*, for always being there beside me, during the up-and-down of my PhD and life journeys. To my father *Sarkawi Afendi*, mother *Norjanah Pitani*, father-in-law *Mohd Ridzuan Salleh*, and mother-in-law *Markonah Abu*, thanks for the prayers and best wishes for me to complete the PhD study.

Last but not least, to the other family members, friends, and those who have made contributions, either directly or indirectly, my sincerest thanks go to all.

Contents

List of Figures

List of Tables

Chapter 1

Introduction

1.1 Motivation

The invention of a bipolar junction transistor (BJT) in 1947 by Shockley [1] marks the era of a transistor. A transistor milestone was achieved when field-effect transistor (FET) was invented in 1952 [2] and subsequently, in 1960, a metal-oxide-semiconductor FET (MOSFET) was invented [3], which has desirable properties such as incredible efficiency, fast switching speed, and high input resistance. These properties attracted the use of switching circuits in power applications, and as a consequence, power converters, whose main functions are achieved by the switching property of MOSFET, have developed rapidly in recent years. A power converter is essentially an electrical or electro-mechanical device that can convert electrical energy. Roughly speaking, a power converter can be found almost everywhere, whether in a small or large device, as long as the device consists of an electronic circuit.

A global climate problem has prompted many countries to reduce their carbon footprint and dependency on fossil fuels and, in turn, use renewable energy sources [4]. Among those renewable energy sources, solar energy has become the most commonly used due to its wide reachability and abundance [5]. Although solar energy is clean and theoretically infinite, as with other renewable energy sources, in nature, it is uncertain. The solar irradiance fluctuates especially during a cloudy or rainy day, which in turn fluctuates the energy harvested from the solar photovoltaic (PV) cell [6]. More so, if a fixed load resistance is used, the generated operating point (voltage and current) are varied, depending on the irradiance levels, as shown in Figure 1.1.

Battery-powered portable electronic devices such as a smartphone, laptop, LED light, power bank, etc., will have their power drains over time. Essentially, a charger that is connected to an alternating-current (AC) outlet is used to charge the battery of

these devices. However, the problem arises, for example, for outdoor activities that lasted for a few days or more, without any access to electricity from the grid. To tackle this power issue, an off-grid, solar energy harvesting system is considered as shown in Figure 1.2 [7]. As can be seen in the figure, the solar energy harvesting system consists of three components; a solar energy harvester, a power management system and a DC load. Since solar energy fluctuates, the problems are arisen as following

- the generated voltage from the PV panel is not constant,
- too high of the voltage will damage the battery, whereas if the voltage is too low, then the battery cannot be charged.

Therefore, to protect the battery from the PV solar panel output voltage fluctuation, a control subsystem for the DC-DC converter needs to be deployed.

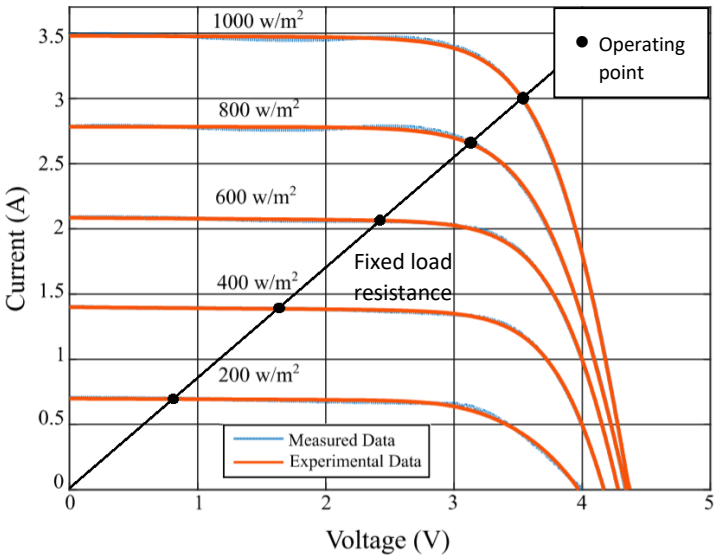

Figure 1.1: I-V curve of a solar cell and operating points for fixed load resistance [6].

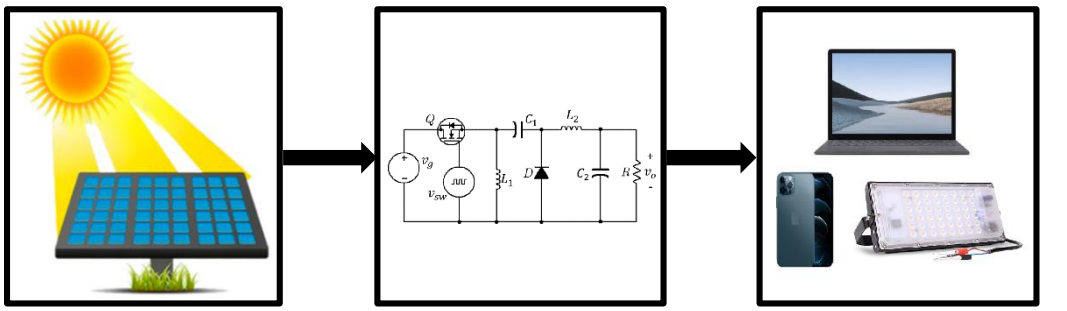

Figure 1.2: Solar energy harvesting system with a DC load.

Motivated by the need to produce a stable and constant output voltage for the solar battery charging application, in this thesis, we propose the switching control strategies and applied the methods to a DC-DC Zeta converter.

1.2 Introduction to DC-DC Converter

A DC-DC converter is a power converter circuit where the input is direct-current (DC) voltage and the output is also DC voltage. Two types of DC-DC converters exist, categorized by a conversion manner; linear or switching. As the name implies, a linear converter uses a linear component, typically a resistive load, to regulate the output voltage. Besides that, it is also named a series converter due to the series arrangement of the control elements between the input and output. The linear converter has a simple circuit configuration, and since no switching involves, the noise is low. The downsides, however, are more obvious, such as poor efficiency, considerable heat generation, and the output voltage is always lower than the input voltage. These three weaknesses of the linear converter can be overcome by a switching type DC-DC converter. In general, the main functions of a switching DC-DC converter are [3]

- to convert a DC input voltage into a DC output voltage either at a lower or higher level,
- to regulate and stabilize (with the help of a control subsystem) the DC output voltage against the input voltage and the load variations,
- to reduce the ripple in the DC output voltage to the below-required level.

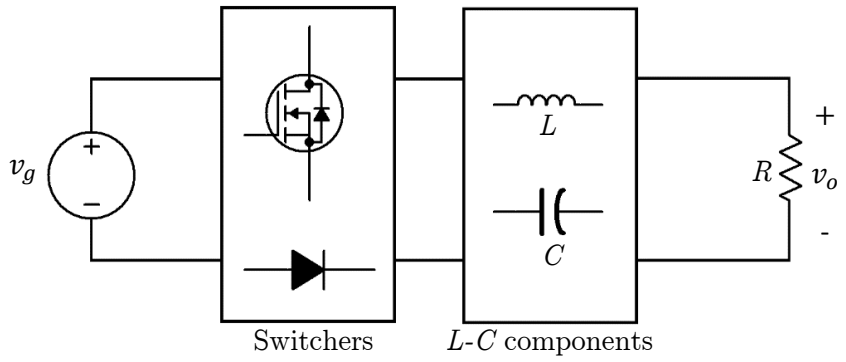

Figure 1.3: A switching-type DC-DC converter block diagram.

A switching DC-DC converter consists of the switchers (MOSFET(s) and/or diode), an inductor(s) L, a capacitor(s) C, and a load R, as shown in Figure 1.3. The switching converter delivers the power from the input to the output by using the switcher

components. More specifically, the converter converts the DC input voltage v_g by temporarily storing the input energy into the energy storage elements such as an inductor and a capacitor and then releasing it to the output at a lower or higher DC voltage level. Since the converter is on-and-off, back-and-forth, less power is used for the voltage conversion process, and thus it offers high efficiency and good thermal performance compared to a linear converter. However, the switching converter has shortcomings such as complicated design and produces high-frequency noise, which can cause electromagnetic interference (EMI) to the nearby device [8]. Because the switching converter benefits outweigh the shortfalls, it is chosen in this thesis.

1.2.1 Mode of Operation

Since the switchers exhibit on-off behaviors, the DC-DC converter can be modeled as a multi-mode system. For any DC-DC converter, because it consists of a MOSFET and a diode, theoretically, the model has up to four modes. However, due to the natural circuit constraint imposed by the electronic component, not all modes are feasible in practice. To be specific, a condition where both MOSFET and diode are on-state cannot be visited. Depending on the inductor's current status, the converter can be modeled as either a two-mode or a three-mode system.

A DC-DC converter is modeled as a two-mode system if it operates under continuous conduction mode (CCM). In a two-mode system, the back-and-forth transition between mode 1 and mode 2 is governed by exogenous switching as depicted in Figure 1.4. Exogenous switching occurs when an external switching signal is applied to a MOSFET. In practice, most converters are designed to operate under CCM operation. The converter is said to be in CCM operation if the inductor current flows continuously as can be seen in Figure 1.5. Note that a cycle, known as a switching period T_{sw}, is the duration taken by the consecutive transitions of mode 1 and mode 2, and it is inversely proportional to the switching frequency $f = \frac{1}{T_{sw}}$. The inductor current ripple, which is the difference between the maximum and minimum inductor current, is denoted as $i_{L\max}$ and $i_{L\min}$, respectively, is proportionally related to the switching frequency. Although it is desirable to have a low inductor current ripple, a high switching frequency is required, which in turn produces high switching loss and reduces the converter efficiency. Therefore, it is important to strike a balance between converter performance and efficiency. In practice, the switching frequency for CCM operation is chosen somewhere from $50\,\text{kHz}$ to $400\,\text{kHz}$.

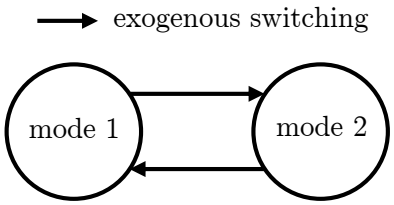

Figure 1.4: Two-mode transitions in CCM operation.

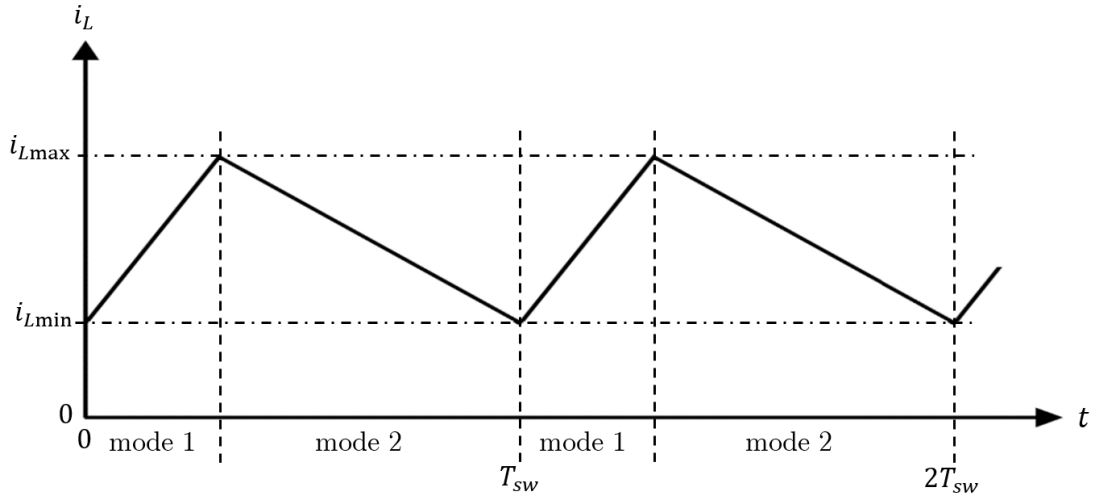

Figure 1.5: Approximate steady-state inductor current waveform in CCM operation.

In certain situations, especially where higher efficiency is required, a DC-DC converter operating in discontinuous conduction mode (DCM) is chosen. This is because the DCM operation generally occurs at a low switching frequency, thus less switching loss. Other than that, under light load (small load current) conditions, or for a specific application such as power factor correction, the DCM operation is also typically deployed. In DCM operation, the converter can be modeled by a three-mode system, as illustrated in Figure 1.6. The transitions from mode 1 to mode 2 and from mode 3 to mode 1 are performed by exogenous switching, while endogenous switching takes place for mode 2 to mode 3 transitions. Endogenous switching is a result of a diode turning on or off due to forward or reverse biased conditions, respectively. Figure 1.7 shows the inductor current waveform in DCM operation. As the discontinuous name suggests, a discontinuity in the inductor current in mode 3 can be seen where the inductor current is zero. The switching frequency in DCM operation is calculated from the inverse of the time taken for the transitions of mode 1-mode 2-mode 3. The switching frequency in DCM operation is relatively low, typically in the range of $20\,\text{kHz}$ to $40\,\text{kHz}$, and thus high inductor current ripple can be expected compared to CCM operation.

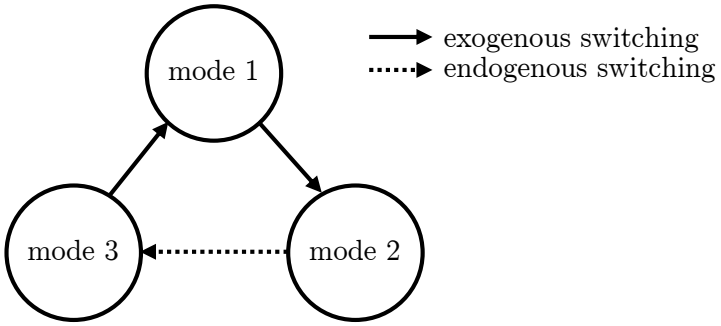

Figure 1.6: Three-mode transitions in DCM operation.

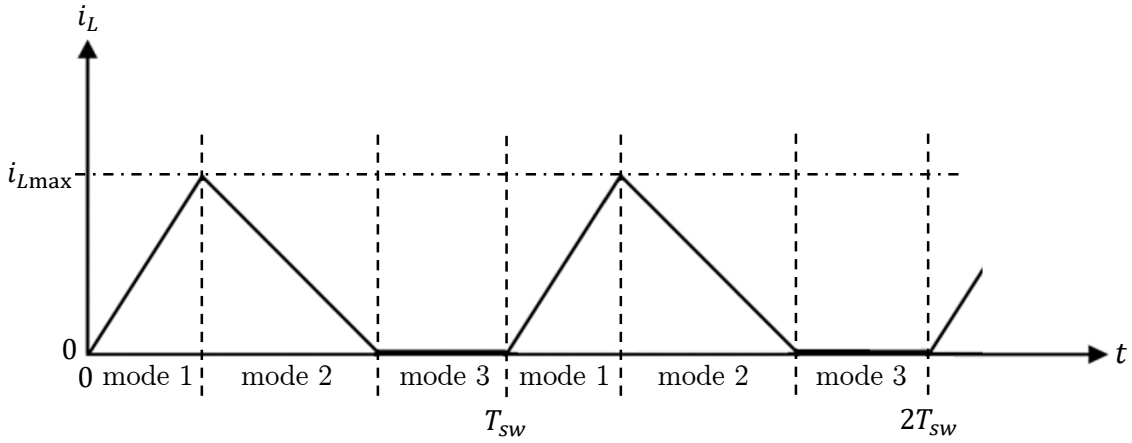

Figure 1.7: Approximate steady-state inductor current waveform in DCM operation.

1.2.2 Circuit Topology

A DC-DC converter circuit can be classified into two categories; isolated and non-isolated. The existence of a transformer to physically and electrically separate a DC path between the input and the output of the converter is what differs the former from the latter. Although the isolated DC-DC converters provide better load protection, the cost, size, and efficiency are inferiors compared to the non-isolated converters, making them less attractive. On the other hand, the well-known circuit configurations for the non-isolated converters are the buck [9], the boost [10], the buck-boost [11], the Cuk [12], and the Zeta [13] topologies, and will be discussed next.

Figure 1.8 shows the topology of a DC-DC buck converter. Buck converter is also known as a step-down converter because it is used to reduce the input voltage. The converter consists of a MOSFET Q, a diode D, an inductor L, a capacitor C, and a load R. Notice that a switching signal v_{sw} is applied to the MOSFET to turn it on or off. The equivalent circuits for the buck converter in CCM and DCM operation are given in

Figure 1.9 and Figure 1.10, respectively. The basic operation principles of the buck converter are as follows. When the MOSFET is turned on, the positive terminal of the input voltage v_g is connected to the diode and the inductor, thus supplies energy to the inductor. Since the diode is reverse biased, it appears as an open circuit. The equivalent circuit for this condition, denoted as mode 1, is shown in Figure 1.9(a) and Figure 1.10(a). When the MOSFET is turned off, the input voltage is disconnected, and the inductor reacts and maintains current flow to the load, therefore reducing the inductor's energy. At the same time, a current flow through the diode and turned on the diode, and hence, the mode 2 equivalent circuit is generated, as depicted in Figure 1.9(b) and Figure 1.10(b). Over time, if the MOSFET remains off-state, the energy in the inductor eventually drains out, and the inductor current becomes zero. This makes the diode off, and the mode 3 equivalent circuit in Figure 1.10(c) is produced.

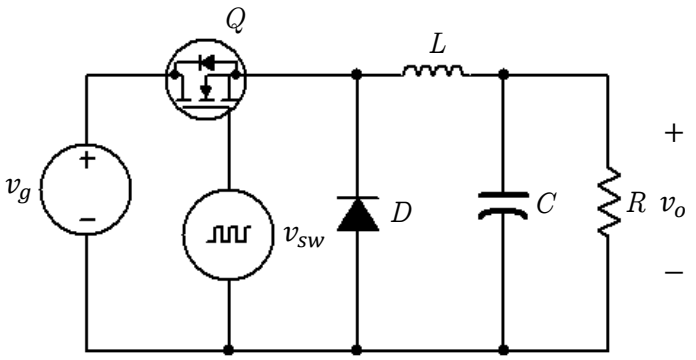

Figure 1.8: DC-DC buck converter circuit.

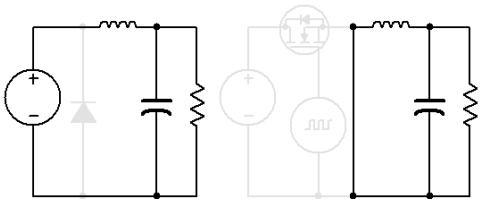

(a) (b)

Figure 1.9: Equivalent buck converter circuits in CCM operation for (a) mode 1, and (b) mode 2.

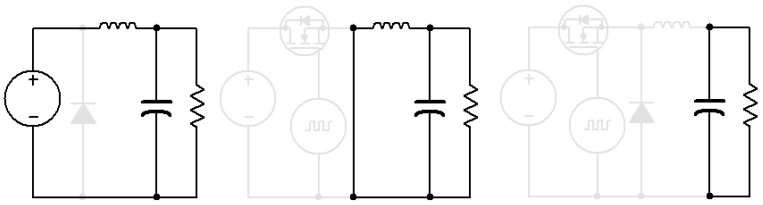

(a) (b) (c)

Figure 1.10: Equivalent buck converter circuits in DCM operation for (a) mode 1, (b) mode 2, and (c) mode 3.

On the other hand, a DC-DC boost converter, synonymously known as a step-up converter, is capable of producing an output voltage that is higher than the input voltage. Similar to a buck converter, the boost converter is made of a MOSFET Q, a diode D, an inductor L, a capacitor C, and a load R, as shown in Figure 1.11. The CCM and DCM operation equivalent circuits for the boost converter are illustrated in Figure 1.12 and Figure 1.13, respectively. In Figure 1.12(a) and Figure 1.13(a), denoted as mode 1, the MOSFET is on-state, allowing the input voltage to store energy into the inductor while turned the diode off since its positive terminal is grounded. When the MOSFET is off-state, the diode is turned on and the energy from the inductor is released to the load to maintain the load current. The mode 2 equivalent circuit is depicted in Figure 1.12(b) and Figure 1.13(b). Eventually, the inductor current is fully discharged. As no current flows inside the diode, it becomes an open circuit, and the equivalent circuit for mode 3 is shown in Figure 1.13(c).

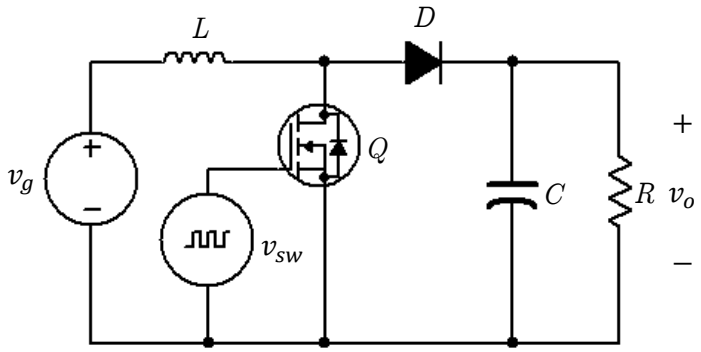

Figure 1.11: DC-DC boost converter circuit.

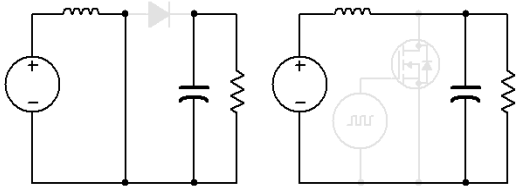

Figure 1.12: Equivalent boost converter circuit in CCM operation for (a) mode 1, and (b) mode 2.

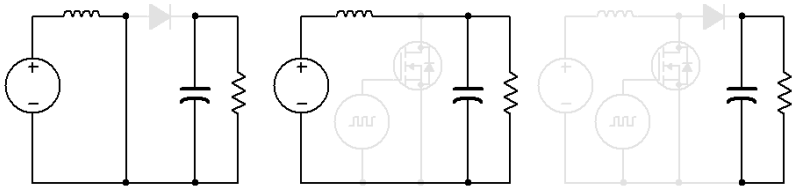

Figure 1.13: Equivalent boost converter circuit in DCM operation for (a) mode 1, (b) mode 2, and (c) mode 3.

As the name implies, a converter with buck-boost topology inherits the functionality of the buck and boost converters, and thus, the output voltage can either be lower or higher than the input voltage. However, the output voltage is in reverse polarity compared to the input voltage. As illustrated in Figure 1.14, the electronic components for the buck-boost converter are identical to the buck and the boost converters, which comprise of a MOSFET Q, a diode D, an inductor L, a capacitor C, and a load R. In general, because the buck-boost converter is fundamentally a combination of the buck and boost converters, it shares the common operation principles of the two converters. Specifically, the operation principles of a buck-boost converter for mode 1, mode 2, and mode 3 are similar to mode 1 of a boost, mode 2 of a buck, and mode 3 of a buck or boost converter, respectively. The CCM and DCM operation equivalent circuits for the buck-boost converter are presented in Figure 1.15 and Figure 1.16, respectively.

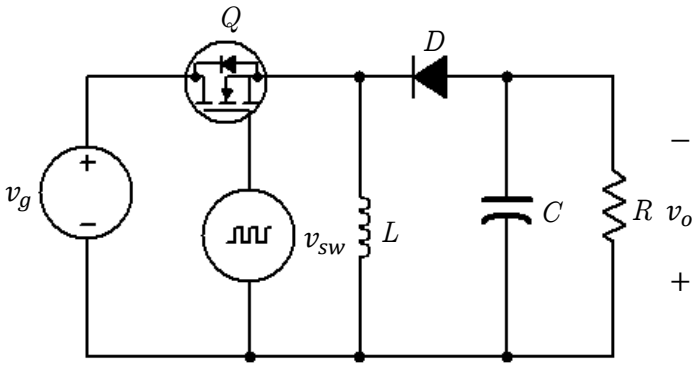

Figure 1.14: DC-DC buck-boost converter circuit.

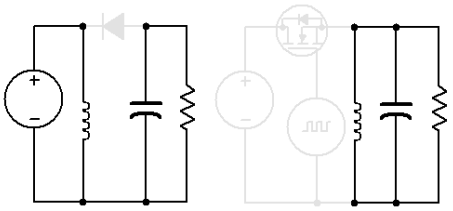

Figure 1.15: Equivalent buck-boost converter circuits in CCM operation for (a) mode 1, and (b) mode 2.

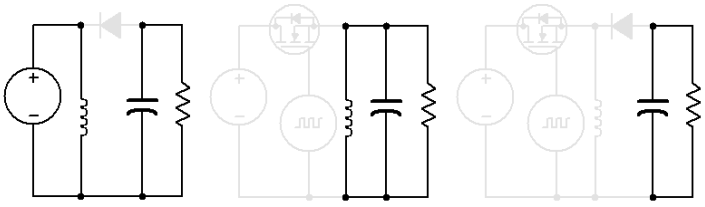

Figure 1.16: Equivalent buck-boost converter circuits in DCM operation for (a) mode 1, (b) mode 2, and (c) mode 3.

The Cuk topology in Figure 1.17 shares similarities with a buck-boost converter, capable of stepping the input voltage down and up, having reverse output voltage polarity. Component-wise, the Cuk converter has an additional inductor and capacitor compared with the three converters mentioned above. Under mode 1 (see Figure 1.18(a) and Figure 1.19(a)), when the MOSFET is on-state, an inductor L_1 is charged by the input voltage, and since the positive terminal of the capacitor C_1 is grounded, the diode is in reverse biased, and thus it appears as an open circuit. When the MOSFET is turned off during mode 2 (Figure 1.18(b) and Figure 1.19(b)), the inductor L_1 tries to maintain the current flows to the load by releasing its energy. The diode is turned on, and the currents in the inductors L_1 and L_2 flow through the diode. The current in the inductor L_1 is decreased over time, and eventually, the current flows through the diode is zero, thus switched off the diode, and the mode 3 equivalent circuit is given in Figure 1.19(c).

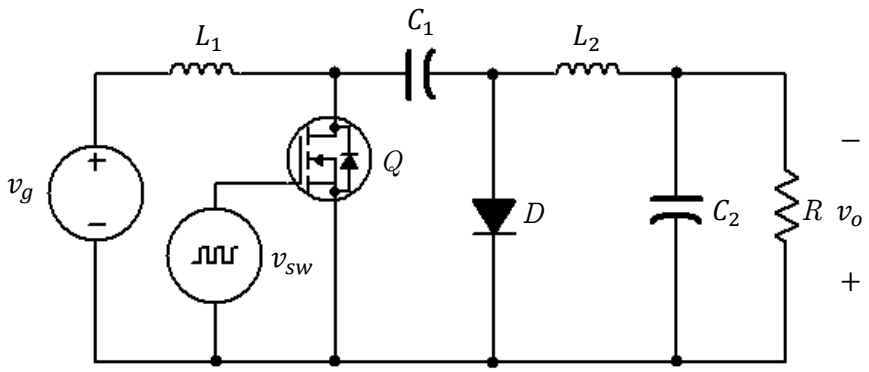

Figure 1.17: DC-DC Cuk converter circuit.

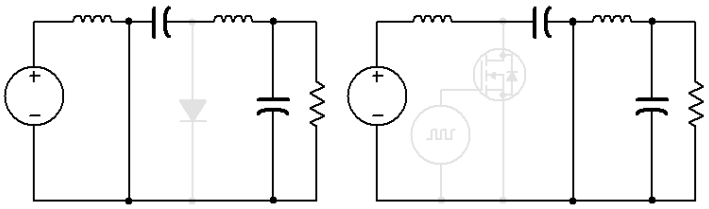

(a) (b)

Figure 1.18: Equivalent Cuk converter circuits in CCM operation for (a) mode 1, and (b) mode 2.

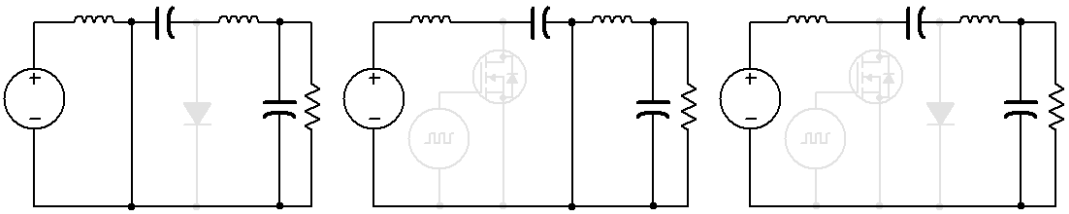

(a) (b) (c)

Figure 1.19: Equivalent Cuk converter circuits in DCM operation for (a) mode 1, (b) mode 2, and (c) mode 3.

Lastly, Figure 1.20 shows a DC-DC Zeta converter. A Zeta topology shares two common attributes to a Cuk; equal number of components count and the ability to increase or decrease the input voltage. The output voltage of a Zeta converter is in phase with the input voltage. In the following, the operation principles of a Zeta converter are explained. During the MOSFET on-state, both inductors L_1 and L_2 are being charged. Because the cathode of the diode has a higher voltage than the anode, the diode is reverse biased, and thus it is off-state. The mode 1 equivalent circuit is shown in Figure 1.21(a) and Figure 1.22(a). For mode 2, the MOSFET is turned off, and the currents in both inductors L_1 and L_2 are discharged to the load to maintain the load current. The diode is forced to be turned on to provide a return path for the inductors' currents, as depicted in Figure 1.21(b) and Figure 1.22(b). Over time, the inductors' currents are depleted such that the current flows through the diode is zero; thereby, the diode becomes off-state. The equivalent circuit, denoted as mode 3, is depicted in Figure 1.22(c).

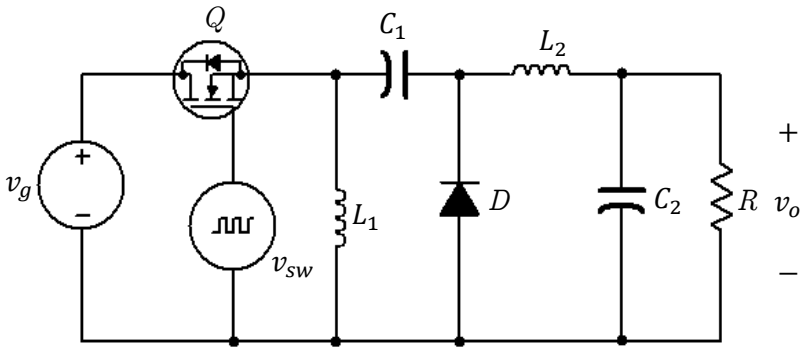

Figure 1.20: DC-DC Zeta converter circuit.

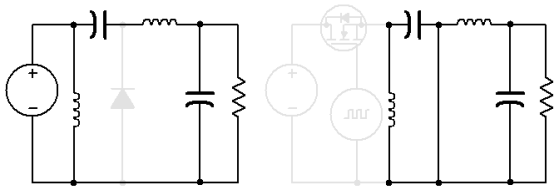

(a) (b)

Figure 1.21: Equivalent Zeta converter circuits in CCM operation for (a) mode 1, and (b) mode 2.

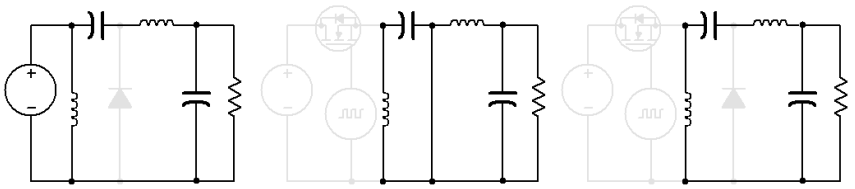

(a) (b) (c)

Figure 1.22: Equivalent Zeta converter circuits in DCM operation for (a) mode 1, (b) mode 2, and (c) mode 3.

To summarize, the five DC-DC converter topologies are compared in Table 1.1. Component-wise, each topology has a MOSFET and a diode as the switchers, and the Cuk and the Zeta topologies have two inductors and two capacitors as compared to one inductor and one capacitor for the other three topologies. In terms of functionality, the buck-boost, the Cuk, and the Zeta can do both step-down and step-up operation, whereas the buck and the boost can do step-down and step-up only, respectively. The output voltage is in phase with the input voltage for the buck, the boost, and the Zeta topologies, while the buck-boost and the Cuk topologies have negative polarity. Note that the output voltage ripple and the input-output isolation, which have not been explicitly explained before, are added for a broader comparison. As can be seen, the buck, the Cuk, and the Zeta topologies relatively have low output voltage ripple compared to the boost and buck-boost topologies. Besides that, out of the five topologies, only the buck, the buck-boost, and the Zeta topologies have natural input-output voltage isolation.

Table 1.1: Comparison of DC-DC converter topologies characteristics.

Topology	**Operation**	**Switcher**	***L-C* component**	**Output voltage**	**Output voltage ripple**	**Input-output isolation**
Buck	Step-down	1 MOSFET, 1 diode	1 inductor, 1 capacitor	Positive	Low	Yes
Boost	Step-up	1 MOSFET, 1 diode	1 inductor, 1 capacitor	Positive	High	No
Buck-boost	Step-down & step-up	1 MOSFET, 1 diode	1 inductor, 1 capacitor	Negative	High	Yes
Cuk	Step-down & step-up	1 MOSFET, 1 diode	2 inductors, 2 capacitors	Negative	Low	No
Zeta	Step-down & step-up	1 MOSFET, 1 diode	2 inductors, 2 capacitors	Positive	Low	Yes

In this thesis, we choose the DC-DC Zeta converter due to the following justifications. The ability to do both step-up and step-down operation allows the Zeta converter to operate in a wider range [14]. Even though the buck-boost and the Cuk topologies offer similar functionality, the Zeta topology has superior electrical characteristics compared with the two. Namely, the Zeta converter produces a relatively

lower output voltage ripple compared with the buck-boost converter [15], which implies a lower switching frequency operation, and in turn, higher efficiency can be achieved. Compared to the Cuk converter, the Zeta converter has a positive output voltage, and thus no output voltage polarity conversion is needed. Moreover, the Zeta converter has a natural DC input-to-output voltage isolation, which helps to prevent unwanted signals or noise from being transmitted from the input to the output.

1.3 DC-DC Converter Control

The DC-DC converter requires a control subsystem that regulates the output voltage to follow a reference voltage. Typically, a control subsystem is designed through feedback to produce a closed-loop system. The advantages of a closed-loop DC-DC converter are

- the converter can be stabilized even with uncertain parameters,
- the output voltage can be regulated, and the reference voltage can be tracked,
- the input voltage and the load variations can be compensated,
- the converter's transient responses can be improved.

Feedback control can be divided into two types; positive feedback and negative feedback. As the name suggests, a positive feedback control adds the reference voltage and the output voltage, while in negative feedback control, the reference voltage and the output values are subtracted, and the latter is commonly used since it is more stable than the former. In Section 1.2.1, we have shown that a DC-DC converter is made of a two- or three-mode system under CCM or DCM operation, respectively. To design the feedback control, the two- and three-mode systems are represented either by the average-based or hybrid system.

1.3.1 Average-based System Control Approach

In an average-based system, a DC-DC converter dynamics of the two- and three-mode systems are averaged over a switching period. The control of the system can be realized through output- or state-feedback, and two design methods are usually considered for the controller; classical and modern control. For a classical control method, the analysis is carried out in the frequency domain using Laplace transform, where the converter is assumed to be a second-order and single variable, and higher-order system responses and multivariable effects are ignored. For a modern control method, the converter is represented as a set of first-order differential equations defined using state variables. In both control methods, most of the effort is spent on finding a control law to calculate the control duty ratio d_d.

Considering CCM operation, as depicted in Figure 1.23, a control duty ratio d_d is used to modulate and generate a pulse width modulation (PWM) switching signal v_{sw} in the average-based system control method. Specifically, the control duty ratio is compared with a sawtooth signal v_{saw} having a fixed frequency and a maximum amplitude V_M [16]. If $d_d \geq v_{saw}$, then the switching signal level is high (logic "1"); otherwise, the switching signal level is low (logic "0"). The durations for the high and low levels of the switching signal are denoted as t_{on} and t_{off}, respectively. The ratio of t_{on} over t_{on} plus t_{off} is known as the duty ratio $d = \frac{t_{on}}{t_{on}+t_{off}}$. It is worth emphasizing that the control duty ratio is instrumental in regulating the output voltage of a DC-DC converter; any changes to the control duty ratio will change the output voltage level.

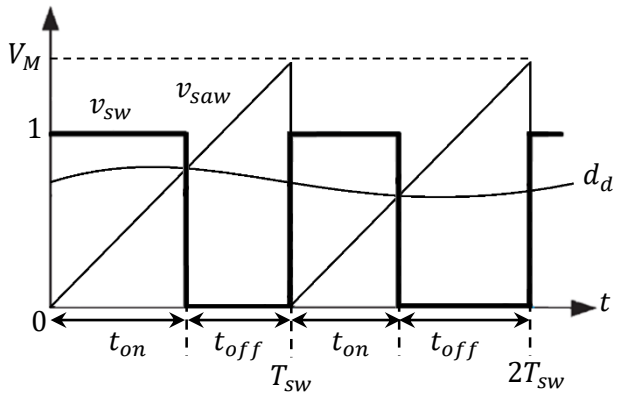

Figure 1.23: Average-based system control switching signal v_{sw} generation in CCM operation.

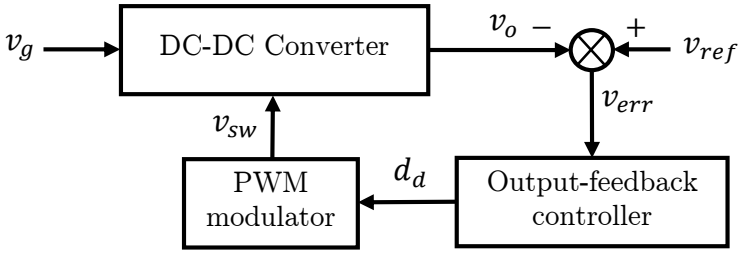

Figure 1.24: Block diagram of DC-DC converter with output-feedback control.

Figure 1.24 shows the implementation diagram of an output-feedback control applied to a DC-DC converter. As can be seen, only one sensor is required to measure the output voltage v_o, which is why this type of feedback is popular in practice. The measured output voltage is subtracted with the reference voltage v_{ref}, and the error voltage v_{err} is compensated by the output-feedback controller, and a control duty ratio

d_d is produced. As a result, a switching signal v_{sw} is produced based on the control duty ratio PWM modulation. Subsequently, based on the duty ratio d of the switching signal, the output voltage of the DC-DC converter will be adjusted accordingly.

On the other hand, the block diagram for a DC-DC converter using a state-feedback control is depicted in Figure 1.25. Typically, it is more expensive to implement this type of controller since more sensors are required to measure the state variables x of the converter. Nevertheless, since richer dynamics are captured by the state variables, the performance of the converter can be easily manipulated, thus makes the controller design attractive.

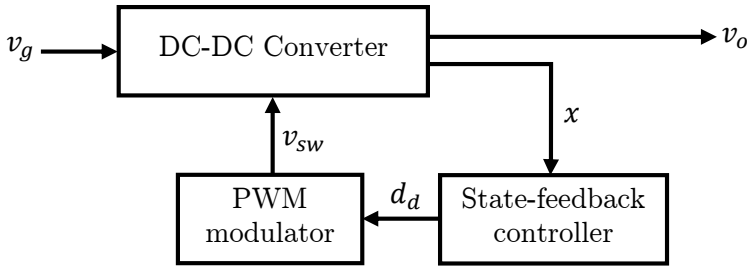

Figure 1.25: Block diagram of DC-DC converter with state-feedback control.

In the average-based system control, a DC-DC converter is modeled based on a state-space averaged (SSA) approach and the corresponding linearized approximate model. Moreover, from the small-signal SSA model, various control techniques have been adopted to investigate the dynamic responses of the converter. In the following, the common controller's design utilizing the output-feedback and state-feedback are presented.

Consider a DC-DC converter small-signal SSA model as following

$$\begin{aligned} \frac{d\tilde{x}}{dt} &= A\tilde{x} + B\tilde{u} + B_d\tilde{u}_d, \\ \tilde{y} &= C\tilde{x}, \end{aligned} \tag{1.1}$$

where $\tilde{x}$, $\tilde{y}$, $\tilde{u}$, and $\tilde{u}_d$ are the state vector, the output, the input, and the control input small-signals, respectively, while A, B, B_d, and C are the averaged matrices of the system, the input, the control input, and the output, respectively.

For the output-feedback control, the frequency domain method is typically used to find the controller for a DC-DC converter. In the steady-state condition, the differential

is zero. Taking Laplace transform and assuming zero initial condition, (1.1) can be rewritten as

$$\tilde{x}(s) = (sI - A)^{-1}B\tilde{u}(s) + (sI - A)^{-1}B_d\tilde{u}_d(s),$$
$$\tilde{y}(s) = -CA^{-1}B_d\tilde{u}_d(s). \tag{1.2}$$

From (1.2), the following four transfer functions are generated

1. State vector-to-input transfer function $G_{xu}(s)$

$$G_{xu}(s) = \frac{\tilde{x}(s)}{\tilde{u}(s)}\Big|_{\tilde{u}_d(s)=0} = (sI - A)^{-1}B. \tag{1.3}$$

2. State vector-to-control input transfer function $G_{xd}(s)$

$$G_{xd}(s) = \frac{\tilde{x}(s)}{\tilde{u}_d(s)}\Big|_{\tilde{u}(s)=0} = (sI - A)^{-1}B_d. \tag{1.4}$$

3. Output-to-input transfer function $G_{yu}(s)$

$$G_{yu}(s) = \frac{\tilde{y}(s)}{\tilde{u}(s)}\Big|_{\tilde{u}_d(s)=0} = C(sI - A)^{-1}B. \tag{1.5}$$

4. Output-to-control input transfer function $G_{yd}(s)$

$$G_{yd}(s) = \frac{\tilde{y}(s)}{\tilde{u}_d(s)}\Big|_{\tilde{u}(s)=0} = C(sI - A)^{-1}B_d. \tag{1.6}$$

Notice that (1.5) is actually a steady-state gain of the converter. Moreover, (1.5) and (1.6) are typically used in the design part of the output-feedback controller.

As for the state-feedback control framework, the control law for the state-feedback is given by

$$\tilde{u}_d = -K\tilde{x}, \tag{1.7}$$

where K is the state-feedback vector gain.

Consider zero external input $(\tilde{u} = 0)$. Then, substituting (1.7) into (1.1), one gets

$$\frac{d\tilde{x}}{dt} = (A - B_dK)\tilde{x}. \tag{1.8}$$

The origin of the closed-loop state-feedback control system (1.8) is asymptotically stable if and only if the matrix $A - B_d K$ is Hurwitz. Thus, the state-feedback stabilization problem is a problem of designing a vector gain K to assign the eigenvalues of $A - B_d K$ in the open left-half complex plane. It is worth highlighting that the eigenvalues of $A - B_d K$ can be arbitrarily assigned, as long as the pair (A, B_d) is controllable. In the case of some eigenvalues of A are not controllable, stabilization is still possible, provided that the uncontrollable eigenvalues have negative real parts. Furthermore, let P and Q be positive-definite symmetric matrices; then, a Lyapunov equation for the closed-loop system is given as follows:

$$P(A - B_d K) + (A - B_d K)^T P = -Q. \tag{1.9}$$

Assumed $(A - B_d K)$ is Hurwitz, then the Lyapunov equation (1.9) has a unique positive definite solution [17]. Furthermore, the quadratic function

$$V(x) = x^T P x, \tag{1.10}$$

is a Lyapunov function for the closed-loop system in the neighborhood of the origin.

1.3.2 Hybrid System Control Approach

A DC-DC converter, by its nature, presents hybrid behavior. Hybrid system modeling is a suitable modeling technique to capture both continuous and discrete dynamics of the converter. In essence, under hybrid system control, continuous dynamics of the modes and a switching rule are combined to determine which mode is active. The hybrid DC-DC converter control can be realized by

$$\frac{dx}{dt} = f_{\gamma_k}(x, u), \tag{1.11}$$

where x is the state, u is an external input assumed to be constant, and γ_k is the switching function corresponds to discrete mode k, where k =1,2 and k =1,2,3 are for CCM and DCM operations, respectively. Only one mode is active at any instant time and it is governed by a switching function that is commonly state-dependent.

Figure 1.26 depicts the transitions of the modes in a hybrid DC-DC converter control framework. Each discrete mode k has associated continuous dynamics f_{γ_k}, and it should be emphasized that the continuous and discrete dynamics coexist and interact with each other. For i, j = 1,2,3, the control problem is to determine the switching conditions G_{ij}

which cause a transition from mode i to mode j while satisfying the system requirements on control. In other words, under current mode k, once the continuous state-dependent switching function γ_k reaches a threshold Ξ_k, a decision can be made whether to jump to the next discrete mode. Notice that endogenous switching occurs for a transition from mode 2 to mode 3. Thus, G_{23} can simply be defined as $i_L = 0$ (or $i_{L1} + i_{L2} = 0$) for a converter with one inductor (or two inductors). The switching conditions for all possible mode transitions are defined as follows:

$$G_{12}: \gamma_1 > \Xi_1, \;\; G_{21}: \gamma_2 > \Xi_2, \;\; G_{23}: i_L = 0, \;\; G_{31}: \gamma_3 > \Xi_3. \tag{1.12}$$

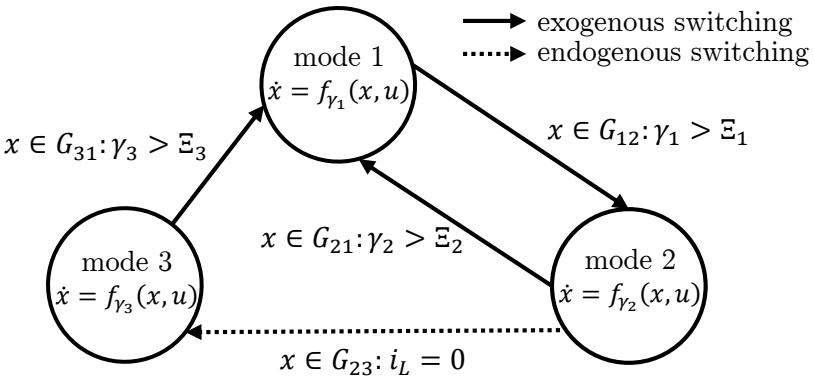

Figure 1.26: Hybrid DC-DC converter control diagram.

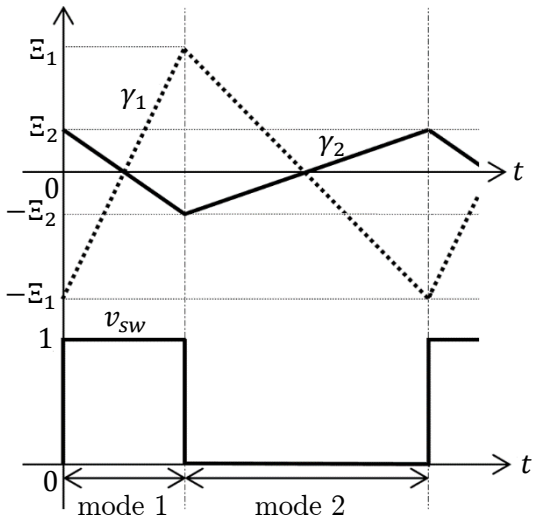

Figure 1.27: Hybrid system control switching signal v_{sw} generation in CCM operation.

Figure 1.27 shows an example of the switching signal v_{sw} generation of the hybrid system control in CCM operation. Under current active discrete mode 1, the v_{sw} is logic "1". Under mode 1, the corresponding switching function γ_1 increases while γ_2 (switching function corresponds to mode 2) decreases. When γ_1 reaches the threshold Ξ_1, then the v_{sw} changes to logic "0", which activates discrete mode 2. Under mode 2, γ_2 increases while γ_1 decreases. When γ_2 reaches Ξ_2, v_{sw} changes back to logic "1", thus mode 1 is active, and the process keeps repeating.

It is worth highlighting that the switching function γ_k is usually a function of state-trajectory under mode k. The threshold Ξ_k on the other hand, is a non-negative constant $\Xi_k \geq 0$, and is typically the difference of the state-trajectory from the operating point x^* at the switching instance from mode k to the next discrete mode. In other words, the threshold is a reflection of the state ripple size. Having said that, zero threshold value implies zero state ripple, however, arbitrarily fast switching may occur which is undesirable in practice. To alleviate this problem, a positive threshold should be chosen, and this is termed spatial regularization [33]. Furthermore, the threshold can be determined from the control system requirements such as voltage regulation or switching frequency constraints.

The hybrid system control strategies for a DC-DC converter in CCM and DCM operation can be realized as follows.

Hybrid System Control Strategy for CCM Operation

- If the system is operating at mode 1 and reaches $\gamma_1(\Xi_1)$, then it switches to mode 2.
- If the system is operating at mode 2 and reaches $\gamma_2(\Xi_2)$, then it switches to mode 1.

Hybrid System Control Strategy for DCM Operation

- If the system is operating at mode 1 and reaches $\gamma_1(\Xi_1)$, then it switches to mode 2.
- If the system is operating at mode 2 and reaches $i_L = 0$, then it switches to mode 3.
- If the system is operating at mode 2 and reaches $\gamma_3(\Xi_3)$, then it switches to mode 1.

Typically, a hybrid system control strategy can be derived based on two methods; state waveform analysis and Lyapunov function candidate. Using a DC-DC boost converter operating under CCM as an example, a hybrid system control strategy based on the state waveform analysis borrowed from [18] will be discussed first.

Under CCM operation, the two-mode system of a boost converter are given by

$$\begin{aligned} \frac{dx}{dt} &= A_1 x + B_1, \\ \frac{dx}{dt} &= A_2 x + B_2, \end{aligned} \tag{1.13}$$

where

$$\begin{aligned} A_1 &= \begin{bmatrix} 0 & 0 \\ 0 & -\frac{1}{CR} \end{bmatrix}, \quad B_1 = \begin{bmatrix} \frac{v_g}{L} \\ 0 \end{bmatrix}, \\ A_2 &= \begin{bmatrix} 0 & -\frac{1}{L} \\ \frac{1}{C} & -\frac{1}{CR} \end{bmatrix}, \quad B_2 = \begin{bmatrix} \frac{v_g}{L} \\ 0 \end{bmatrix}. \end{aligned} \tag{1.14}$$

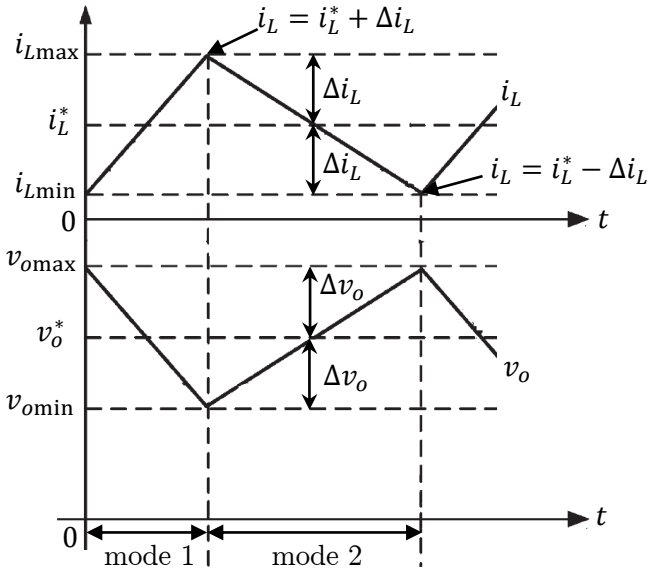

Figure 1.28: Approximate steady-state inductor current i_L (top) and output voltage v_o (bottom) waveforms of a boost converter in CCM operation.

Based on the observation of the inductor current i_L in Figure 1.28, it can be seen that the transitions from mode 1 to mode 2 and mode 2 to mode 1 of the boost converter

occur when the inductor current reach $i_L = i_L^* + \Delta i_L$ and $i_L = i_L^* - \Delta i_L$, respectively. Following this observation, the switching functions γ_1 and γ_2, and the thresholds Ξ_1 and Ξ_1 are defined by

$$\gamma_1 = i_L, \quad \gamma_2 = -i_L, \quad \Xi_1 = i_L^* + \Delta i_L, \quad \Xi_2 = i_L^* - \Delta i_L, \tag{1.15}$$

respectively.

The performance specification is defined by the size of the output voltage ripple Δv_o. As such, the inductor current ripple Δi_L in (1.15) is written as a function of Δv_o to achieve the output voltage constraint. For that, the waveforms in Figure 1.28 and the dynamics (1.12) are analyzed, and it is found that

$$\Delta i_L = \frac{CRv_g}{Lv_{ref}} \Delta v_o. \tag{1.16}$$

Additionally, by equating the converter input and output power, and solving for the average inductor current i_L^*, one gets [18]

$$i_L^* = \frac{v_{ref}^2}{Rv_g}. \tag{1.17}$$

Thus, the *Hybrid System Control Strategy for CCM Operation* for the state waveform analysis can be executed by applying parameters in (1.15) to (1.17). As a result, the prescribed output voltage regulation can be achieved. Moreover, a similar procedure can be used to produce a switching control strategy for DCM operation.

For a Lyapunov-based hybrid system control strategy, first, consider the following two-mode and there-mode systems in (1.18) and (1.19), respectively.

$$\begin{aligned} \frac{dx}{dt} &= A_1 x + B_1 u, \\ \frac{dx}{dt} &= A_2 x + B_2 u, \end{aligned} \tag{1.18}$$

$$\begin{aligned} \frac{dx}{dt} &= A_1 x + B_1 u, \\ \frac{dx}{dt} &= A_2 x + B_2 u, \\ \frac{dx}{dt} &= A_3 x + B_3 u. \end{aligned} \tag{1.19}$$

Choose a candidate of Lyapunov function

$$V(x) = (x - x^*)^T P(x - x^*), \tag{1.20}$$

where P is a positive definite matrix and x^* is the operating point.

Under CCM operation, the derivatives of $V(x)$ (1.20) along the trajectories of (1.18) for mode 1 and mode 2 are given by (1.21) and (1.22), respectively.

$$\begin{aligned}\gamma_1(x) &:= \frac{\partial V}{\partial x}(A_1 x + B_1 u_0) \\ &= (x - x^*)^T (PA_1 + A_1^T P)(x - x^*) + 2(A_1 x^* + B_1 u_0)^T P(x - x^*),\end{aligned} \tag{1.21}$$

$$\begin{aligned}\gamma_2(x) &:= \frac{\partial V}{\partial x}(A_2 x + B_2 u_0) \\ &= (x - x^*)^T (PA_2 + A_2^T P)(x - x^*) + 2(A_2 x^* + B_2 u_0)^T P(x - x^*),\end{aligned} \tag{1.22}$$

Whereas under DCM operation, the derivatives of $V(x)$ (1.20) along the trajectories of (1.19) for mode 1, and mode 3 are given by

$$\begin{aligned}\gamma_1(x) &:= \frac{\partial V}{\partial x}(A_1 x + B_1 u_0) \\ &= (x - x^*)^T (PA_1 + A_1^T P)(x - x^*) + 2(A_1 x^* + B_1 u_0)^T P(x - x^*),\end{aligned} \tag{1.23}$$

$$\begin{aligned}\gamma_3(x) &:= \frac{\partial V}{\partial x}(A_3 x + B_3 u_0) \\ &= (x - x^*)^T (PA_2 + A_2^T P)(x - x^*) + 2(A_2 x^* + B_2 u_0)^T P(x - x^*).\end{aligned} \tag{1.24}$$

respectively.

Notice that under the DCM operation, γ_2 is omitted because the transition from mode 2 to mode 3 is endogenous.

By applying the switching functions in (1.21) and (1.22), and (1.23) and (1.24), in the *Hybrid System Control Strategy for CCM Operation* and *Hybrid System Control Strategy for DCM Operation*, respectively, the system state-trajectory is driven along the fastest converging direction while guaranteeing the asymptotic stability of the system. Note that the thresholds Ξ_1, Ξ_2 and Ξ_3 have not been explicitly defined. They will be detailed out in Chapter 4 and Chapter 5.

1.3.3 Summary

A summary of the main differences of both average-based and hybrid system controls of a DC-DC converter is given in Table 1.2.

Table 1.2: Comparison between average-based and hybrid system control.

	Average-based system control	**Hybrid system control**
System model	SSA model (with approximation)	Hybrid model (no approximation)
Controller design	Compensator parameter selection	Switching function definition
MOSFET switching	PWM modulation	Direct switching (no modulation)
Switching frequency	Fixed	Adjustable

In terms of system modeling, the two modes or the three modes of the converter are averaged to produce an approximate single system under the average-based system, by using a state-space averaging (SSA) approach and corresponding linear approximation. For the hybrid system model, each mode is treated individually, and all the dynamics are captured without any approximation. In the controller design, for the average-based system control, the parameter of the compensator needs to be selected, and usually tuning is required to find the best parameter. Whereas for the hybrid system control, the switching functions need to be defined. To turned the MOSFET on and off, a modulated PWM switching signal is used by the average-based system control, while direct MOSFET switching is used in the hybrid system control. As a result, the switching frequency produced by the former is fixed while the latter is adjustable.

1.4 Previous Studies

Some researchers have studied the control problem of a DC-DC converter using the average-based system control method. Meanwhile, no work was reported under the hybrid system control framework to stabilize a Zeta converter, whose dynamic equation is described by a fourth-order system. Therefore, this section will review some studies

on the average-based Zeta converter control and the hybrid control of DC-DC converters described by second-order systems, such as a buck, a boost, and a buck-boost converters.

1.4.1 Conventional Zeta Converter Control

In [19, 20], the authors have proposed a proportional-integral (PI) to control a DC-DC Zeta converter. The authors have modeled the Zeta converter by taking into account the internal resistance of the two inductors and two capacitors. The PI controller was found from the control-to-output transfer function, considering crossover frequency of 10 kHz [19] and 12 kHz [20] and phase margin of at least 45 degrees. To reduce the magnitude of output voltage overshoot, a derivative term was added, and a proportional-integral-derivative (PID) controller designed using the Ziegler–Nichols method was presented in [21]. Moreover, an optimal version of the PID controller based on ant colony optimization (ACO) and a reduced-order Zeta converter model was proposed in [22]. Generally, although the PI and the PID controllers produce fast output voltage responses, the effort by the control duty ratio is high. To compensate for the variations of the load and the internal resistances of the inductors and the capacitors, adaptive control was deployed to control a DC-DC Zeta converter in [23, 24]. In [23], a model reference adaptive control (MRAC) strategy was used to adjust the controller parameters so that the output voltage of the Zeta converter tracked the output voltage of the reference model. Furthermore, to cope with the nonlinearity model of the converter, a combination of MRAC with neural networks (NN) was used in [24]. The designed controller gave a satisfactory result but was very sensitive to the changes in the magnitude of the reference signal. In [25], a fuzzy logic-based controller was used to improve the steady-state and dynamic performance of a Zeta converter.

On the other hand, a state-feedback controller for a DC-DC Zeta converter was reported in [26]. Pole placement and optimal control were used to formulate the state-feedback controller. For the pole placement formulation, the state-feedback controller was derived by placing the poles seven times farther from the system's open left-half most poles location of the complex plane. For the optimal control formulation, an algebraic Ricatti equation was used to solve a linear quadratic regulator (LQR) problem over a finite time interval. The proposed state-feedback controllers can regulate the output voltage, and it was shown to work better than the PI controller since less effort was needed by the control duty ratio [27]. However, the output voltage steady-state error is considerably large. The most recent work was presented in [15]. The load and the input voltage variations were included in the Zeta converter model and were utilized in the design procedure based on the LQR problem. Albeit a robust controller was achieved, a relatively high percentage of ripple was propagated in the control duty ratio.

1.4.2 Hybrid Two-dimensional Converter Control

Hybrid system controls have been implemented for the stabilization of the DC-DC converters in [18, 28-35]. In [18, 28, 29], the authors have proposed a hybrid switching algorithm for a buck [18], a boost [28], and a buck-boost [29] converters. The hybrid switching algorithm restricted the state-trajectory within the limit specified by the guard conditions which were derived based on the observation of the approximated steady-state state waveform. Precisely, an explicit relation between the output voltage ripple and the inductor current ripple was found, and the switching took place when the pre-defined output voltage ripple size was reached. The authors in [30] have developed a hybrid system switching strategy of a boost converter where the switching among the modes was governed by an adjustable reference voltage and a reference current which were calculated by an energy balance principle. Even though the output voltage regulation was achieved, no theoretical work was discussed to prove the stability of the system.

In [31-35], the authors have proposed a Lyapunov-based hybrid system control to stabilize the DC-DC converters. In [31], the switching rule that assigns the mode decreasing the value of the Lyapunov function most was deployed for the buck, boost, and buck-boost converters. When the trajectory reached the switching boundary, it evolved as a sliding mode solution, which meant that the switching interval became infinitesimally small. The authors in [32, 33] have used a buck [32] and a boost [32, 33] converters and extended the idea in [31] by introducing a spatial regularization to reduce the switching frequency. In [34, 35], the authors have used sampled-data control to avoid sliding mode solutions. Though switching frequency was controlled by the sampling period, it tends to be small because the method was based on sufficient conditions. Hence the trajectory was close to the sliding solution. In general, because two-dimensional DC-DC converters were used in [31, 33-35], the stabilities of the hybrid control systems were analyzed by the standard Lyapunov approach by showing the decrease of the Lyapunov function along the trajectory. Furthermore, although the switching frequency can be controlled in [32-35], because the heuristic procedure was used to set the switching frequency, the output voltage was prone to have an offset error.

1.5 Thesis Contribution

This thesis presents three DC-DC Zeta converter control techniques. For the first control technique, we propose a robust DC-DC Zeta converter control operating in continuous conduction mode (CCM). We use an uncertain DC-DC Zeta converter model and formulate a linear quadratic regulator (LQR) problem into linear matrix inequality (LMI) representation; we refer to it as an LMI-LQR approach. We find the robust state-

feedback LMI-LQR control for the uncertain system and compare the performance to conventional LQR control. For the second control technique, we present a hybrid DC-DC Zeta converter control operating in CCM. Based on a control Lyapunov function (CLF), we define two switching functions to govern the hybrid system control strategy. We analyze the state waveform near the operating point under CCM operation and find an explicit relation between the hybrid switching control strategy and the switching frequency. For the third control technique, we propose a hybrid DC-DC Zeta converter control under discontinuous conduction mode (DCM) operation. We deploy a similar hybrid system control strategy in CCM, but with an additional switching function for the third mode. Moreover, we derive a hybrid system switching control strategy and the switching frequency relation by approximating the DCM steady-state state waveform.

As a result, we show that, through simulation, under highly uncertain conditions, our LMI-LQR control can robustly stabilize the output voltage, whereas the conventional LQR control is unable to return to its operating point, as reported in [36, 37]. For the hybrid system control in CCM, as reported in [38, 39], the controller has no problem in stabilizing the converter, even when the input voltage and the load are decreased as high as $-66\,\%$ and $-200\,\%$, respectively. Moreover, it is shown that the hybrid system control is more robust than the LMI-LQR control especially if the perturbations are outside the predefined uncertain parameters range, as reported in [40]. Furthermore, for the DCM operation, our hybrid system control can regulate the output voltage, while maintaining the desired DCM switching frequency as reported in [41, 42]. Apart from that, we established local asymptotic stability of the operating point by exploiting LaSalle's invariance principle for the class of differential inclusions, as reported in [39].

Chapter 2

Preliminaries

2.1 Mathematical Notation

Throughout this thesis, the following mathematical notation will be used. $\mathbb{R}$ and $\mathbb{R}_{-}$ denote the set of real, and non-positive numbers, respectively. For $\rho \in \mathbb{R}$, $\mathbb{R}_{>\rho}$, $\mathbb{R}_{<\rho}$, $\mathbb{R}_{\geq\rho}$, and $\mathbb{R}_{\leq\rho}$ denote the set of real numbers larger, smaller, larger than or equal to, and smaller than or equal to ρ, respectively. The notation conv denotes the convex hull of a set. For a function $\alpha : \mathbb{R}^n \to \mathbb{R}$, α^{-1} denotes the inverse image of α. For a singleton $\{c\}$, $c \in \mathbb{R}$, we use the simplified notation, $\alpha^{-1}(c) = \alpha^{-1}(\{c\})$. A set-valued map F is denoted as $F: \mathbb{R}^n \twoheadrightarrow \mathbb{R}^m$, where for $x \in \mathbb{R}^n$, $F(x) \subset \mathbb{R}^m$.

2.2 Zeta Converter Model in CCM Operation

In this chapter, three mathematical models of a DC-DC Zeta converter will be presented. The Zeta converter under continuous conduction mode (CCM), discontinuous conduction mode (DCM), and small-signal state-space averaging (SSA) models will be derived in sequential section order. These three models are instrumental and will be used in the following chapters of this thesis.

For a DC-DC Zeta converter operating in CCM, it can be modeled by a two-mode system, as depicted in Figure 2.1. Under mode 1 (see Figure 2.1(a)) and mode 2 (see Figure 2.1(b)), the dynamics of the inductor currents i_{L1} and i_{L2}, and the capacitor voltages v_{C1} and v_{C2}, are given by (2.1) and (2.2), respectively.

$$\frac{di_{L1}}{dt} = \frac{1}{L_1} v_g,$$
$$\frac{di_{L2}}{dt} = \frac{1}{L_2}\left(v_{C1} - v_{C2} + v_g\right),$$
$$\frac{dv_{C1}}{dt} = -\frac{1}{C_1} i_{L2},$$
$$\frac{dv_{C2}}{dt} = \frac{1}{C_2}\left(i_{L2} - \frac{1}{R} v_{C2}\right). \tag{2.1}$$

$$\frac{di_{L1}}{dt} = -\frac{1}{L_1} v_{C1},$$
$$\frac{di_{L2}}{dt} = -\frac{1}{L_2} v_{C2},$$
$$\frac{dv_{C1}}{dt} = \frac{1}{C_1} i_{L1},$$
$$\frac{dv_{C2}}{dt} = \frac{1}{C_2}\left(i_{L2} - \frac{1}{R} v_{C2}\right). \tag{2.2}$$

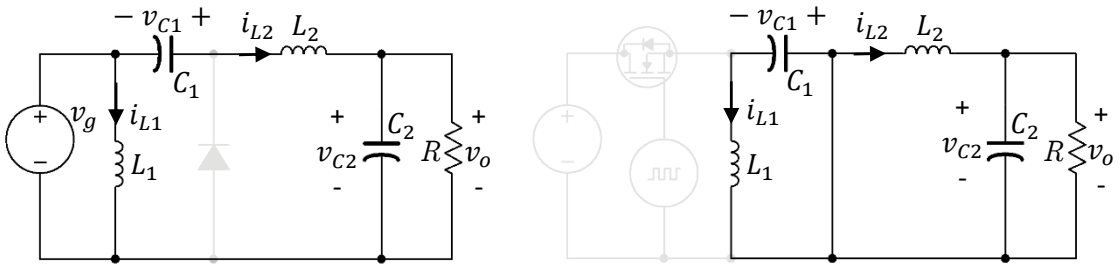

Figure 2.1: DC-DC Zeta converter inductor currents i_{L1} and i_{L2}, and capacitor voltages v_{C1} and v_{C2}, in CCM operation for (a) mode 1, and (b) mode 2.

The state-space representations for the Zeta converter under CCM operation for mode 1 and mode 2 can be described as

$$\frac{dx}{dt} = A_1 x + B_1 u, \tag{2.3}$$
$$\frac{dx}{dt} = A_2 x + B_2 u, \tag{2.4}$$

respectively.

Choose state vector $x = [i_{L1}\ i_{L2}\ v_{C1}\ v_{C2}]^T$, and the input $u = v_g$. Then, the matrices of the Zeta converter in CCM can be found by comparing (2.1) and (2.2) to (2.3) and (2.4), respectively, and are given by

$$A_1 = \begin{bmatrix} 0 & 0 & 0 & 0 \\ 0 & 0 & \frac{1}{L_2} & -\frac{1}{L_2} \\ 0 & -\frac{1}{C_1} & 0 & 0 \\ 0 & \frac{1}{C_2} & 0 & -\frac{1}{RC_2} \end{bmatrix}, \quad B_1 = \begin{bmatrix} \frac{1}{L_1} \\ \frac{1}{L_2} \\ 0 \\ 0 \end{bmatrix},$$

$$A_2 = \begin{bmatrix} 0 & 0 & -\frac{1}{L_1} & 0 \\ 0 & 0 & 0 & -\frac{1}{L_2} \\ \frac{1}{C_1} & 0 & 0 & 0 \\ 0 & \frac{1}{C_2} & 0 & -\frac{1}{RC_2} \end{bmatrix}, \quad B_2 = \begin{bmatrix} 0 \\ 0 \\ 0 \\ 0 \end{bmatrix}. \tag{2.5}$$

2.3 Zeta Converter Model in DCM Operation

In DCM operation, as shown in Figure 2.2, a Zeta converter can be modeled by a three-mode system. The dynamics of inductor currents i_{L1} and i_{L2}, and capacitor voltages v_{C1} and v_{C2}, under mode 1, mode 2, and mode 3, as illustrated in Figure 2.2(a), Figure 2.2(b), and Figure 2.2(c), respectively, are given by

$$\begin{aligned} \frac{di_{L1}}{dt} &= \frac{1}{L_1} v_g, \\ \frac{di_{L2}}{dt} &= \frac{1}{L_2}\left(v_{C1} - v_{C2} + v_g\right), \\ \frac{dv_{C1}}{dt} &= -\frac{1}{C_1} i_{L2}, \\ \frac{dv_{C2}}{dt} &= \frac{1}{C_2}\left(i_{L2} - \frac{1}{R} v_{C2}\right). \end{aligned} \tag{2.6}$$

$$\begin{aligned} \frac{di_{L1}}{dt} &= -\frac{1}{L_1} v_{C1}, \\ \frac{di_{L2}}{dt} &= -\frac{1}{L_2} v_{C2}, \\ \frac{dv_{C1}}{dt} &= \frac{1}{C_1} i_{L1}, \\ \frac{dv_{C2}}{dt} &= \frac{1}{C_2}\left(i_{L2} - \frac{1}{R} v_{C2}\right). \end{aligned} \tag{2.7}$$

$$\begin{aligned} \frac{di_{L1}}{dt} &= -\frac{1}{L_1+L_2}(v_{C1} - v_{C2}), \\ \frac{di_{L2}}{dt} &= \frac{1}{L_1+L_2}(v_{C1} - v_{C2}), \\ \frac{dv_{C1}}{dt} &= \frac{1}{C_1} i_{L1}, \\ \frac{dv_{C2}}{dt} &= \frac{1}{C_2}\left(i_{L2} - \frac{1}{R} v_{C2}\right). \end{aligned} \tag{2.8}$$

respectively.

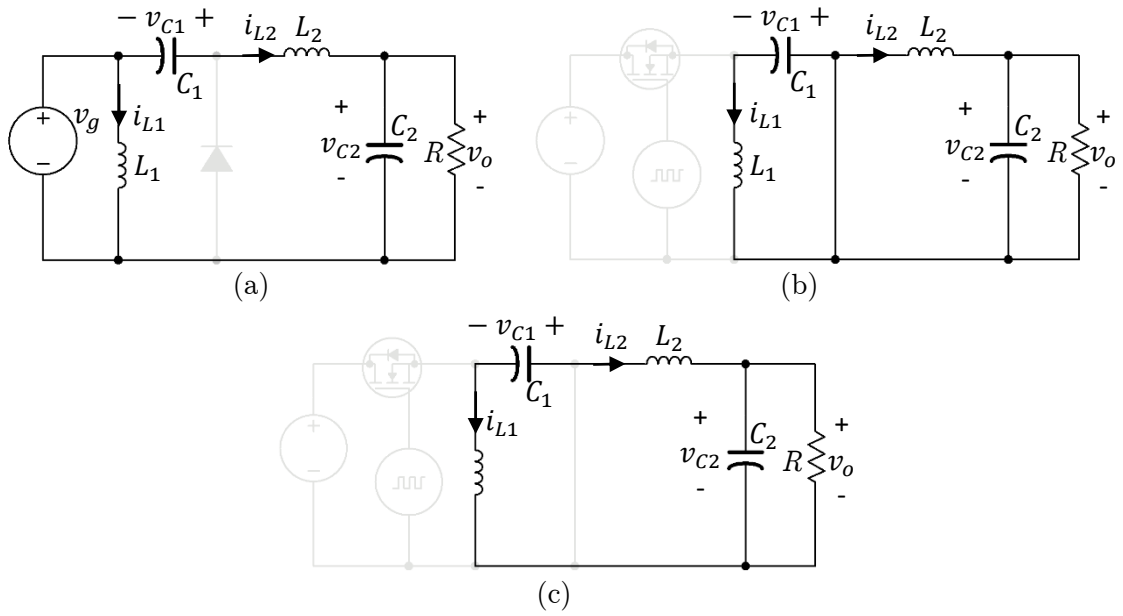

Figure 2.2: DC-DC Zeta converter inductor currents i_{L1} and i_{L2}, and capacitor voltages v_{C1} and v_{C2}, in DCM operation for (a) mode 1, (b) mode 2, and (c) mode 3.

Mode 1, mode 2, and mode 3 of the Zeta converter in DCM operation can be represented in state-space by

$$\frac{dx}{dt} = A_1 x + B_1 u, \tag{2.9}$$

$$\frac{dx}{dt} = A_2 x + B_2 u, \tag{2.10}$$

$$\frac{dx}{dt} = A_3 x + B_3 u, \tag{2.11}$$

respectively.

Consider the state vector $x = [i_{L1}\ \ i_{L2}\ \ v_{C1}\ \ v_{C2}]^T$, and the input $u = v_g$, then, comparing (2.6), (2.7), and (2.8) to (2.9), (2.10), and (2.11), respectively, one gets the matrices of the Zeta converter in DCM operation as follows:

$$A_1 = \begin{bmatrix} 0 & 0 & 0 & 0 \\ 0 & 0 & \frac{1}{L_2} & -\frac{1}{L_2} \\ 0 & -\frac{1}{C_1} & 0 & 0 \\ 0 & \frac{1}{C_2} & 0 & -\frac{1}{RC_2} \end{bmatrix}, \quad B_1 = \begin{bmatrix} \frac{1}{L_1} \\ \frac{1}{L_2} \\ 0 \\ 0 \end{bmatrix},$$

$$A_2 = \begin{bmatrix} 0 & 0 & -\frac{1}{L_1} & 0 \\ 0 & 0 & 0 & -\frac{1}{L_2} \\ \frac{1}{C_1} & 0 & 0 & 0 \\ 0 & \frac{1}{C_2} & 0 & -\frac{1}{RC_2} \end{bmatrix}, \quad B_2 = \begin{bmatrix} 0 \\ 0 \\ 0 \\ 0 \end{bmatrix},$$

$$A_3 = \begin{bmatrix} 0 & 0 & -\frac{1}{L_1+L_2} & \frac{1}{L_1+L_2} \\ 0 & 0 & \frac{1}{L_1+L_2} & -\frac{1}{L_1+L_2} \\ \frac{1}{C_1} & 0 & 0 & 0 \\ 0 & \frac{1}{C_2} & 0 & -\frac{1}{RC_2} \end{bmatrix}, \quad B_3 = \begin{bmatrix} 0 \\ 0 \\ 0 \\ 0 \end{bmatrix}. \tag{2.12}$$

2.4 Zeta Converter Small-signal SSA Model in CCM Operation

In SSA approach, mode 1 and mode 2 of the DC-DC Zeta converter in CCM operation are averaged over one switching period. The SSA of the Zeta converter can be written as

$$\frac{dx}{dt} = Ax + Bu, \tag{2.13}$$

where

$$\begin{aligned} A &= A_1 d + A_2(1-d), \\ B &= B_1 d + B_2(1-d), \end{aligned} \tag{2.14}$$

where d is the duty ratio.

Assume the variables change linearly around the operating point such that

$$\begin{aligned} x &= X + \tilde{x}, \\ u &= U + \tilde{u}, \\ d &= D_d + \tilde{d}_d, \end{aligned} \tag{2.15}$$

where X, U, and D_d are the steady-state values, $\tilde{x}$, $\tilde{u}$, and $\tilde{d}_d$ are the small-signal values.

Substituting (2.14) and (2.15) into (2.13), one gets the Zeta converter small-signal SSA model as follows:

$$\frac{d\tilde{x}}{dt} = A_{ss}\tilde{x} + B_{ss}\tilde{u} + B_d\tilde{d}_d + A_{dx}\tilde{d}_d\tilde{x} + B_{du}\tilde{d}_d\tilde{u}, \tag{2.16}$$

where

$$\begin{aligned} A_{ss} &= A_1 D_d + A_2(1 - D_d), \\ B_{ss} &= B_1 D_d + B_2(1 - D_d), \\ B_d &= (A_1 - A_2)X + (B_1 - B_2)U, \\ A_{dx} &= A_1 - A_2, \\ B_{du} &= B_1 - B_2. \end{aligned} \tag{2.17}$$

Because the differential of steady-state is zero $\left(\frac{dX}{dt} = 0\right)$, from (2.13), the steady-state for the state vector is given by

$$X = -{A_{ss}}^{-1} B_{ss} U. \tag{2.18}$$

If the products of small-signal terms $\tilde{d}_d \tilde{x}$ and $\tilde{d}_d \tilde{u}$ in (2.16) are considered small and neglected, the approximate small-signal SSA model for the converter is described as

$$\frac{d\tilde{x}}{dt} = A_{ss}\tilde{x} + B_{ss}\tilde{u} + B_d \tilde{d}_d. \tag{2.19}$$

Choose steady-state input $U = V_g$. Then, from (2.5), (2.17) and (2.18), the matrices for the Zeta converter small-signal SSA model (2.19) are given by

$$A_{ss} = \begin{bmatrix} 0 & 0 & -\frac{1-D_d}{L_1} & 0 \\ 0 & 0 & \frac{D_d}{L_2} & -\frac{1}{L_2} \\ \frac{1-D_d}{C_1} & -\frac{D_d}{C_1} & 0 & 0 \\ 0 & \frac{1}{C_2} & 0 & -\frac{1}{RC_2} \end{bmatrix}, \quad B_{ss} = \begin{bmatrix} \frac{D_d}{L_1} \\ \frac{D_d}{L_2} \\ 0 \\ 0 \end{bmatrix}, \quad B_d = \begin{bmatrix} \frac{V_g}{(1-D_d)L_1} \\ \frac{V_g}{(1-D_d)L_2} \\ \frac{D_d V_g}{(1-D_d)^2 C_1 R} \\ 0 \end{bmatrix}. \tag{2.20}$$

Chapter 3

Robust DC-DC Zeta Converter Control Operating in CCM

3.1 Uncertain SSA Zeta Converter Model in CCM Operation

In this section, modifying the idea from [43], we propose a robust state-feedback control technique to stabilize an uncertain DC-DC Zeta converter operating in continuous conduction mode (CCM). The Zeta converter is modeled based on a linear state-space averaging (SSA) approach, and the state-feedback controller is formulated in terms of a linear matrix inequality (LMI) from a linear quadratic regulator (LQR) problem.

In general, a basic state-feedback control for a converter produces an output voltage error [26]. To achieve zero-offset between the output voltage v_o and the reference voltage v_{ref}, an additional state-variable $\tilde{x}_{int} = \int(v_{ref} - v_{C2})dt$ is introduced to enforce the integral action of the output error, as illustrated in Figure 3.1. Let the augmented state vector is given by $\tilde{x}_a = [\tilde{\imath}_{L1}\ \tilde{\imath}_{L2}\ \tilde{v}_{C1}\ \tilde{v}_{C2}\ \tilde{x}_{int}]^T$, then from (2.20) in Section 2.4, the matrices are augmented as follows:

$$A_{ssa} = \begin{bmatrix} 0 & 0 & -\frac{1-D_d}{L_1} & 0 & 0 \\ 0 & 0 & \frac{D_d}{L_2} & -\frac{1}{L_2} & 0 \\ \frac{1-D_d}{C_1} & -\frac{D_d}{C_1} & 0 & 0 & 0 \\ 0 & \frac{1}{C_2} & 0 & -\frac{1}{RC_2} & 0 \\ 0 & 0 & 0 & -1 & 0 \end{bmatrix},\ B_{ssa} = \begin{bmatrix} \frac{D_d}{L_1} \\ \frac{D_d}{L_2} \\ 0 \\ 0 \\ 0 \end{bmatrix},\ B_{da} = \begin{bmatrix} \frac{V_g}{(1-D_d)L_1} \\ \frac{V_g}{(1-D_d)L_2} \\ \frac{D_d V_g}{(1-D_d)^2 C_1 R} \\ 0 \\ 0 \end{bmatrix}. \quad (3.1)$$

From (3.1), some parameters can be uncertain, and these matrices are represented as a function of such parameters. If the external input is neglected, the small-signal SSA model for the uncertain DC-DC Zeta converter is given by

$$\frac{d\tilde{x}_a}{dt} = A_{ssa}(p)\tilde{x}_a + B_{da}(p)\tilde{d}, \tag{3.2}$$

where p is the vector of uncertain parameters. Let $p = (p_1, p_2, \dots, p_{n_p})$, where n_p is the number of uncertain parameters. It is assumed that each parameter has an upper and lower limit. Then, the allowable values of the vector p are constrained in a hyper-rectangle in $\mathbb{R}^{n_p}$ with $N = 2^{n_p}$ vertices. The uncertain matrices $A_{ssa}(p)$ and $B_{da}(p)$ can be included in a convex polytope

$$[A_{ssa}(p), B_{da}(p)] \in \operatorname{conv}\{\mathcal{G}_1, \dots, \mathcal{G}_N\} \coloneqq \left\{\sum_{i=1}^{N} \lambda_i \mathcal{G}_i, \;\; \lambda_i \geq 0, \;\; \sum_{i=1}^{N} \lambda_i = 1\right\}, \tag{3.3}$$

where the images of the matrix $[A_{ssa}(p), B_{da}(p)]$ for each vertex corresponding to a set $\{\mathcal{G}_1, \dots, \mathcal{G}_N\}$. The components of the set $\{\mathcal{G}_1, \dots, \mathcal{G}_N\}$ are the extrema of a convex polytope that contains the images for all allowable values of p.

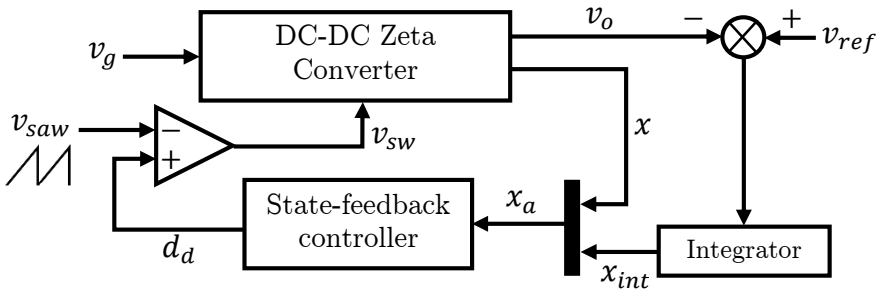

Figure 3.1: State-feedback controller with integral action.

In practice, the input and the output of a DC-DC Zeta converter can vary since they are connected to the external source and load, respectively. As such, the input voltage V_g and the load R are chosen as the uncertain parameters. However, because the duty ratio D_d largely influences the matrices (3.1) and is a function of V_g described by $D_d = \left(1 + \frac{V_g}{v_{ref}}\right)^{-1}$ [26], D_d is selected as the uncertain parameter instead of V_g. To describe a convex polytope of the uncertainty, each block must depend linearly on the uncertain parameters. Since the condition is not met for A_{ssa} and B_{da} matrices, two new variables are introduced; $\frac{1}{1-D_d}$ and $\frac{D_d}{(1-D_d)^2 R}$, to produce linear dependence. Thus, the vector of uncertain parameters for the Zeta converter can be written as

$$p = \left(D_d,\ \frac{1}{1-D_d},\ \frac{D_d}{(1-D_d)^2 R},\ \frac{1}{R}\right). \tag{3.4}$$

Furthermore, the uncertain parameters are assumed to be within the following range:

$$\begin{aligned} D_d &\in \left[D_{d,\min}\ \ D_{d,\max}\right], \\ \frac{1}{1-D_d} &\in \left[\frac{1}{1-D_{d,\min}}\ \ \frac{1}{1-D_{d,\max}}\right], \\ \frac{D_d}{(1-D_d)^2 R} &\in \left[\frac{D_{d,\min}}{(1-D_{d,\min})^2 R_{\max}}\ \ \frac{D_{d,\max}}{(1-D_{d,\max})^2 R_{\min}}\right], \\ \frac{1}{R} &\in \left[\frac{1}{R_{\max}}\ \ \frac{1}{R_{\min}}\right]. \end{aligned} \tag{3.5}$$

The parameters given by (3.4) define the uncertain matrices $A_{ssa}(p)$ and $B_{da}(p)$, which can be included in the convex polytope (3.3). In general, the convex polytope of uncertainty is covered by 16 vertices for a given four uncertain parameters in (3.4). However, as will be presented later in Section 3.3, to reduce the conservativeness, an additional version of the convex polytope of uncertainty covered by eight vertices is proposed.

3.2 LMI-LQR Control Formulation

In this section, a linear matrix inequality (LMI) will be formulated from a linear quadratic regulator (LQR) problem, which can then be solved by the convex optimization method. This convex optimization method is particularly advantageous because it guarantees the quadratic stability for all possible cases of the uncertain DC-DC Zeta converter. In the following, the quadratic stability of an uncertain system is presented.

Consider a linear system

$$\frac{dx}{dt} = A_{cl}x, \tag{3.6}$$

where A_{cl} is the closed-loop system matrix. The well-established Lyapunov theory states that if there exists a positive definite matrix P, such that the quadratic function

$$V(x) = x^T P x > 0 \quad \forall x \neq 0,$$

satisfies the following condition along the trajectories of the system (3.6)

$$\dot{V}(x) = x^T\left(A_{cl}^T P + P A_{cl}\right)x < 0 \quad \forall x \neq 0,$$

then the system (3.6) is quadratically stable and all its trajectories will converge to the origin [44]. Furthermore, assume that the system (3.6) is the uncertain system described by $A_{cl,i} \in \text{conv}\left\{A_{cl,1}, A_{cl,2}, \dots, A_{cl,N}\right\}$. If there exist $P > 0$ such that

$$x^T\left(A_{cl,i}^T P + P A_{cl,i}\right)x < 0 \quad \forall x \neq 0, \quad \forall i = 1, \dots, N$$

then the uncertain system (3.6) is quadratically stable.

Assume the augmented matrices A_{ssa} and B_{da} are controllable and all the states are accessible. Then, feedback of all of the states through a gain matrix K can be used, and the control law is given by [45]

$$\tilde{u}_d = \tilde{d}_d = -K\tilde{x}_a. \tag{3.7}$$

To optimally control the control effort within a performance specification, a compensator is sought to provide a control effort for an input that minimizes a cost function or performance index [46] as follows:

$$J = \int_0^\infty \left(\tilde{x}_a^T Q_w \tilde{x}_a + \tilde{u}_d^T R_w \tilde{u}_d\right) dt, \tag{3.8}$$

where Q_w is a symmetric, positive semidefinite matrix and R_w is a symmetric, positive definite matrix. The optimization problem (3.8) is known as an LQR problem. The LQR problem is essentially a weighted minimization of the states $\tilde{x}_a$ and the control input $\tilde{u}_d$, by selecting weighting matrices Q_w and R_w, respectively.

Inserting (3.7) into (3.8), one gets

$$J = \int_0^\infty (\tilde{x}_a^T (Q_w + K^T R_w K)\tilde{x}_a)\, dt.$$

Using trace operator $\text{Tr}(.)$, the above cost function is equivalent to

$$\begin{aligned} J &= \int_0^\infty \text{Tr}\left((Q_w + K^T R_w K)\tilde{x}_a \tilde{x}_a^T\right) dt \\ &= \text{Tr}(Q_w + K^T R_w K)P_0, \end{aligned}$$

where $P_0 = \int_0^\infty (\tilde{x}_a \tilde{x}_a^T)\, dt$ is a definite positive symmetric matrix that satisfies

$$(A_{ssa} - B_{da}K)P_0 + P_0(A_{ssa} - B_{da}K)^T + \tilde{x}_{a(0)}\tilde{x}_{a(0)}^T = 0,$$

where $\tilde{x}_{a(0)}$ represents the initial condition of the state.

Define P by a matrix inequality

$$(A_{ssa} - B_{da}K)P + P(A_{ssa} - B_{da}K)^T + I < 0.$$

Because $\|\tilde{x}_{a(0)}\| < 1$, we have

$$\mathrm{Tr}(Q_w + K^T R_w K)P_0 < \mathrm{Tr}(Q_w + K^T R_w K)P.$$

Hence, the matrix P gives an upper bound for the performance of the feedback control (3.7).

The feedback gain K is attained from the following optimization problem

$$\min_{P,K} \mathrm{Tr}(Q_w P) + \mathrm{Tr}\left(R_w^{\frac{1}{2}} K P K^T R_w^{\frac{1}{2}}\right),$$

subject to

$$A_{ssa}P + PA_{ssa}^T - B_{da}KP - (KP)^T B_{da}^T + I < 0.$$

Due to the existence of nonlinear term (multiplication of K and P), a new variable $Y = KP$ is introduced, thus the optimization can be rewritten as

$$\min_{P,Y} \mathrm{Tr}(Q_w P) + \mathrm{Tr}\left(R_w^{\frac{1}{2}} Y P^{-1} Y^T R_w^{\frac{1}{2}}\right),$$

subject to

$$A_{ssa}P + PA_{ssa}^T - B_{da}Y - Y^T B_{da}^T + I < 0.$$

Likewise, define $X = R_w^{\frac{1}{2}} Y P^{-1} Y^T R_w^{\frac{1}{2}}$ such that

$$\min_X \mathrm{Tr}(X) \text{ subject to } \mathrm{X} > R_w^{\frac{1}{2}} Y P^{-1} Y^T R_w^{\frac{1}{2}}.$$

Moreover, using Schur's complement, $\mathrm{X} > R_w^{\frac{1}{2}} Y P^{-1} Y^T R_w^{\frac{1}{2}}$ is equivalent to

$$\begin{bmatrix} X & R_w^{\frac{1}{2}} Y \\ Y^T R_w^{\frac{1}{2}} & P \end{bmatrix} > 0.$$

The complete LMI-LQR control formulation is therefore given by

$$\min_{P,Y,X} \mathrm{Tr}(Q_w P) + \mathrm{Tr}(X),$$

subject to

$$\begin{aligned} A_{ssa} P + P A_{ssa}^T - B_{da} Y - Y^T B_{da}^T + I < 0, \\ \begin{bmatrix} X & R_w^{\frac{1}{2}} Y \\ Y^T R_w^{\frac{1}{2}} & P \end{bmatrix} > 0, \qquad P > 0. \end{aligned} \tag{3.9}$$

Note that the constraint in (3.9) is for a system without uncertainty. To include the uncertain parameters, nominal matrices A_{ssa} and B_{da} in (3.9) are replaced with the matrices that correspond to all vertices of the polytope $A_{ssa,i}$ and $B_{da,i}$ defined in (3.3), which can be written as follows:

$$A_{ssa,i} P + P A_{ssa,i}^T - B_{da,i} Y - Y^T B_{da,i}^T + I < 0, \;\; i = 1, \dots, N. \tag{3.10}$$

The solution of (3.9) produces a common matrix P that satisfies (3.10) at all the vertices of the convex polytope. Once this minimization under constraints is solved, the LMI-LQR controller can be recovered by $K = YP^{-1}$. Since P satisfies (3.10), this feedback gain K will ensure quadratic stability of the closed-loop system. It is worth highlighting that compared with a conventional LQR formulation based on the Riccati equation, the presented LMI-LQR formulation allows one to include the uncertainties of the parameters into the controller design procedure, thus, produces a robust controller.

Remark 1. The main purpose of the above LMI-LQR formulation is to have a fixed gain controller that is simple yet can produce satisfactory output voltage regulation performance under uncertain operating conditions. This is important consideration because a fast controller is needed due to the high switching frequency is required.

3.3 Design Example

In this section, the proposed LMI-LQR control is applied to a DC-DC Zeta converter using a set of parameters tabulated in Table 3.1. Referring to Table 3.1 and $D_d = \left(1+\frac{v_g}{v_{ref}}\right)^{-1}$, from (3.5), it follows that

$$D_d \in [0.375 \quad 0.6],\ \frac{1}{1-D_d} \in [1.6 \quad 2.5],\ \frac{D_d}{(1-D_d)^2 R} \in [0.32 \quad 2.5],\ \frac{1}{R} \in [0.33 \quad 0.67]. \tag{3.11}$$

Table 3.1: The DC-DC Zeta converter with uncertain parameters.

Parameter	Value	Nominal value
v_g	[6 15] V	15 V
$v_o(v_{ref})$	9 V	-
R	[1.5 3] Ω	1.5 Ω
L_1	100 μH	-
L_2	55 μH	-
C_1	100 μF	-
C_2	200 μF	-
f	100 kHz	-

Conventionally, as given in Table 3.2, 16 uncertain parameter vectors p are allowed, in correspond to four uncertain parameters (3.11). Subsequently, a convex polytope with 16 vertices is formed, which is given by the following system matrices

$$\begin{aligned}
&[A_{ssa}(p), B_{da}(p)] \in \mathcal{P}_{16} = \mathrm{co}\{\mathcal{G}_{1a}, \dots, \mathcal{G}_{16a}\}: \\
&\quad \mathcal{G}_{1a} = [A_{ssa}(p_{1a}), B_{da}(p_{1a})], \quad \mathcal{G}_{2a} = [A_{ssa}(p_{2a}), B_{da}(p_{2a})], \\
&\quad \mathcal{G}_{3a} = [A_{ssa}(p_{3a}), B_{da}(p_{3a})], \quad \mathcal{G}_{4a} = [A_{ssa}(p_{4a}), B_{da}(p_{4a})], \\
&\quad \mathcal{G}_{5a} = [A_{ssa}(p_{5a}), B_{da}(p_{5a})], \quad \mathcal{G}_{6a} = [A_{ssa}(p_{6a}), B_{da}(p_{6a})], \\
&\quad \mathcal{G}_{7a} = [A_{ssa}(p_{7a}), B_{da}(p_{7a})], \quad \mathcal{G}_{8a} = [A_{ssa}(p_{8a}), B_{da}(p_{8a})], \\
&\quad \mathcal{G}_{9a} = [A_{ssa}(p_{9a}), B_{da}(p_{9a})], \quad \mathcal{G}_{10a} = [A_{ssa}(p_{10a}), B_{da}(p_{10a})], \\
&\quad \mathcal{G}_{11a} = [A_{ssa}(p_{11a}), B_{da}(p_{11a})], \quad \mathcal{G}_{12a} = [A_{ssa}(p_{12a}), B_{da}(p_{12a})], \\
&\quad \mathcal{G}_{13a} = [A_{ssa}(p_{13a}), B_{da}(p_{13a})], \quad \mathcal{G}_{14a} = [A_{ssa}(p_{14a}), B_{da}(p_{14a})], \\
&\quad \mathcal{G}_{15a} = [A_{ssa}(p_{15a}), B_{da}(p_{15a})], \quad \mathcal{G}_{16a} = [A_{ssa}(p_{16a}), B_{da}(p_{16a})].
\end{aligned} \tag{3.12}$$

Table 3.2: 16 uncertain parameters vectors.

Uncertain parameters vector $p = \left(D_d,\ \frac{1}{1-D_d},\ \frac{D_d}{(1-D_d)^2R},\ \frac{1}{R}\right)$
$p_{1a} = (0.375,\ 1.6,\ 0.32,\ 0.33)$
$p_{2a} = (0.375,\ 1.6,\ 0.32,\ 0.67)$
$p_{3a} = (0.375,\ 1.6,\ 2.5,\ 0.33)$
$p_{4a} = (0.375,\ 1.6,\ 2.5,\ 0.67)$
$p_{5a} = (0.375,\ 2.5,\ 0.32,\ 0.33)$
$p_{6a} = (0.375,\ 2.5,\ 0.32,\ 0.67)$
$p_{7a} = (0.375,\ 2.5,\ 2.5,\ 0.33)$
$p_{8a} = (0.375,\ 2.5,\ 2.5,\ 0.67)$
$p_{9a} = (0.6,\ 1.6,\ 0.32,\ 0.33)$
$p_{10a} = (0.6,\ 1.6,\ 0.32,\ 0.33)$
$p_{11a} = (0.6,\ 1.6,\ 2.5,\ 0.33)$
$p_{12a} = (0.6,\ 1.6,\ 2.5,\ 0.33)$
$p_{13a} = (0.6,\ 2.5,\ 0.32,\ 0.33)$
$p_{14a} = (0.6,\ 2.5,\ 0.32,\ 0.33)$
$p_{15a} = (0.6,\ 2.5,\ 2.5,\ 0.33)$
$p_{16a} = (0.6,\ 2.5,\ 2.5,\ 0.33)$

The stability and an upper cost bound are guaranteed for the convex polytope (3.12) for the uncertainties described in (3.11). Due to the switching nature of a DC-DC Zeta converter, the control duty ratio contains a high-frequency ripple. The ripple should be lower than 20% to avoid the nonlinear behavior of the PWM circuitry [47, 48]. As such, a less conservative design is proposed where the convex polytope covering is tightened. The proposed procedure to tighten the polytope covering is illustrated in Figure 3.2. Essentially, the procedure involves finding a few coordinates such that the polytope s sufficiently covered. From the procedure, the possible values of the uncertain parameters vector are now reduced to eight, as tabulated in Table 3.3. The corresponding eight vertices of the convex polytope of uncertainty is formed by the following system matrices

$$
\begin{aligned}
&[A_{ssa}(p), B_{da}(p)] \in \mathcal{P}_8 = \mathrm{co}\{\mathcal{G}_{1b}, \dots, \mathcal{G}_{8b}\}:\\
&\quad \mathcal{G}_{1b} = [A_{ssa}(p_{1b}), B_{da}(p_{1b})], \quad \mathcal{G}_{2b} = [A_{ssa}(p_{2b}), B_{da}(p_{2b})],\\
&\quad \mathcal{G}_{3b} = [A_{ssa}(p_3 b), B_{da}(p_{3b})], \quad \mathcal{G}_{4b} = [A_{ssa}(p_{4b}), B_{da}(p_{4b})],\\
&\quad \mathcal{G}_{5b} = [A_{ssa}(p_{5b}), B_{da}(p_{5b})], \quad \mathcal{G}_{6b} = [A_{ssa}(p_{6b}), B_{da}(p_{6b})],\\
&\quad \mathcal{G}_{7b} = [A_{ssa}(p_{7b}), B_{da}(p_{7b})], \quad \mathcal{G}_{8b} = [A_{ssa}(p_{8b}), B_{da}(p_{8b})].
\end{aligned} \tag{3.13}
$$

Table 3.3: Eight uncertain parameters vectors.

Uncertain parameters vector $p = \left(D_d,\ \frac{1}{1-D_d},\ \frac{D_d}{(1-D_d)^2}\cdot\left(\frac{1}{R}\right),\ \frac{1}{R}\right)$
$p_{1b} = (0.375,\ 1.6,\ 0.95\cdot(0.33),\ 0.33)$
$p_{2b} = (0.375,\ 1.6,\ 0.95\cdot(0.67),\ 0.67)$
$p_{3b} = (0.52,\ 1.97,\ 1.78\cdot(0.33),\ 0.33)$
$p_{4b} = (0.52,\ 1.97,\ 1.78\cdot(0.67),\ 0.67)$
$p_{5b} = (0.52,\ 2.01,\ 1.78\cdot(0.33),\ 0.33)$
$p_{6b} = (0.52,\ 2.01,\ 1.78\cdot(0.67),\ 0.67)$
$p_{7b} = (0.6,\ 2.5,\ 3.75\cdot(0.33),\ 0.33)$
$p_{8b} = (0.6,\ 2.5,\ 3.75\cdot(0.67),\ 0.67)$

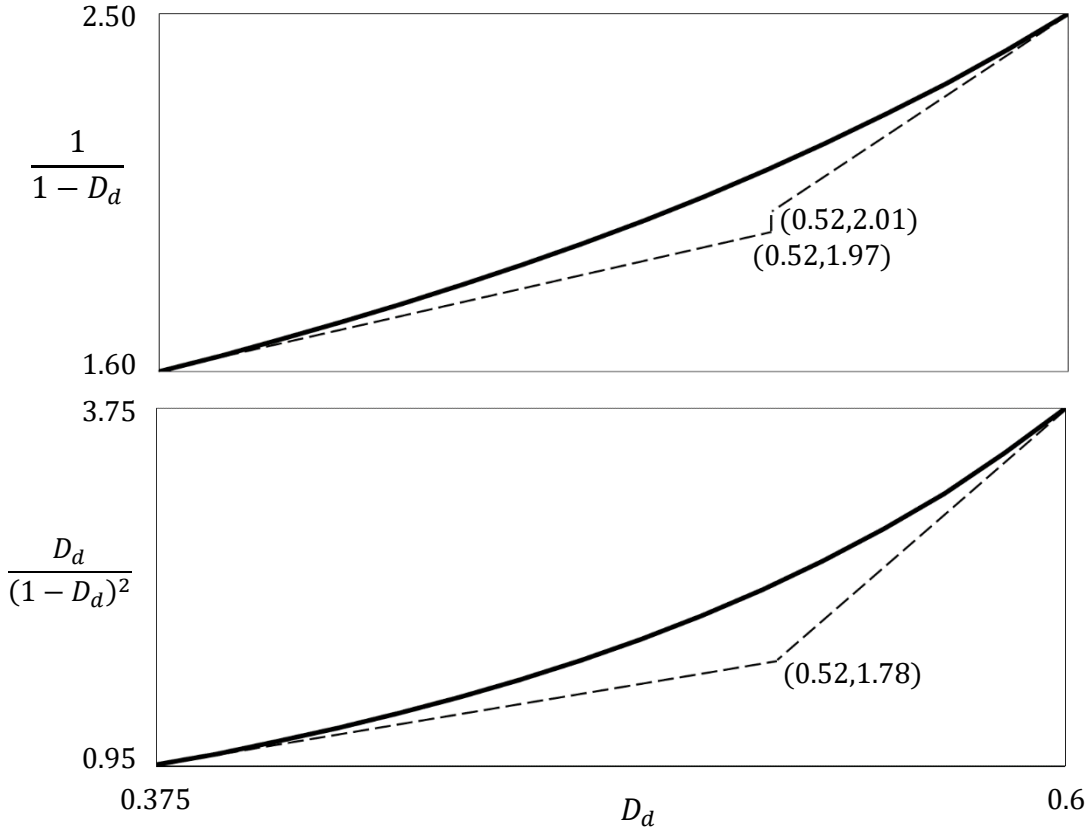

Figure 3.2: Coordinate for the reduced convex polytope covering.

Remark 2. Although it is possible to further tighten the convex polytope covering to improve some performance specifications, as will be shown later in Section 3.4, the proposed polytope covering version is sufficient to produce the desired output voltage regulation and control duty ratio ripple propagation.

To demonstrate the effectiveness of the proposed control formulation, three versions of state-feedback LQR controllers are presented: 1) the nominal LQR feedback controller K_{LQR}, 2) the LMI-LQR feedback controller K_{LMI16} with 16 vertices for the uncertain convex polytope, and 3) the LMI-LQR feedback controller K_{LMI8} with 8 vertices of an uncertain convex polytope. The weight matrices Q_w and R_w of the LQR performance index are selected as follows:

$$Q_w = \begin{bmatrix} 0 & 0 & 0 & 0 & 0 \\ 0 & 10^{-4} & 0 & 0 & 0 \\ 0 & 0 & 0 & 0 & 0 \\ 0 & 0 & 0 & 10^{-4} & 0 \\ 0 & 0 & 0 & 0 & 5\times 10^{6} \end{bmatrix}, \quad R_w = 1. \tag{3.14}$$

The three state-feedback controllers are found by solving the optimization problem (3.9) with the matrices defined in (3.1) and (3.14). The computation is done by Matlab LMI solver [49] called *mincx*, which is based on the barrier function of the interior-point method. The details of the Matlab codes are presented in Appendix B to D. Note that to find K_{LMI16} and K_{LMI8}, the LMI constraint (3.10) and their respective convex polytope of uncertainty (3.12) and (3.13) are used. Consider the control input $\tilde{u}_d = \tilde{d}_d$ and $\tilde{d} = -K_1\tilde{\imath}_{L1} - K_2\tilde{\imath}_{L2} - K_3\tilde{v}_{C1} - K_4\tilde{v}_{C2} - K_5\tilde{x}_{\text{int}}$. Then, the state-feedback gain vectors are given by

$$\begin{aligned} K_{LQR} &= [0.0673 \quad 0.0441 \quad 0.0661 \quad 0.1876 \quad -2236.1], \\ K_{LMI16} &= [0.3755 \quad 0.0701 \quad 0.1588 \quad 0.3408 \quad -2226.4], \\ K_{LMI8} &= [0.2531 \quad 0.0450 \quad 0.1736 \quad 0.3551 \quad -2240.1]. \end{aligned} \tag{3.15}$$

From (3.15), it can be observed that the state-feedback controller K_{LQR} for the nominal plant has considerably smaller gains compared to those with multiple plants. Roughly speaking, as much uncertainty there is in a DC-DC Zeta converter, higher state-feedback gains are expected, especially the gains for the inductor currents $\tilde{\imath}_{L1}$ and $\tilde{\imath}_{L2}$.

Remark 3. The positive definiteness of matrix P $(P > 0)$ in constraint (3.9) is verified by the Matlab numerical solution of the optimization problem in (3.9) where all the eigenvalues of P are positive for all three controllers in (3.15).

3.4 Simulation Results

To verify the performance of the proposed state-feedback control method, a simulation is carried out using PSIM, which is a circuit-based simulator. The simulation circuit for the closed-loop DC-DC Zeta converter is depicted in Figure 3.3. For simplicity, all electronic components are considered ideal where the internal resistances are considered small and negligible, and all the state variables are assumed measurable using either a current or voltage sensor. The simulation results are group into two conditions; nominal and non-nominal. A nominal condition refers to a nominal input voltage $v_g = 15\,\text{V}$ (implies duty ratio $D_d = 0.375$), whereas $v_g = 6\,\text{V}$ ($D_d = 0.6$) is referred to as a non-nominal condition.

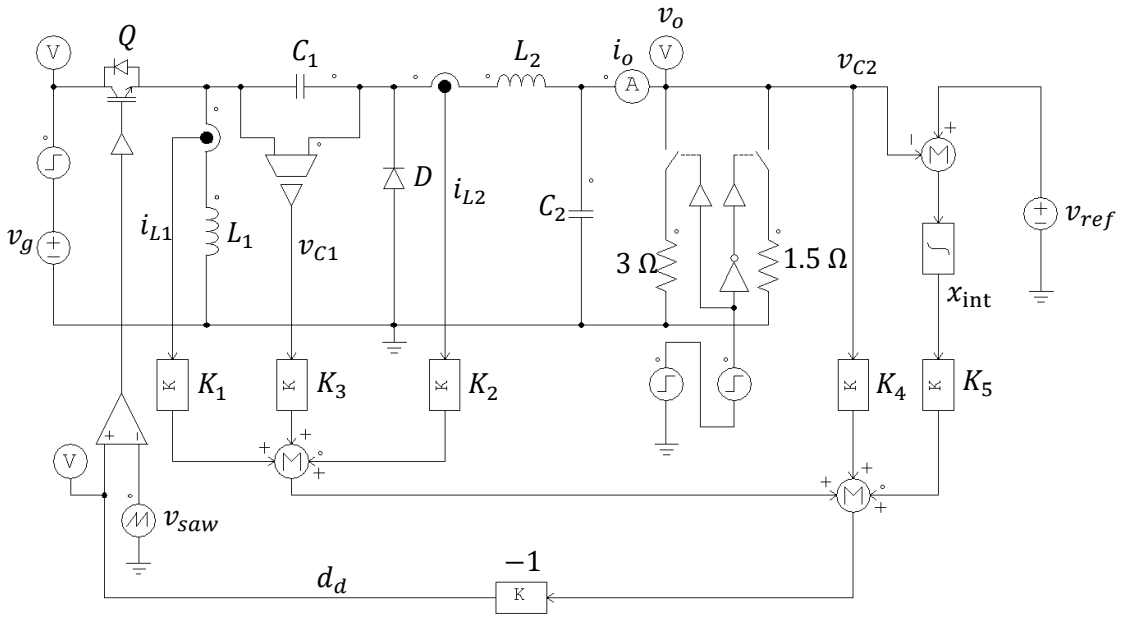

Figure 3.3: Simulation circuit of a DC-DC Zeta converter with the state-feedback controller.

The performance of the three state-feedback controllers under the nominal condition is compared in Figure 3.4. The waveforms of Figure 3.4(a), Figure 3.4(b), and Figure 3.4(c) show the output voltage v_o signal, the output current i_o signal, and the control duty ratio d_d signal, respectively. Moreover, the lines in blue, black, and red colors correspond to state-feedback controllers K_{LQR}, K_{LMI16}, and K_{LMI8}, respectively. Notice that the start-up response is omitted, and the simulated response begins in a steady-state condition. As can be seen in the figure, the initial conditions for the output voltage v_o, the load R, and the control duty ratio d_d are 9 V, 1.5 Ω (implies output current $i_o = 6\,\text{A}$), and 0.375, respectively. Note that due to high-frequency ripple propagation, the

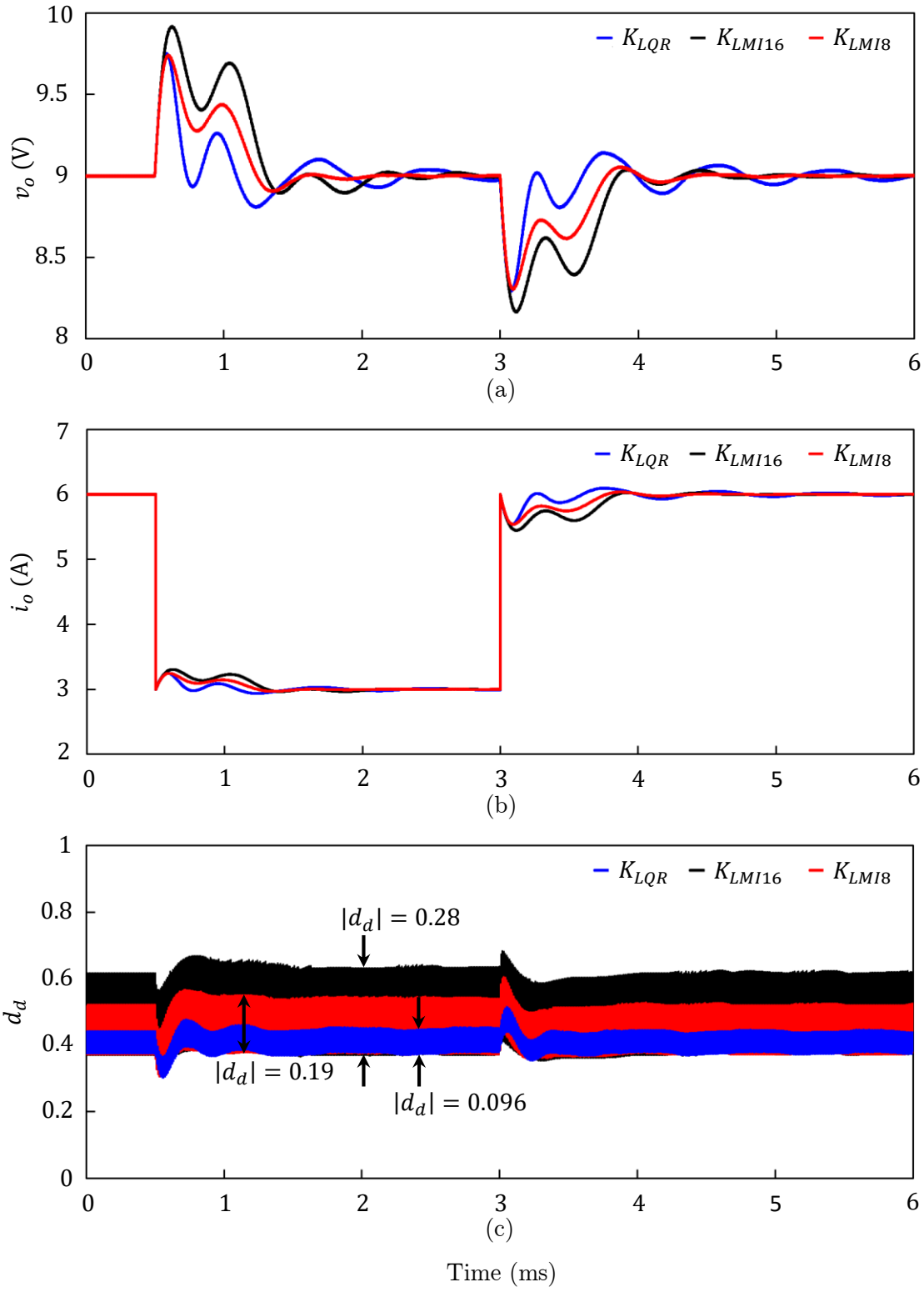

Figure 3.4: Performance comparison of the state-feedback controllers K_{LQR} (blue line), K_{LMI16} (black line), and K_{LMI8} (red line), under nominal condition. Simulated response for (a) output voltage v_o, (b) output current i_o, and (c) control duty ratio d_d.

control duty ratio appears "thick" and will be discussed shortly. At $t = 0.5\ \text{ms}$, a load perturbation occurs where the load is changed to $3\ \Omega$, evidently shown in Figure 3.4(b), where the output current is changed to $3\ \text{A}$. From the output voltage observation in Figure 3.4(a), all the three state-feedback controllers can handle the $+50\ \%$ load increment. In terms of performance, comparatively, the controller K_{LMI8} provides the best output voltage response with minimum overshoot and fastest settling time. The controller K_{LQR} produces the same amount of overshoot as K_{LMI8} but has the worst settling time. While the controller K_{LMI16} yields faster settling time than the controller K_{LQR}, the output voltage overshoot is the largest. On the other hand, at $t = 3\ \text{ms}$, the load is returned to its nominal value of $1.5\ \Omega$, which implies an output current of $6\ \text{A}$. From the figure, the output voltage response is found to be similar (but in the opposite direction) to the previous case. Concerning the control duty ratio response in Figure 3.4(c), for both instances, $t = 0.5\ \text{ms}$ and $t = 3\ \text{ms}$, all the three state-feedback controllers produced considerably small control effort to stabilize the DC-DC Zeta converter. The performance of the controllers is differentiated by the magnitude of the ripple propagated by the control duty ratio. In this case, the controller K_{LQR} propagated the least ripple at $9.6\ \%$, followed by the controller K_{LMI8} (19%), and the controller K_{LMI16} produced 28%.

In the case of the non-nominal condition, the simulation result is presented in Figure 3.5. Notice that the signals are in steady-state under the nominal condition for $0 \leq t < 0.5\ \text{ms}$ and the non-nominal condition occurs at $t = 0.5\ \text{ms}$ onwards. This is to avoid the conventional LQR controller K_{LQR} from failing to regulate the output voltage on start-up, since it is designed based on the nominal condition. At $t = 0.5\ \text{ms}$, the Zeta converter circuit is perturbed by the load, where the value is changed from $3\ \Omega$ to $1.5\ \Omega$, which implies an output current changed from $6\ \text{A}$ to $3\ \text{A}$, respectively, as depicted in Figure 3.5(b). From the output voltage response in Figure 3.5(a), comparing the performance of all three state-feedback controllers, it is observed that the controller K_{LMI8} produced a reasonable overshoot and the fastest settling time. The controller K_{LMI16} generated the largest overshoot and the settling time is slightly more than the controller K_{LMI8}, in addition to some small oscillation. Although the controller K_{LQR} gave the least overshoot, the output voltage is largely oscillating. At $t = 3\ \text{ms}$, when the load is changed back to $3\ \Omega$, the output voltage and the output current for the controller K_{LQR} deteriorated further and do not return to their respective operating point. As for the controllers K_{LMI8} and K_{LMI16}, even though the overshoot and settling time are considerably more than in the previous case, nevertheless, the output voltage is settled at its operating point. Observing the control duty ratio response in Figure 3.5(c) revealed

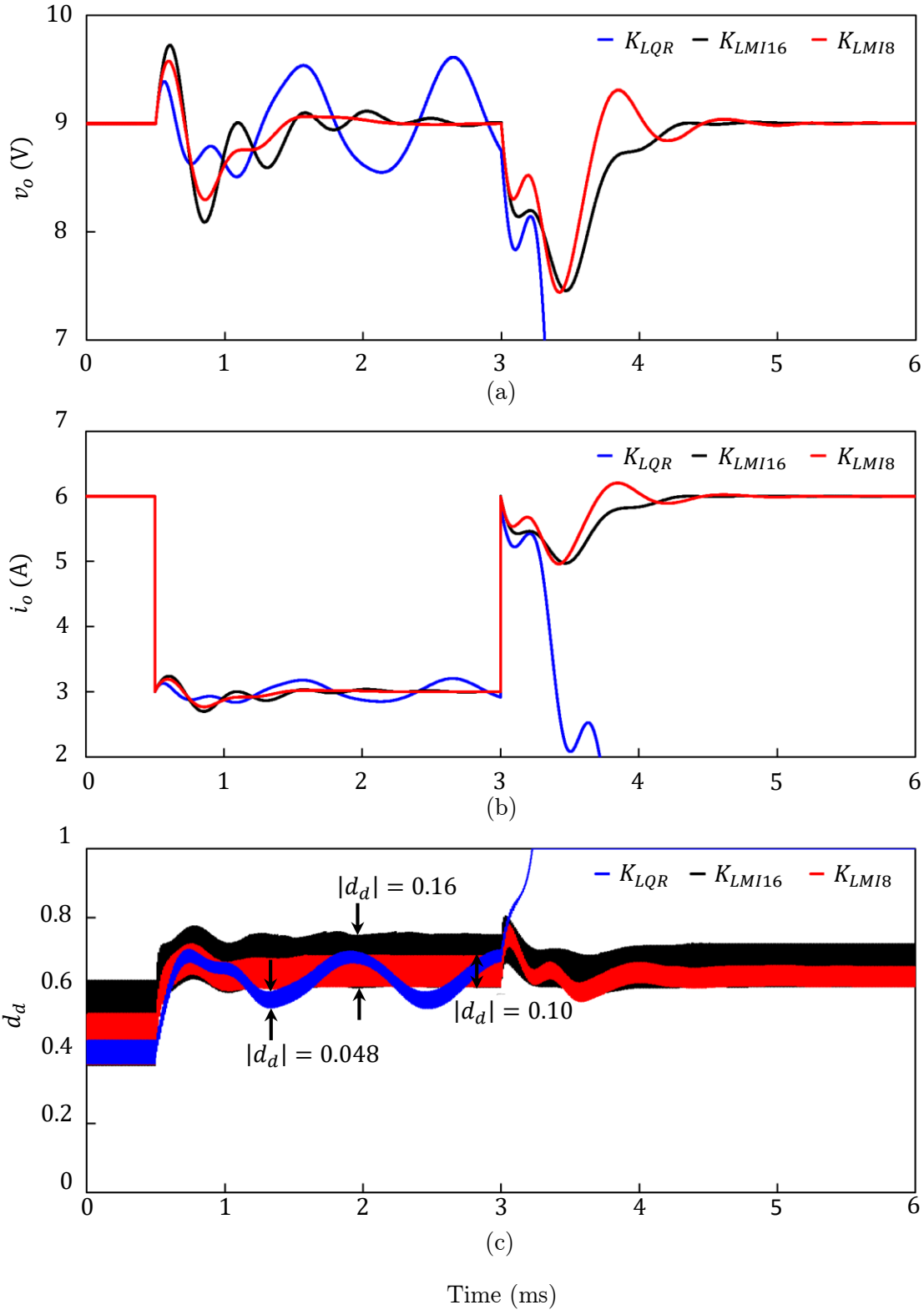

Figure 3.5: Performance comparison of the state-feedback controllers K_{LQR} (blue line), K_{LMI16} (black line), and K_{LMI8} (red line), under non-nominal condition. Simulated response for (a) output voltage v_o, (b) output current i_o, and (c) control duty ratio d_d.

that 4.8%, 10%, and 16% ripples are propagated by the controllers K_{LQR}, K_{LMI8}, and K_{LMI16}, respectively. It can be seen that only minimal control efforts are needed by the controllers K_{LMI8} and K_{LMI16} to compensate the load perturbations at $t = 0.5$ ms and $t = 3$ ms. On the contrary, the controller K_{LQR} encountered difficulties in coping with the load perturbation at $t = 0.5$ ms, and after the second load perturbation at $t = 3$ ms, the control of the Zeta converter is eventually lost, and the control duty ratio became saturated.

3.5 Summary

In this chapter, we present a control formulation based on a linear matrix inequality (LMI) from a linear quadratic regulator (LQR) problem to regulate the output voltage of a DC-DC Zeta converter. Compared with conventional LQR control which is designed for a nominal plant, our LMI-LQR control takes into account multiple plants. Furthermore, we propose a tighter version of the convex polytope of uncertainty. The conventional LQR control produces an optimal performance under the nominal condition, however, when the system is highly uncertain, the control function is lost such that it fails to bring back the state-trajectory to its operating point. Our LMI-LQR controllers performs well even under non-nominal conditions and in the presence of high load perturbation. Due to the importance of having robust control and at the same time meeting the ripple propagation limitation, it is worth highlighting the benefits of having a reduced convex polytope covering in the control design.

Chapter 4

Hybrid DC-DC Zeta Converter Control Operating in CCM

4.1 Hybrid Two-mode System Control

In this section, considering continuous conduction mode (CCM) operation of a DC-DC converter, we propose a hybrid system control strategy based on a Lyapunov functional candidate for a two-mode system and motivate its stability analysis.

Two-mode system of the same state dimension are given by

$$\frac{dx}{dt} = A_1 x + B_1 u, \tag{4.1}$$

$$\frac{dx}{dt} = A_2 x + B_2 u, \tag{4.2}$$

where $x(t) \in \mathbb{R}^n$ is the state and $u(t) \in \mathbb{R}$ is the input. Fix $u_0 \in \mathbb{R}$ and $\lambda \in \mathbb{R}$. Assume that

$$\lambda A_1 + (1-\lambda)A_2$$

is invertible. Define

$$x^* = -(\lambda A_1 + (1-\lambda)A_2)^{-1}(\lambda B_1 + (1-\lambda)B_2)u_0. \tag{4.3}$$

Note that we do not assume the stability nor the non-singularity of the matrices A_1 and A_2. Let $\mathcal{S}_i$ $(i = 1, 2)$ denote the set of stationary points of the two-mode system (4.1 and (4.2); namely

$$\mathcal{S}_1 = \{x: A_1 x + B_1 u_0 = 0\}, \mathcal{S}_2 = \{x: A_2 x + B_2 u_0 = 0\}. \tag{4.4}$$

If A_i is non-singular, $\mathcal{S}_i$ is a singleton; otherwise it may be empty or infinite. The following proposition is easy to derive, but useful in the subsequent discussions.

Proposition 1. The point x^* is given by (4.3) if and only if it satisfies the following equation:

$$\lambda(A_1x^* + B_1u_0) = -(1-\lambda)(A_2x^* + B_2u_0). \tag{4.5}$$

Furthermore, $A_ix^* + B_iu_0 \neq 0$ $(i = 1, 2)$ if and only if $\mathcal{S}_1 \cap \mathcal{S}_2 = \emptyset$.

Proof. Since

$$(\lambda A_1 + (1-\lambda)A_2)x^* = (\lambda B_1 + (1-\lambda)B_2)u_0,$$

the equivalence of (4.3) and (4.5) is immediate. If $x^{\#} \in \mathcal{S}_1 \cap \mathcal{S}_2$, then

$$\lambda\big(A_1x^{\#} + B_1u_0\big) = -(1-\lambda)\big(A_2x^{\#} + B_2u_0\big) = 0,$$

which implies $x^{\#} = x^*$ by the non-singularity of $\lambda A_1 + (1-\lambda)A_2$. Conversely, if $A_1x^* + B_1u_0 = 0$, then $A_2x^* + B_2u_0 = 0$ by (4.5)(4.5). Thus, $x^* \in \mathcal{S}_1 \cap \mathcal{S}_2$. ■

We are interested in a switching control law that drives the state of the switching system with the modes (4.1) and (4.2) to x^* under $u(t) \equiv u_0$. For this, define a candidate Lyapunov function

$$V(x) = (x - x^*)^T P(x - x^*), \tag{4.6}$$

where P is a positive definite matrix. Because $P > 0$, there exist $c_1 > 0$ and $c_2 > 0$ such that

$$c_1\|x - x^*\|^2 \leq V(x) \leq c_2\|x - x^*\|^2, \tag{4.7}$$

holds. The derivatives of $V(x)$ along the trajectories of (4.1) and (4.2) are

$$\begin{aligned}\alpha_1(x) &\coloneqq \frac{\partial V}{\partial x}(A_1x + B_1u_0)\\ &= (x - x^*)^T(PA_1 + A_1^TP)(x - x^*) + 2(A_1x^* + B_1u_0)^TP(x - x^*),\end{aligned} \tag{4.8}$$

$$\alpha_2(x) \coloneqq \frac{\partial V}{\partial x}(A_2x + B_2u_0)$$
$$= (x - x^*)^T(PA_2 + A_2^TP)(x - x^*) + 2(A_2x^* + B_2u_0)^TP(x - x^*), \tag{4.9}$$

respectively.

Proposition 2. Suppose that $PA_1 + A_1^TP \leq 0$ and $PA_2 + A_2^TP \leq 0$. Then,

$$\alpha_2^{-1}(\mathbb{R}_{\geq 0}) \subset \alpha_1^{-1}(\mathbb{R}_{\leq 0}), \quad \alpha_1^{-1}(\mathbb{R}_{\geq 0}) \subset \alpha_2^{-1}(\mathbb{R}_{\leq 0}), \tag{4.10}$$

$$\alpha_1^{-1}(0) \cap \alpha_2^{-1}(0) = \{x : x - x^* \in \ker\,(PA_1 + A_1^TP) \cap \ker\,(PA_2 + A_2^TP) \cap \ker\,(A_1x^* + B_1u_0)^TP\}. \tag{4.11}$$

The proof is based on the following observation.

Lemma 1. Let $Q_1 \leq 0$ and $Q_2 \leq 0$ be $n \times n$ symmetric matrices. Let $v_1 \in \mathbb{R}^n$ and $v_2 \in \mathbb{R}^n$ satisfy $\lambda v_1 + (1 - \lambda)v_2 = 0$ for some $0 < \lambda < 1$. Define

$$p_1(x) \coloneqq x^TQ_1x + v_1^Tx, p_2(x) \coloneqq x^TQ_2x + v_2^Tx.$$

Then

$$p_1^{-1}(\mathbb{R}_{\leq 0}) \subset p_2^{-1}(\mathbb{R}_{\geq 0}), p_2^{-1}(\mathbb{R}_{\leq 0}) \subset p_2^{-1}(\mathbb{R}_{\geq 0}),$$
$$p_1^{-1}(0) \cap p_2^{-1}(0) = \ker Q_1 \cap \ker Q_2 \cap \ker v_1^T.$$

Proof. If $p_1(x) > 0$, then

$$0 < \lambda p_1(x) = \lambda x^TQ_1x + \lambda v_1^Tx$$
$$\leq \lambda v_1^Tx = -(1 - \lambda)v_2^Tx$$
$$\leq -(1 - \lambda)x^TQ_2x - (1 - \lambda)v_2^Tx = -(1 - \lambda)p_2(x)$$

holds. Thus, $p_2(x) < 0$. Because $p_1^{-1}(\mathbb{R}_{\leq 0}) = \mathbb{R}^n \setminus p_1^{-1}(\mathbb{R}_{>0})$ and $p_2^{-1}(\mathbb{R}_{\geq 0}) = \mathbb{R}^n \setminus p_2^{-1}(\mathbb{R}_{<0})$, $p_2^{-1}(\mathbb{R}_{\geq 0}) \subset p_1^{-1}(\mathbb{R}_{\leq 0})$. By interchanging p_1 and p_2, in the argument, it follows that $p_1^{-1}(\mathbb{R}_{\geq 0}) \subset p_2^{-1}(\mathbb{R}_{\leq 0})$. If $p_1(x) = p_2(x) = 0$, then

$$0 = \lambda p_1(x) = \lambda x^TQ_1x + \lambda v_1^Tx$$
$$\leq \lambda v_1^Tx = -(1 - \lambda)v_2^Tx$$
$$\leq -(1 - \lambda)x^TQ_2x - (1 - \lambda)v_2^Tx = -(1 - \lambda)p_2(x) = 0.$$

Hence all the inequalities hold as equalities. This implies $v_1^T x = 0$, $x^T Q_1 x = 0$, and $x^T Q_2 x = 0$, which means $x \in \ker Q_1 \cap \ker Q_2 \cap \ker v_1^T$. Conversely, if $x \in \ker Q_1 \cap \ker Q_2 \cap \ker v_1^T$, then $x \in \ker v_2^T$ and $p_1(x) = p_2(x) = 0$. ■

Proof of Proposition 2. Define

$$\begin{aligned} Q_1 &\coloneqq PA_1 + A_1^T P, & Q_2 &\coloneqq PA_2 + A_2^T P, \\ v_1 &\coloneqq 2P(A_1 x^* + B_1 u_0), & v_2 &\coloneqq 2P(A_2 x^* + B_2 u_0), \\ p_1(x) &\coloneqq \alpha_1(x + x^*), & p_2(x) &\coloneqq \alpha_2(x + x^*). \end{aligned}$$

Notice that the assumptions of Lemma 1 are satisfied since (4.5) holds. Then the proof is immediate from Lemma 1. ■

Based on Proposition 2, we propose the following hybrid system control strategy.

Hybrid CCM System Control Strategy 1

- If the system is operating in mode 1 and reaches $\alpha_1^{-1}(0)$, then it switches to mode 2.
- If the system is operating in mode 2 and reaches $\alpha_2^{-1}(0)$, then it switches to mode 1.

To analyze the stability of the Hybrid CCM System Control Strategy 1, we consider the differential inclusion

$$\frac{dx}{dt} \in F(x), \tag{4.12}$$

$$F(x) \coloneqq \begin{cases} \{A_1 x + B_1 u_0\} & \text{if } x \in M_1, \\ \{A_2 x + B_2 u_0\} & \text{if } x \in M_2, \\ \operatorname{conv}\{A_1 x + B_1 u_0, A_2 x + B_2 u_0\} & \text{if } x \in M_0, \end{cases}$$

where

$$\begin{aligned} M_1 &= \{x: \alpha_1^{-1}(\mathbb{R}_{<0}) \cap \alpha_2^{-1}(\mathbb{R}_{>0}) = \alpha_1^{-1}(\mathbb{R}_{<0})\}, \\ M_2 &= \{x: \alpha_1^{-1}(\mathbb{R}_{>0}) \cap \alpha_2^{-1}(\mathbb{R}_{<0}) = \alpha_2^{-1}(\mathbb{R}_{<0})\}, \\ M_0 &= \{x: \alpha_1^{-1}(\mathbb{R}_{\leq 0}) \cap \alpha_2^{-1}(\mathbb{R}_{\leq 0})\}. \end{aligned}$$

The set-valued map $F: \mathbb{R}^n \rightsquigarrow \mathbb{R}^n$ is upper semi-continuous, and its values are bounded closed convex sets. Solutions of (4.12) include solutions of (4.1), (4.2) with the hybrid

system control strategy. We shall analyze the stability of the operating point x^* of the differential inclusion (4.12).

4.2 Stability of Hybrid System Control

In this section, we will analyze the stability of the hybrid system control strategy proposed in the previous section and apply the method to a DC-DC Zeta converter operating in CCM.

4.2.1 Stability Analysis

Consider the differential inclusion (4.12) and the function $V(x)$ in (4.6). Define $\dot{V}(x)\colon \mathbb{R}^n \rightsquigarrow \mathbb{R}$ by

$$\dot{V}(x) = \frac{\partial V}{\partial x} F(x) \coloneqq \left\{ \frac{\partial V}{\partial x} \omega \colon \omega \in F(x) \right\}.$$

It is easy to verify that

$$\dot{V}(x) = \begin{cases} \{\alpha_1(x)\} & \text{if } x \in M_1, \\ \{\alpha_2(x)\} & \text{if } x \in M_2, \\ \operatorname{conv}\{\alpha_1(x), \alpha_2(x)\} & \text{if } x \in M_0. \end{cases} \tag{4.13}$$

The inverse image $\dot{V}^{-1}(S)$, where $S \subset \mathbb{R}$, is defined by

$$\dot{V}^{-1}(S) \coloneqq \left\{ y \in \mathbb{R}^n \colon \dot{V}(y) \cap S \neq \emptyset \right\}.$$

When $S = \{a\}$, we write $\dot{V}^{-1}(a) \coloneqq \dot{V}^{-1}(\{a\})$.

Proposition 3. Consider the differential inclusion (4.12) and the Lyapunov function (4.6). Then,

$$\dot{V}^{-1}(0) = \alpha_1^{-1}(0) \cup \alpha_2^{-1}(0).$$

Proof. If $x \in \alpha_1^{-1}(0)$, then $\dot{V}(x) = \operatorname{conv}\{0, \alpha_2(x)\} \ni 0$. Similarly, we have $0 \in \dot{V}(x)$ if $x \in \alpha_2^{-1}(0)$. Hence $\dot{V}^{-1}(0) \supset \alpha_1^{-1}(0) \cup \alpha_2^{-1}(0)$. Conversely, if $0 \in \dot{V}(x)$, then $x \in \alpha_1^{-1}(\mathbb{R}_{\leq 0}) \cap \alpha_2^{-1}(\mathbb{R}_{\leq 0})$ and $0 \in \operatorname{conv}\{\alpha_1(x), \alpha_2(x)\}$. Because $\alpha_1(x) \leq 0$ and $\alpha_2(x) \leq$

0, this implies either $\alpha_1(x) = 0$ or $\alpha_2(x) = 0$. ■

Proposition 4. Let x^*, $\mathcal{S}_1$, and $\mathcal{S}_2$ be defined by (4.3) and (4.4). Then $\{x^*\} \cup \mathcal{S}_1 \subset \alpha_2^{-1}(0)$ hold.

Proof. We have already shown that $x^* \in \alpha_1^{-1}(0) \cap \alpha_2^{-1}(0)$ in Proposition 2. If $x \in \mathcal{S}_1$, then $\alpha_1(x) = 0$ by (4.8). Similarly, if $x \in \mathcal{S}_2$, then $\alpha_2(x) = 0$. ■

Proposition 5. Let $x^{\#} \in \{x^*\} \cup \mathcal{S}_1 \cup \mathcal{S}_2$. Then, the differential inclusion (4.12) has a stationary solution $\phi(t, x^{\#}) \equiv x^{\#}$.

Proof. If $x^{\#} \in \mathcal{S}_1$, then $\alpha_1(x^{\#}) = 0$ by Proposition 4. Thus $F(x^{\#}) = \text{conv}\{0, A_2x^{*1} + B_2u_0\} \ni 0$. Similarly, $x^{\#} \in \mathcal{S}_2$ implies $0 \in F(x^{\#})$. By Proposition 4, $\alpha_1(x^*) = \alpha_2(x^*) = 0$. Consequently, $F(x^*) = \text{conv}\{A_1x^* + B_1u_0, A_2x^* + B_2u_0\} \ni \lambda(A_1x^* + B_1u_0) + (1 - \lambda)(A_2x^* + B_2u_0) = 0$ ■

By Proposition 5, the operation point x^* is not globally asymptotically stable if $\mathcal{S}_1 \cup \mathcal{S}_2 \neq \emptyset$. We shall study the local asymptotic stability of x^*. The next result shows that x^* is stable in this sense.

Theorem 1. Suppose that $PA_1 + A_1^TP \leq 0$ and $PA_2 + A_2^TP \leq 0$ hold. If $\alpha_1^{-1}(0) \cap \alpha_2^{-1}(0)$ contains no solution of (4.12) except for $x(t) \equiv x^*$, then x^* is locally asymptotically stable.

The proof of Theorem 1 hinges on a couple of Lemmas. The first one states that the operating point x^* is stable.

Lemma 2. Suppose that $PA_1 + A_1^TP \leq 0$ and $PA_2 + A_2^TP \leq 0$ hold. Then x^* is stable.

Proof. Note that the set-valued function $F(x)$ in (4.12) is defined for all $x \in \mathbb{R}^n$ from (4.10) in Proposition 2. Let $\varepsilon > 0$, and choose $\delta = \frac{\varepsilon c_1}{c_2} > 0$. If $\|x_0 - x^*\|^2 < \delta$, it follows from (4.7) that $V(x_0) \leq c_2\delta = c_1\varepsilon$. Along the trajectory $\phi(t, x_0)$ of (4.12), it holds that

$$\frac{d}{dt}V(\phi(t, x_0)) = \dot{V}(\phi(t, x_0)) \subset \mathbb{R}_{\leq 0},$$

by (4.13), and hence $V(\phi(t, x_0)) \leq V(x_0)$ holds. This implies that $\|\phi(t, x_0) - x^*\|^2 \leq \varepsilon$,

and therefore x^* is stable. ■

One of the important observations is the property of the limiting set of a solution of a differential inclusion with an upper semi-continuous set-valued map. Let

$$\frac{dx}{dt} \in F(x), \tag{4.14}$$

be a differential inclusion where $F: \mathbb{R}^n \twoheadrightarrow \mathbb{R}^n$ is upper semi-continuous and its values are bounded closed convex sets. Let $\phi(t, x_0)$ be a solution of (4.14). A point $\omega \in \mathbb{R}^n$ is called a limit point of $\phi(t, x_0)$ if there is a sequence $\{t_k\}$ in $[0, \infty)$ such that $t_k \to \infty$ and

$$\lim_{k\to\infty} \phi(t_k, x_0) = \omega.$$

The set of all limit points of $\phi(t, x_0)$ is called the limit set of $\phi(t, x_0)$ and is denoted as Ω.

Lemma 3. Consider the differential inclusion (4.14). Suppose that a solution $\phi(t, x_0)$ is bounded. Then the limit set Ω is nonempty, closed, and bounded. Furthermore, if $\omega \in \Omega$, then there exists a solution of $\phi(t, \omega)$ of (4.14) with initial condition $x(0) = \omega$ satisfying $\phi(t, \omega) \in \Omega$ for all $t \geq 0$.

Proof. The first half is elementary, see for example [50, Lemma 5.30]. To prove the second half, let $\{t_k\}$ be a sequence in $[0, \infty)$ such that $t_k \to \infty$ and $\omega_k := \phi(t_k, x_0)$ tends to $\omega \in \Omega$. Let $T > 0$ be fixed, and define $\psi_k(t) := \phi(t + t_k, x_0)$ for $t \in [0, T]$. Note that $\psi_k(t)$ is a solution of (4.14) with the initial condition $x(0) = \omega_k$. Using a similar argument as in [51, p.13, Theorem 4] and [51, p.104, Theorem 1], one can prove there exists ψ and a convergent subsequence of $\{\psi_k\}$ where the limit is ψ, and $\psi(t) = \phi(t, \omega)$ is a solution of the differential inclusion (4.14) with the initial condition $x(0) = \omega$. Then any point on $\psi(t)$ is a limit point of $\phi(t, x_0)$ and hence $\phi(t, \omega) \in \Omega$ for $0 \leq t \leq T$. Since this is true for any $T > 0$, this concludes the proof. ■

Lemma 4. There exists $r > 0$ such that for every ω in the set $\left\{\left(\alpha_1^{-1}(0) \setminus \alpha_2^{-1}(0)\right) \cup \left(\alpha_2^{-1}(0) \setminus \alpha_1^{-1}(0)\right)\right\} \cap \{x: V(x) < r\}$ and every solution $\phi(t, \omega)$ of (4.14), there exists $\tau > 0$ such that $V\big(\phi(\tau, \omega)\big) < V(\omega)$.

Proof. Define

$$\dot{\alpha}_1(x) \coloneqq \frac{\partial \alpha_1(x)}{\partial x}(A_1 x + B_1 u_0),$$

and recall from (4.9) that

$$\frac{\partial \alpha_1(x)}{\partial x} = 2((x - x^*)^T(PA_1 + A_1^T P) + (A_1 x^* + B_1 u_0)^T P).$$

It follows that $\dot{\alpha}_1(x)$ is a continuous function; moreover,

$$\dot{\alpha}_1(x^*) = (A_1 x^* + B_1 u_0)^T P(A_1 x^* + B_1 u_0) > 0,$$

and from the continuity of $\dot{\alpha}_1(x)$, $\dot{\alpha}_1(x) > 0$ in some neighborhood of x^*, say $N = \{x: V(x) < r\}$ for some $r > 0$. Let $\omega \in \left(\alpha_1^{-1}(0) \setminus \alpha_2^{-1}(0)\right) \cap N$. Since $\alpha_1(\omega) = 0$, $\alpha_2(\omega) < 0$ by (10). We can take $\tau > 0$ small enough, so $\alpha_2\big(\phi(\tau, \omega)\big) < 0$ for all $t \in [0, \tau]$. If $V\big(\phi(t, \omega)\big) = V(\omega)$ for all $t \in [0, \tau]$, then

$$\frac{d}{dt}V(\phi(t, \omega)) = \frac{\partial V}{\partial x}\frac{d}{dt}\phi(t, \omega) = 0, \tag{4.15}$$

for almost all t. Let $\mathcal{T} = \big\{t: \alpha_1\big(\phi(\tau, \omega)\big) > 0\big\}$. Note that $\mathcal{T}$ is an open set. If $t \in \mathcal{T}$, then by (4.12) $F\big(\phi(\tau, \omega)\big) = \{A_2\phi(\tau, \omega) + B_2 u_0\}$, and hence $\frac{\partial V}{\partial x}\frac{d}{dt}\phi(t, \omega) = \alpha_2\big(\phi(\tau, \omega)\big) < 0$. Hence $\mathcal{T} = \emptyset$. Consequently, $F\big(\phi(\tau, \omega)\big) = \operatorname{conv}\{A_1\phi(\tau, \omega) + B_1 u_0, A_2\phi(\tau, \omega) + B_2 u_0\}$, but $\frac{\partial V}{\partial x}A_2\phi(\tau, \omega) + B_2 u_0 = \alpha_2\big(\phi(\tau, \omega)\big) < 0$ implies $\frac{d}{dt}\phi(\tau, \omega) = A_1\phi(\tau, \omega) + B_1 u_0$ for almost all t. Hence $\phi(\tau, \omega)$ is the solution of the differential equation

$$\frac{dx}{dt} = A_1 x + B_1 u_0, \quad x(0) = \omega, \quad 0 \le t \le \tau,$$

$V(\phi(t, \omega))$ is twice continuously differentiable, and

$$\frac{d^2}{dt^2}V(\phi(t, \omega)) = \dot{\alpha}_1(\phi(t, \omega)) > 0, \qquad t \in [0, \tau].$$

This implies that $\alpha_1\big(\phi(t, \omega)\big) > \alpha_1\big(\phi(0, \omega)\big) = 0$ for some t. But $\mathcal{T} = \emptyset$, and this is not possible. Hence, $V(\phi(\tau, \omega)) \le V\big(\phi(t, \omega)\big) < V(\omega)$ for some $t \in [0, \tau]$. The proof for $\omega \in \left(\alpha_2^{-1}(0) \setminus \alpha_1^{-1}(0)\right) \cap N$ is similar. ■

Proof of Theorem 1. Since $\phi(t, x_0)$ is bounded, its limit set Ω is an invariant set by Lemma 3. Since $V(x)$ is bounded from below and $V\big(\phi(t, x_0)\big)$ is monotonically non-increasing for every sequence $\{t_k\}$ such that $t_k \to \infty$ as $k \to \infty$, $c \coloneqq \lim_{k\to\infty} V\big(\phi(t_k, x_0)\big)$ exists. If $\omega \in \Omega$, then there exists a sequence $\{t_k\}$ such that $\omega = \lim \phi(t_k, x_0)$. This means $V(\omega) = V(\lim \phi(t_k, x_0)) = \lim V\big(\phi(t_k, x_0)\big) = c$. Because Ω is an invariant set, $0 \in V(\omega)$ for any $\omega \in \Omega$. From Proposition 3, $\omega \in \alpha_1^{-1}(0) \cup \alpha_2^{-1}(0)$. Take $r > 0$ and $N = \{x: V(x) < r\}$ as in Lemma 4. If $\omega \in \left\{\left(\alpha_1^{-1}(0) \setminus \alpha_2^{-1}(0)\right) \cup \left(\alpha_2^{-1}(0) \setminus \alpha_1^{-1}(0)\right)\right\} \cap N$, then ω is not a limit point by Lemma 4. Thus, $\omega \in \alpha_1^{-1}(0) \cap \alpha_2^{-1}(0)$. Hence, if $V(x_0) < r$, then $\phi(t, x_0)$ does not have a limit point except x^*. ■

Remark 1. Theorem 1 is a consequence of LaSalle's invariance principle proved for the differential inclusion (4.12). This is a useful tool to prove the stability of the hybrid system control applied to a DC-DC Zeta converter in Section 4.3.2.

4.2.2 Stability of Hybrid Zeta Converter Control in CCM

As presented in Section 2.2, for the state vector $x = [i_{L1}\ i_{L2}\ v_{C1}\ v_{C2}]^T$ and the input $u = v_g$, the matrices for a DC-DC Zeta converter operating in CCM are given by

$$A_1 = \begin{bmatrix} 0 & 0 & 0 & 0 \\ 0 & 0 & \frac{1}{L_2} & -\frac{1}{L_2} \\ 0 & -\frac{1}{C_1} & 0 & 0 \\ 0 & \frac{1}{C_2} & 0 & -\frac{1}{RC_2} \end{bmatrix}, \quad B_1 = \begin{bmatrix} \frac{1}{L_1} \\ \frac{1}{L_2} \\ 0 \\ 0 \end{bmatrix},$$

$$A_2 = \begin{bmatrix} 0 & 0 & -\frac{1}{L_1} & 0 \\ 0 & 0 & 0 & -\frac{1}{L_2} \\ \frac{1}{C_1} & 0 & 0 & 0 \\ 0 & \frac{1}{C_2} & 0 & -\frac{1}{RC_2} \end{bmatrix}, \quad B_2 = \begin{bmatrix} 0 \\ 0 \\ 0 \\ 0 \end{bmatrix}. \tag{4.16}$$

If $u_0 > 0$, then mode 1 has no stationary solution, and mode 2 has a unique stationary solution $x^{*2} = [0 \quad 0 \quad 0 \quad 0]^T$.

For $\lambda \in (0,1)$,

$$x^* = -(\lambda A_1 + (1-\lambda)A_2)^{-1}(\lambda B_1 + (1-\lambda)B_2)u_0$$

$$= \begin{bmatrix} 0 & 0 & -\frac{1-\lambda}{L_1} & 0 \\ 0 & 0 & \frac{\lambda}{L_2} & -\frac{1}{L_2} \\ \frac{1-\lambda}{C_1} & -\frac{\lambda}{C_1} & 0 & 0 \\ 0 & \frac{1}{C_2} & 0 & -\frac{1}{RC_2} \end{bmatrix} \begin{bmatrix} \frac{\lambda}{L_1} \\ \frac{\lambda}{L_2} \\ 0 \\ 0 \end{bmatrix} u_0$$

$$= \begin{bmatrix} \frac{v_r^2}{Rv_g} \\ \frac{v_r}{R} \\ v_r \\ v_r \end{bmatrix} =: \begin{bmatrix} i_{L1}^* \\ i_{L2}^* \\ v_{C1}^* \\ v_{C2}^* \end{bmatrix}, \tag{4.17}$$

where $v_g := u_0$ and $v_r := \frac{\lambda u_0}{1-\lambda}$. Based on the energy stored in the inductors and the capacitors of the Zeta converter, define

$$P := \begin{bmatrix} \frac{L_1}{2} & 0 & 0 & 0 \\ 0 & \frac{L_2}{2} & 0 & 0 \\ 0 & 0 & \frac{C_1}{2} & 0 \\ 0 & 0 & 0 & \frac{C_2}{2} \end{bmatrix}. \tag{4.18}$$

Then

$$PA_1 + A_1^T P = \begin{bmatrix} 0 & 0 & 0 & 0 \\ 0 & 0 & 0 & 0 \\ 0 & 0 & 0 & 0 \\ 0 & 0 & 0 & -\frac{1}{R} \end{bmatrix} \leq 0,$$

$$PA_2 + A_2^T P = \begin{bmatrix} 0 & 0 & 0 & 0 \\ 0 & 0 & 0 & 0 \\ 0 & 0 & 0 & 0 \\ 0 & 0 & 0 & -\frac{1}{R} \end{bmatrix} \leq 0,$$

$$(A_1 x^* + B_1 u_0)^T P = \begin{bmatrix} \frac{v_g}{2} & \frac{v_g}{2} & -\frac{v_r}{2R} & 0 \end{bmatrix},$$

$$(A_2 x^* + B_2 u_0)^T P = \begin{bmatrix} -\frac{v_r}{2} & -\frac{v_r}{2} & -\frac{v_r^2}{2Rv_g} & 0 \end{bmatrix}. \tag{4.19}$$

From (4.19),

$$\ker (PA_1 + A_1^T P) \cap \ker (PA_2 + A_2^T P) \cap \ker (A_1 x^* + B_1 u_0)^T P = \operatorname{span} \{d_1, d_2\},$$

where

$$d_1 = \begin{bmatrix} \frac{v_r}{R} \\ 0 \\ v_g \\ 0 \end{bmatrix}, \qquad d_2 = \begin{bmatrix} 0 \\ \frac{v_r}{R} \\ v_g \\ 0 \end{bmatrix}. \tag{4.20}$$

The function $\dot{V}(x)$ decreases along the trajectory as long as $x \notin \alpha_1^{-1}(0) \cap \alpha_2^{-1}(0)$. It remains to see what happens when the trajectory reaches $\alpha_1^{-1}(0) \cap \alpha_2^{-1}(0)$.

Lemma 5. Let $x \in \alpha_1^{-1}(0) \cap \alpha_2^{-1}(0)$. Then the following properties hold:

(a) $0 \in F(x)$ if and only if $x = x^*$.
(b) if $x - x^* \notin \text{span}\{d_1\}$, then $F(x) \cap \ker(PA_1 + A_1^T P) \cap \ker(PA_2 + A_2^T P) \neq \emptyset$.
(c) if $x - x^* \in \text{span}\{d_1\}$, and $x \neq x^*$, then $F(x) \cap \text{span}\{d_1\} \neq \emptyset$.

Proof. It follows from (4.17) that

$$A_1 x^* + B_1 v_g = \begin{bmatrix} 0 \\ 0 \\ -\frac{v_r}{C_1 R} \\ 0 \end{bmatrix} + \begin{bmatrix} \frac{v_g}{L_1} \\ \frac{v_g}{L_2} \\ 0 \\ 0 \end{bmatrix} = \begin{bmatrix} \frac{v_g}{L_1} \\ \frac{v_g}{L_2} \\ -\frac{v_r}{C_1 R} \\ 0 \end{bmatrix}, \tag{4.21}$$

$$A_2 x^* + B_2 v_g = \begin{bmatrix} -\frac{v_r}{L_1} \\ -\frac{v_r}{L_2} \\ \frac{v_r^2}{C_1 R v_g} \\ 0 \end{bmatrix} + \begin{bmatrix} 0 \\ 0 \\ 0 \\ 0 \end{bmatrix} = \begin{bmatrix} -\frac{v_r}{L_1} \\ -\frac{v_r}{L_2} \\ \frac{v_r^2}{C_1 R v_g} \\ 0 \end{bmatrix}. \tag{4.22}$$

Note that $x \in \alpha_1^{-1}(0) \cap \alpha_2^{-1}(0)$ if and only if $x = x^* + \Delta x$ with

$$\Delta x = \delta_1 d_1 + \delta_2 d_2 = \begin{bmatrix} \delta_1 \frac{v_r}{R} \\ \delta_2 \frac{v_r}{R} \\ (\delta_1 + \delta_2) v_g \\ 0 \end{bmatrix}. \tag{4.23}$$

From this, it follows that

$$A_1 \Delta x = \begin{bmatrix} 0 \\ (\delta_1 + \delta_2) \frac{v_g}{L_2} \\ -\delta_2 \frac{v_r}{C_1 R} \\ \delta_2 \frac{v_r}{C_2 R} \end{bmatrix}, \quad A_2 \Delta x = \begin{bmatrix} -(\delta_1 + \delta_2) \frac{v_g}{L_1} \\ 0 \\ \delta_1 \frac{v_r}{C_1 R} \\ \delta_2 \frac{v_r}{C_2 R} \end{bmatrix}.$$

Hence if $x \in \alpha_1^{-1}(0) \cap \alpha_2^{-1}(0)$, then

$$A_1 x + B_1 v_g = A_1 x^* + B_1 v_g + A_1 \Delta x = \begin{bmatrix} \frac{v_g}{L_1} \\ \frac{v_g}{L_2} \\ -\frac{v_r}{C_1 R} \\ 0 \end{bmatrix} + \begin{bmatrix} 0 \\ (\delta_1 + \delta_2)\frac{v_g}{L_2} \\ -\delta_2 \frac{v_r}{C_1 R} \\ \delta_2 \frac{v_r}{C_2 R} \end{bmatrix}, \tag{4.24}$$

$$A_2 x + B_2 v_g = A_2 x^* + B_2 v_g + A_2 \Delta x = \begin{bmatrix} -\frac{v_r}{L_1} \\ -\frac{v_r}{L_2} \\ \frac{v_r^2}{C_1 R v_g} \\ 0 \end{bmatrix} + \begin{bmatrix} -(\delta_1 + \delta_2)\frac{v_g}{L_1} \\ 0 \\ \delta_1 \frac{v_r}{C_1 R} \\ \delta_2 \frac{v_r}{C_2 R} \end{bmatrix}, \tag{4.25}$$

Hence if $\omega \in F(x)$ for $x \in \alpha_1^{-1}(0) \cap \alpha_2^{-1}(0) \setminus \text{span}\{d_1\}$, then

$$[0 \quad 0 \quad 0 \quad 1]\omega = \frac{\delta_2 v_r}{C_2 R} \neq 0,$$

which shows $F(x) \cap \ker(PA_1 + A_1^T P) \cap \ker(PA_2 + A_2^T P) \neq \emptyset$ and $0 \notin \text{conv}\{A_1 x + B_1 v_g, A_2 x + B_2 v_g\}$. Suppose $x - x^* \in \text{span}\{d_1\}$, then,

$$\begin{aligned} \text{rank}\begin{bmatrix} (A_1 x + B_1 v_g) & (A_2 x + B_2 v_g) \end{bmatrix} &= \text{rank}\begin{bmatrix} \frac{v_g}{L_1} & -\frac{v_r}{L_1} - \delta_1 \frac{v_g}{L_1} \\ \frac{v_g}{L_2} + \delta_1 \frac{v_g}{L_2} & -\frac{v_r}{L_2} \\ -\frac{v_r}{C_1 R} & \frac{v_r^2}{C_1 R v_g} + \delta_1 \frac{v_r}{C_1 R} \end{bmatrix} \\ &= \text{rank}\begin{bmatrix} \frac{v_g}{L_1} & -\delta_1 \frac{v_g}{L_1} \\ \frac{v_g}{L_2} + \delta_1 \frac{v_g}{L_2} & \delta_1 \frac{v_r}{L_2} \\ -\frac{v_r}{C_1 R} & \delta_1 \frac{v_r}{C_1 R} \end{bmatrix} \\ &= \text{rank}\begin{bmatrix} \frac{v_g}{L_1} & -\frac{v_g}{L_1} \\ \frac{v_g}{L_2} + \delta_1 \frac{v_g}{L_2} & \frac{v_r}{L_2} \\ -\frac{v_r}{C_1 R} & \frac{v_r}{C_1 R} \end{bmatrix} \\ &= \text{rank}\begin{bmatrix} 0 & -\frac{v_g}{L_1} \\ \frac{v_r + v_g}{L_2} + \delta_1 \frac{v_g}{L_2} & \frac{v_r}{L_2} \\ 0 & \frac{v_r}{C_1 R} \end{bmatrix}. \end{aligned}$$

If $\delta_1 \neq -\frac{v_r+v_g}{v_g}$, then $A_1x + B_1v_g$ and $A_2x + B_2v_g$ are linearly independent, and hence $0 \notin F(x)$. If $\delta_1 = -\frac{v_r+v_g}{v_g}$, then

$$x = x^* + \Delta x = \begin{bmatrix} \frac{v_r^2}{Rv_g} \\ \frac{v_r}{R} \\ v_r \\ v_r \end{bmatrix} + \begin{bmatrix} -\frac{v_r+v_g}{v_g}\left(\frac{v_r}{R}\right) \\ 0 \\ -\frac{v_r+v_g}{v_g}(v_g) \\ 0 \end{bmatrix} = \begin{bmatrix} -\frac{v_r}{R} \\ \frac{v_r}{R} \\ -v_g \\ v_r \end{bmatrix},$$

$$A_1x + B_1v_g = \begin{bmatrix} \frac{v_g}{L_1} \\ \frac{v_g}{L_2} \\ -\frac{v_r}{C_1R} \\ 0 \end{bmatrix} + \begin{bmatrix} 0 \\ -\frac{v_r+v_g}{v_g}\left(\frac{v_g}{L_2}\right) \\ 0 \\ 0 \end{bmatrix} = \begin{bmatrix} \frac{v_g}{L_1} \\ -\frac{v_r}{L_2} \\ -\frac{v_r}{C_1R} \\ 0 \end{bmatrix},$$

$$A_2x + B_2v_g = \begin{bmatrix} -\frac{v_r}{L_1} \\ -\frac{v_r}{L_2} \\ \frac{v_r^2}{C_1Rv_g} \\ 0 \end{bmatrix} + \begin{bmatrix} \frac{v_r+v_g}{v_g}\left(\frac{v_g}{L_1}\right) \\ 0 \\ -\frac{v_r+v_g}{v_g}\left(\frac{v_r}{C_1R}\right) \\ 0 \end{bmatrix} = \begin{bmatrix} \frac{v_g}{L_1} \\ -\frac{v_r}{L_2} \\ -\frac{v_r}{C_1R} \\ 0 \end{bmatrix}.$$

Because $A_1x + B_1v_g = A_2x + B_2v_g \neq 0$, we have $0 \notin F(x)$. Finally, note that

$$\Delta x^T P(A_1x + B_1v_g) = \begin{bmatrix} \delta_1\frac{L_1v_r}{2R} & \delta_2\frac{L_2v_r}{2R} & (\delta_1+\delta_2)\frac{C_1v_g}{2} & 0 \end{bmatrix} \left\{ \begin{bmatrix} \frac{v_g}{L_1} \\ \frac{v_g}{L_2} \\ -\frac{v_r}{C_1R} \\ 0 \end{bmatrix} + \begin{bmatrix} 0 \\ (\delta_1+\delta_2)\frac{v_g}{L_2} \\ -\delta_2\frac{v_r}{C_1R} \\ \delta_2\frac{v_r}{C_2R} \end{bmatrix} \right\}$$

$$= 0,$$

$$\Delta x^T P(A_2x + B_2v_g) = \begin{bmatrix} \delta_1\frac{L_1v_r}{2R} & \delta_2\frac{L_2v_r}{2R} & (\delta_1+\delta_2)\frac{C_1v_g}{2} & 0 \end{bmatrix} \left\{ \begin{bmatrix} \frac{v_r}{L_1} \\ \frac{v_r}{L_2} \\ -\frac{v_r}{C_1Rv_g} \\ 0 \end{bmatrix} + \begin{bmatrix} -(\delta_1+\delta_2)\frac{v_g}{L_1} \\ 0 \\ \delta_1\frac{v_r}{C_1R} \\ \delta_2\frac{v_r}{C_2R} \end{bmatrix} \right\}$$

$$= 0.$$

Let $x - x^* \in \text{span}\{d_1\}$ and $x \neq x^*$. Then for every $\omega \in F(x)$, $d_1^T P\omega = 0$. Since $0 \notin F(x)$, it follows that $F(x) \cap \text{span}\{d_1\} = \emptyset$. ■

Theorem 2. Consider the differential inclusion (4.12) defined by the system matrices (4.16) and the operating point x^* in (4.17). Then, the operating point x^* is local

asymptotically stable.

Proof. Assume that $\phi(t, x_0)$ is a solution of the differential inclusion satisfying $\phi(t, x_0) \in \alpha_1^{-1}(0) \cap \alpha_2^{-1}(0)$ for $t \geq 0$ and $x_0 \neq x^*$. If $x_0 - x^* \notin \text{span}\{d_1\}$, then $\frac{d}{dt}\phi(t, x_0) \notin \ker(PA_1 + A_1^T P) \cap \ker(PA_2 + A_2^T P)$ by Lemma 5, but this contradicts the assumption that $\phi(t, x_0) \in \alpha_1^{-1}(0) \cap \alpha_2^{-1}(0)$ for $t \geq 0$. If $x_0 - x^* \in \text{span}\{d_1\}$, then from Lemma 5, there exists t_1 such that $x_1 := \phi(t_1, x_0)$ satisfies $x_1 - x^* \notin \text{span}\{d_1\}$. Then the trajectory $\phi(t, x_1)$ cannot stay in $\alpha_1^{-1}(0) \cap \alpha_2^{-1}(0)$ just as we have proved before. This completes the proof. ■

Remark 2. The state dimension of the Zeta converter model is four, and the set $\alpha_1^{-1}(0) \cap \alpha_2^{-1}(0)$ includes the two-dimensional affine set spanned by d_1 and d_2 in (4.20). The stability of the operating point is a consequence of Theorem 1, which is a differential-inclusion version of LaSalle's invariance principle.

4.3 Limiting the Switching Frequency

The hybrid system control proposed in Section 4.2 requires an unbounded number of switching as a solution approaches the operating point x^*. In this section, the hybrid system control strategy discussed in Section 4.2 is modified to limit the switching frequency of a Zeta converter.

4.3.1 Modified Hybrid CCM System Control Strategy

The Hybrid System Control Strategy 1 considered in Section 4.2 is based on the signs of the derivatives along the trajectories (4.8) and (4.9). Let $\rho_1, \rho_2 > 0$ and $\tilde{\alpha}_1$ and $\tilde{\alpha}_2$ be modified switching functions that satisfy the following

$$\tilde{\alpha}_1(x) \geq \alpha_1(x), \quad \tilde{\alpha}_2(x) \geq \alpha_2(x), \tag{4.26}$$

$$\alpha_2^{-1}(\mathbb{R}_{\geq 0}) \subset \tilde{\alpha}_1^{-1}\left(\mathbb{R}_{\leq \rho_1}\right), \quad \alpha_1^{-1}(\mathbb{R}_{\geq 0}) \subset \tilde{\alpha}_2^{-1}\left(\mathbb{R}_{\leq \rho_2}\right). \tag{4.27}$$

Notice that (4.27) is equivalent to

$$\tilde{\alpha}_1^{-1}\left(\mathbb{R}_{>\rho_1}\right) \subset \alpha_2^{-1}(\mathbb{R}_{<0}), \quad \tilde{\alpha}_2^{-1}\left(\mathbb{R}_{>\rho_2}\right) \subset \alpha_1^{-1}(\mathbb{R}_{<0}).$$

Based on (4.26) and (4.27), we propose the following modified hybrid system control strategy.

Hybrid CCM System Control Strategy 2

- If the system is operating at mode 1 and reaches $\tilde{\alpha}_1^{-1}(\rho_1)$, then it switches to mode 2.
- If the system is operating at mode 2 and reaches $\tilde{\alpha}_2^{-1}(\rho_2)$, then it switches to mode 1.

The differential inclusion (4.12) is modified accordingly.

$$\frac{dx}{dt} \in \tilde{F}(x), \tag{4.28}$$

$$\tilde{F}(x) \coloneqq \begin{cases} \{A_1x + B_1u_0\} & \text{if } x \in \widetilde{M}_1, \\ \{A_2x + B_2u_0\} & \text{if } x \in \widetilde{M}_2, \\ \operatorname{conv}\{A_1x + B_1u_0, A_2x + B_2u_0\} & \text{if } x \in \widetilde{M}_0, \end{cases}$$

where

$$\widetilde{M}_1 = \{x: \alpha_1^{-1}(\mathbb{R}_{<0}) \cap \tilde{\alpha}_2^{-1}(\mathbb{R}_{>\rho_2}) = \tilde{\alpha}_2^{-1}(\mathbb{R}_{>\rho_2})\},$$
$$\widetilde{M}_2 = \{x: \tilde{\alpha}_1^{-1}(\mathbb{R}_{>\rho_1}) \cap \alpha_2^{-1}(\mathbb{R}_{<0}) = \tilde{\alpha}_1^{-1}(\mathbb{R}_{>\rho_1})\},$$
$$\widetilde{M}_0 = \{x: \tilde{\alpha}_1^{-1}(\mathbb{R}_{\leq\rho_1}) \cap \tilde{\alpha}_2^{-1}(\mathbb{R}_{\leq\rho_2})\}.$$

Assumption 1. The sets $\tilde{\alpha}_1^{-1}(\mathbb{R}_{\leq\rho_1}) \cap \alpha_1^{-1}(\mathbb{R}_{>0})$ and $\tilde{\alpha}_2^{-1}(\mathbb{R}_{\leq\rho_2}) \cap \alpha_2^{-1}(\mathbb{R}_{>0})$ are bounded.

Proposition 6. Suppose Assumption 1 holds. Let $c > 0$ satisfy

$$c > \sup\left\{V(x): x \in \left(\tilde{\alpha}_1^{-1}(\mathbb{R}_{\leq\rho_1}) \cap \alpha_1^{-1}(\mathbb{R}_{>0})\right) \cup \left(\tilde{\alpha}_2^{-1}(\mathbb{R}_{\leq\rho_2}) \cap \alpha_2^{-1}(\mathbb{R}_{>0})\right)\right\}.$$

Then for any solution $\tilde{\phi}(t, x_0)$ of (4.28), there exists $T > 0$ such that $\tilde{\phi}(t, x_0) \in \{x: V(x) < c\}$ for $t > T$.

Proof. First, we shall prove that $\tilde{F}(x) \subset F(x)$ if $x \notin \Xi_\rho \coloneqq \left(\tilde{\alpha}_1^{-1}(\mathbb{R}_{\leq\rho_1}) \cap \alpha_1^{-1}(\mathbb{R}_{>0})\right) \cup \left(\tilde{\alpha}_2^{-1}(\mathbb{R}_{\leq\rho_2}) \cap \alpha_2^{-1}(\mathbb{R}_{>0})\right)$. From (4.27), $\tilde{\alpha}_1^{-1}(\mathbb{R}_{>\rho_1}) \subset \alpha_2^{-1}(\mathbb{R}_{<0})$. So, if $\tilde{\alpha}_2(x) > \rho_2$, then

$$\tilde{F}(x) = \begin{cases} \{A_1x + B_1u_0\} = F(x), & \alpha_2(x) > 0, \\ \{A_2x + B_2u_0\} \subset \operatorname{conv}\{A_1x + B_1u_0, A_2x + B_2u_0\} = F(x), & \alpha_2(x) \leq 0. \end{cases}$$

From Assumption 1, the number $c > 0$ exists. If $V(x_0) > c$, then a solution $\tilde{\phi}(t, x_0)$ of

(4.28) satisfies $\tilde{\phi}(t,x_0)=\phi(t,x_0)$ as long as $\tilde{\phi}(t,x_0)\notin\Xi_\rho$ where $\phi(t,x_0)$ is a solution of (4.12). There exists $T>0$ such that $V\big(\phi(t,x_0)\big)\geq c$ if $t>T$ because $V\big(\phi(t,x_0)\big)$ is monotonically decreasing and $V\big(\phi(t,x_0)\big)\to 0$ as $t\to\infty$ from Theorem 1. Note that $\Xi_\rho\cap\{x:V(x)\geq c\}=\emptyset$. This implies that $\tilde{\phi}(t,x_0)=\phi(t,x_0)$ and $V\left(\tilde{\phi}(t,x_0)\right)\geq c$ for $0\leq t\leq T$. Furthermore, $V\left(\tilde{\phi}(t,x_0)\right)$ is non-increasing when $\tilde{\phi}(t,x_0)\notin\Xi_\rho$. Therefore, $V\left(\tilde{\phi}(t,x_0)\right)<c$ for $t>T$. ■

4.3.2 Modified Hybrid CCM Zeta Converter Control Strategy

From (4.19),

$$\alpha_1(x)=(x-x^*)^T\begin{bmatrix}0&0&0&0\\0&0&0&0\\0&0&0&0\\0&0&0&-\frac{1}{R}\end{bmatrix}(x-x^*)+v_g(i_{L1}-i_{L1}^*)+v_g(i_{L2}-i_{L2}^*)-\frac{v_r}{R}(v_{C1}-v_{C1}^*), \tag{4.29}$$

$$\alpha_2(x)=(x-x^*)^T\begin{bmatrix}0&0&0&0\\0&0&0&0\\0&0&0&0\\0&0&0&-\frac{1}{R}\end{bmatrix}(x-x^*)-v_r(i_{L1}-i_{L1}^*)-v_r(i_{L2}-i_{L2}^*)+\frac{v_r^2}{Rv_g}(v_{C1}-v_{C1}^*). \tag{4.30}$$

Define

$$d_3\coloneqq\begin{bmatrix}\frac{v_gRC_1}{L_1}\\\frac{v_gRC_1}{L_2}\\-v_r\\0\end{bmatrix},\quad d_4\coloneqq\begin{bmatrix}0\\0\\0\\v_r\end{bmatrix}. \tag{4.31}$$

Then $\{d_1,d_2,d_3,d_4\}$ with d_1 and d_2 in (4.20) is a basis of $\mathbb{R}^4$, and thus any $x\in\mathbb{R}^4$ can be written as

$$x-x^*=\Delta x=\delta_1d_1+\delta_2d_2+\delta_3d_3+\delta_4d_4. \tag{4.32}$$

The modified functions $\tilde{\alpha}_1(x)$ and $\tilde{\alpha}_2(x)$ can be defined as

$$\tilde{\alpha}_1(x)\coloneqq\alpha_1(x)+k_1\delta_4^2+\beta(c_1\|\delta_1,\delta_2\|), \tag{4.33}$$

$$\tilde{\alpha}_2(x)\coloneqq\alpha_2(x)+k_2\delta_4^2+\beta(c_2\|\delta_1,\delta_2\|), \tag{4.34}$$

where $\|\delta_1, \delta_2\|$ is any norm in $\mathbb{R}^2$, and $\beta: \mathbb{R}_{\geq 0} \to \mathbb{R}_{\geq 0}$ is a monotone nondecreasing function satisfying

$$\beta(0) = 0, \quad \beta(z) = \rho, \quad \text{if } z \geq \rho,$$
$$0 < k_1 < \frac{v_r^2}{R},\ 0 < k_2 < \frac{v_r^2}{R},\ c_1 > 0,\ c_2 > 0,\ \rho > 0.$$

Proposition 7. The functions $\tilde{\alpha}_1$ and $\tilde{\alpha}_2$ defined by (4.33) and (4.34) satisfy (4.26), (4.27), and Assumption 1.

Proof. It is obvious that (4.26) holds. Suppose $\alpha_2(x) \geq 0$. Define $p_1(x - x^*) \coloneqq \alpha_1(x) + k_1\delta_4^2$ and $p_2(x - x^*) \coloneqq \alpha_2(x) + k_2\delta_4^2$. Then the quadratic terms of p_1 and p_2 are nonpositive, and hence by Lemma 1, we assert that $\alpha_1(x) + k_1\delta_4^2 \leq 0$. Because $\beta(c_1\|\delta_1, \delta_2\|) \leq \rho_1$, we obtain $\tilde{\alpha}_1(x) \leq \rho_1$. Similarly, $\alpha_1(x) \geq 0$ implies $\tilde{\alpha}_2(x) \leq \rho_2$. To show that $\alpha_1^{-1}(\mathbb{R}_{>0}) \cap \tilde{\alpha}_1^{-1}\left(\mathbb{R}_{\leq \rho_1}\right)$ is bounded, we use the representation (4.30) and show that the set $\left\{(d_1, d_2, d_3, d_4): x \in \alpha_1^{-1}(\mathbb{R}_{>0}) \cap \tilde{\alpha}_1^{-1}\left(\mathbb{R}_{\leq \rho_1}\right)\right\}$ is bounded. If $\alpha_1(x) > 0$ and $\tilde{\alpha}_1(x) \leq \rho_1$, then

$$\rho_1 > \tilde{\alpha}_1(x) - \alpha_1(x) = k_1\delta_4^2 + \beta(c_1\|\delta_1, \delta_2\|) \geq \begin{cases} \beta(c_1\|\delta_1, \delta_2\|), \\ k_1\delta_4^2. \end{cases} \tag{4.35}$$

From (4.35), it follows that $\|\delta_1, \delta_2\| < \frac{\rho_1}{c_1}$ and $|\delta_4| < \sqrt{\frac{\rho_1}{k_1}}$. From the definition of α_1, $\tilde{\alpha}_1$, and d_3, we have

$$\alpha_1(x) = k\delta_3 + \gamma(\delta_1, \delta_2, \delta_4), \quad \tilde{\alpha}_1(x) = k\delta_3 + \tilde{\gamma}(\delta_1, \delta_2, \delta_4),$$

where γ and $\tilde{\gamma}$ are continuous functions and

$$k = \frac{v_r^2 RC_1}{L_1} + \frac{v_r^2 RC_1}{L_2} + \frac{v_r^2}{R} > 0.$$

Let

$$M \coloneqq \sup\left\{\gamma(\delta_1, \delta_2, \delta_4): \|\delta_1, \delta_2\| < \frac{\rho_1}{c_1}, |\delta_4| < \sqrt{\frac{\rho_1}{k_1}}\right\},$$
$$m \coloneqq \inf\left\{\tilde{\gamma}(\delta_1, \delta_2, \delta_4): \|\delta_1, \delta_2\| < \frac{\rho_1}{c_1}, |\delta_4| < \sqrt{\frac{\rho_1}{k_1}}\right\}.$$

Then,

$$0 < \alpha_1(x) = k\delta_3 + \gamma(\delta_1, \delta_2, \delta_4) \leq k\delta_3 + M,$$
$$\rho_1 \geq \tilde{\alpha}_1(x) = k\delta_3 + \tilde{\gamma}(\delta_1, \delta_2, \delta_4) \geq k\delta_3 + m,$$

and it follows that $-\frac{M}{k} < \delta_3 \leq \frac{\rho_1 - m}{k}$. The boundedness of the set $\alpha_2^{-1}(\mathbb{R}_{>0}) \cap \tilde{\alpha}_2^{-1}(\mathbb{R}_{\leq \rho_2})$ can be proved similarly. ■

4.3.3 Switching Frequency Estimation in CCM Operation

Although the modified hybrid system control strategy can limit the switching frequency, the value of the switching frequency itself, however, is controlled by the parameters in Hybrid CCM System Control Strategy 2. In this subsection, we will show how to decide such parameters based on a linear-line approximation of the trajectory.

From Section 4.4.2, the switching occurs when

$$\rho_1 \coloneqq \tilde{\alpha}_1(x^* + \Delta x_1),$$
$$\rho_2 \coloneqq \tilde{\alpha}_2(x^* + \Delta x_2),$$

where $\Delta x_1 \coloneqq \begin{bmatrix}\Delta i_{L1,1} & \Delta i_{L2,1} & \Delta v_{C1,1} & 0\end{bmatrix}^T$ and $\Delta x_2 \coloneqq \begin{bmatrix}\Delta i_{L1,2} & \Delta i_{L2,2} & \Delta v_{C1,2} & 0\end{bmatrix}^T$ are the difference of the approximated state-trajectory from the operating point at their respective switching instants as shown in Figure 4.1.

Observing Figure 4.1 and from (4.21) and (4.22), the gradient of the state-trajectory at the operating point is given by

$$\frac{2\Delta x_1}{\lambda T_{sw}} = \begin{bmatrix} \frac{v_g}{L_1} \\ \frac{v_g}{L_2} \\ -\frac{v_r}{C_1 R} \\ 0 \end{bmatrix}, \quad \frac{2\Delta x_2}{(1-\lambda)T_{sw}} = \begin{bmatrix} -\frac{v_r}{L_1} \\ -\frac{v_r}{L_2} \\ \frac{v_r^2}{C_1 R v_g} \\ 0 \end{bmatrix}.$$

where $T_{sw} = \frac{1}{f}$ is the period of the switching frequency f. With $\lambda = \frac{v_r}{v_r + v_g}$ (from (4.17)) the above expressions can be rewritten as

$$\Delta x_1 = \begin{bmatrix} \frac{v_r v_g}{2fL_1(v_r+v_g)} \\ \frac{v_r v_g}{2fL_2(v_r+v_g)} \\ -\frac{v_r^2}{2fC_1R(v_r+v_g)} \\ 0 \end{bmatrix}, \quad \Delta x_2 = \begin{bmatrix} -\frac{v_r v_g}{2fL_1(v_r+v_g)} \\ -\frac{v_r v_g}{2fL_2(v_r+v_g)} \\ \frac{v_r^2}{2fC_1R(v_r+v_g)} \\ 0 \end{bmatrix}. \tag{4.36}$$

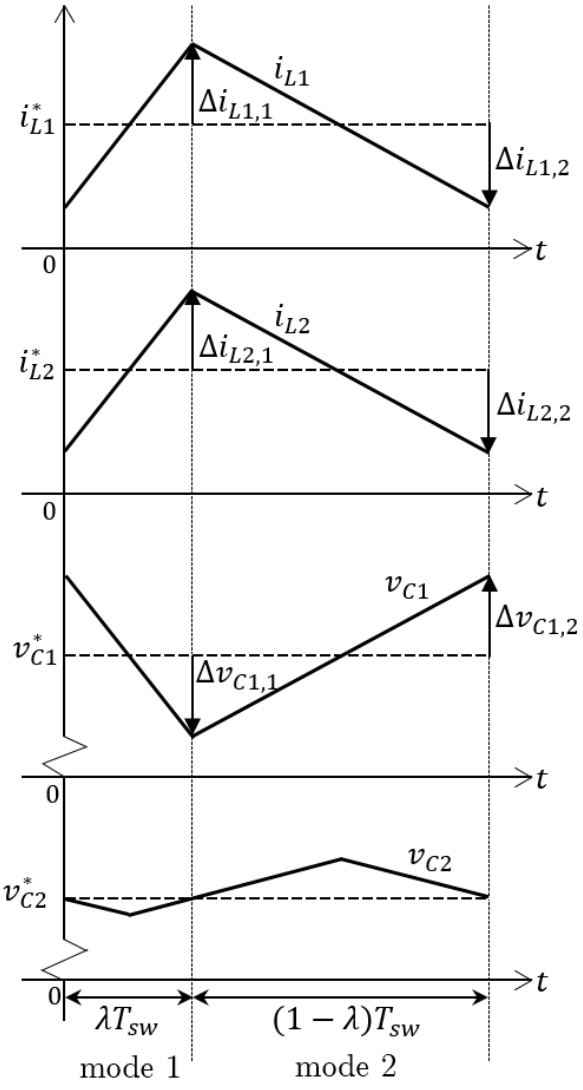

Figure 4.1: Approximate state-trajectory at the operating point for a DC-DC Zeta converter in CCM operation.

Define penalty functions $\sigma_1 := k_1\delta_4^2 + \beta(c_1\|\delta_1, \delta_2\|)$ and $\sigma_2 := k_2\delta_4^2 + \beta(c_2\|\delta_1, \delta_2\|)$ and assume the state-trajectory near the operating point. Therefore, the penalty functions are close to 0 such that $\sigma_1 \approx 0$ and $\sigma_2 \approx 0$, consequently, $\rho_1 \approx \alpha_1(x^* + \Delta x_1)$ and $\rho_2 \approx$

$\alpha_2(x^* + \Delta x_2)$. Nevertheless, the effect of $\sigma_1 > 0$ and $\sigma_2 > 0$ will be investigated and illustrated graphically later in Section 4.5. Therefore, with (4.17) and (4.36), and from (4.29) and (4.30), we have

$$\rho_1 \approx \frac{v_r(L_1L_2v_r^2+C_1L_1R^2v_g^2+C_1L_2R^2v_g^2)}{2fC_1L_1L_2R^2(v_r+v_g)}, \tag{4.37}$$

$$\rho_2 \approx \frac{v_r^2(L_1L_2v_r^2+C_1L_1R^2v_g^2+C_1L_2R^2v_g^2)}{2fC_1L_1L_2R^2v_g(v_r+v_g)}. \tag{4.38}$$

From (4.37) and (4.38), we observe how the desired switching frequency f is related to the thresholds ρ_1 and ρ_2. As such, the DC-DC Zeta converter will operate at the prescribed switching frequency under the modified hybrid system control strategy. Though the expressions of ρ_1 and ρ_2 look complex, some of the parameters are pre-processed beforehand (offline). Nowadays, considering the capability of the high-speed processors like in the DSP, FPGA, or even microcontroller, there should be no performance issue in executing the hybrid system control strategy.

4.4 Simulation Results

In this section, the proposed hybrid DC-DC Zeta converter control strategy is simulated using a circuit-based simulator called PSIM, as depicted in Figure 4.2. Considering a solar battery charging application for a smartphone, the output of a photovoltaic (PV) panel, which act as the input voltage v_g of the converter, is assumed to be $18\,\mathrm{V}$ and the converter output voltage v_o $5\,\mathrm{V}$ is considered to charge the smartphone. The parameters for the Zeta converter are considered ideal (zero internal resistance) as tabulated in Table 4.1. All four state variables i_{L1}, i_{L2}, v_{C1}, and v_{C2}, the input voltage v_g, and the load current i_o are assumed to be measurable. Note that the load R is sensed using v_{C2} and i_o measurements such that $R = \frac{v_{C2}}{i_o}$. With parameters in Table 4.1 and using fixed number to reduce the computational burden, then $\tilde{\alpha}_1$, $\tilde{\alpha}_2$, ρ_1 and ρ_2 in (4.33), (4.34), (4.37) and (4.38), can respectively be rewritten as

$$\tilde{\alpha}_1(x) = v_g(i_{L1} + i_{L2}) - i_o\left(\frac{5}{v_{C2}}\left(v_{C1} + v_g + 5\right) + v_{C2} - 10\right) + \sigma_1, \tag{4.39}$$

$$\tilde{\alpha}_2(x) = -5(i_{L1} + i_{L2}) + i_o\left(\frac{25v_{C1}}{v_{C2}v_g} - v_{C2} + 10\right) + \sigma_2, \tag{4.40}$$

$$\rho_1 \approx \frac{1}{4(v_g+5)}\left(2v_g^2 + 25\left(\frac{i_o}{v_{C2}}\right)^2\right), \tag{4.41}$$

$$\rho_2 \approx \frac{5}{4v_g(v_g+5)}\left(2v_g^2 + 25\left(\frac{i_o}{v_{C2}}\right)^2\right), \tag{4.42}$$

Table 4.1: The DC-DC Zeta converter parameters in CCM operation.

Parameter	**Value**
v_g	18 V
$v_o(v_r)$	5 V
R	2.5 Ω
L_1	100 μH
L_2	100 μH
C_1	100 μF
C_2	220 μF
f	100 kHz

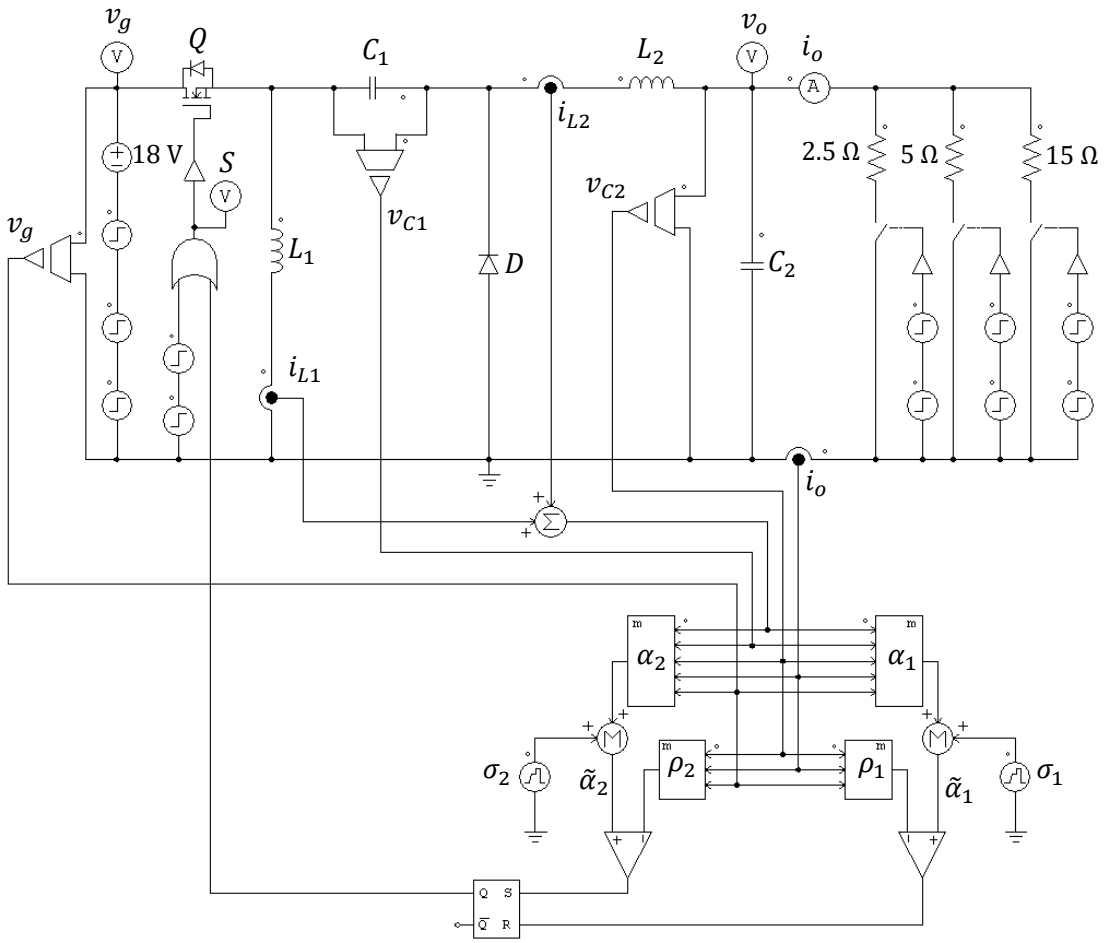

Figure 4.2: Simulation circuit of a DC-DC Zeta converter hybrid control in CCM operation.

In Figure 4.3 and Figure 4.4, the simulation results for $\sigma_1 \approx 0$ and $\sigma_2 \approx 0$ are shown. The waveforms of Figure 4.3(a), Figure 4.3(b), Figure 4.3(c), and Figure 4.3(d) show the output voltage v_o, the load current i_o, the input voltage v_g, and the switching S signals, respectively. In practice, the voltage generated by the PV panel fluctuates, however, since a small time interval (a few milliseconds) is used in the simulation, a step input voltage is considered. For nominal input voltage $18\,\text{V}$ and load $2.5\,\Omega$ (implies $i_o = 2\,\text{A}$), no overshoot at the output voltage and load current are observed during start-up, and the settling time is approximately $10\ \text{ms}$. At $t = 20\,\text{ms}$, the input voltage is reduced by $-50\,\%$ to $9\,\text{V}$ while the load is increased by $+50\,\%$ to $5\,\Omega$ ($i_o = 1\,\text{A}$), respectively. Despite the considerably large perturbations, the hybrid system control produced no output voltage overshoot, albeit some oscillations, and settles at $t \approx 30\,\text{ms}$. Afterwards, at $t = 40\,\text{ms}$, $v_g = 4.5\,\text{V}$ and $R = 15\,\Omega$ ($i_o = 0.33\,\text{A}$), a variations of $-50\,\%$ and $+200\,\%$, respectively. Compared to previously, the output voltage oscillates more, nonetheless eventually it returned to its operating point, though with a longer settling time. It is worth highlighting that the converter is now operating in step-up mode (instead of step-down mode for the first two perturbations), this proves the effectiveness of the switching control in regulating the output voltage at both operation modes. Finally, at $t = 80\,\text{ms}$, the input voltage and the load is returned to their nominal value $18\,\text{V}$ ($+300\,\%$) and $2.5\,\Omega$ ($-83.33\,\%$), respectively. Albeit significant perturbations, the hybrid system control works perfectly with minimum output voltage oscillation and considerably fast settling time ($\approx 8\,\text{ms}$). The close view of the switching waveform under three input voltages and loads perturbations discussed above is illustrated in Figure 4.4. As can be observed, the hybrid system control produced switching frequencies $99.42\,\text{kHz}$ (see Figure 4.4(a)), $99.79\,\text{kHz}$ (Figure 4.4(b)), and $98.77\,\text{kHz}$ (Figure 4.4(c)), which is close to the desired $100\,\text{kHz}$ switching frequency, thus validates its usefulness.

In the next simulation, the effect of introducing the penalty functions $\sigma_1 > 0$ and $\sigma_2 > 0$, will be discussed. For this simulation, nominal input voltage $18\,\text{V}$ and load $2.5\,\Omega$ are used. As can be observed in Figure 4.5, the introduction of σ_1 and σ_2 does not have much effect on the response of the output voltage (see Figure 4.5(a)). Increasing σ_1 and σ_2, however, increases the switching frequency, as shown in Figure 4.6. Precisely, for $\sigma_1 = 3.84$ and $\sigma_2 = 1.07$, the switching frequency is $203.67\,\text{kHz}$, and it increases further to $454.55\,\text{kHz}$ for a larger penalty function $\sigma_1 = 5.72$ and $\sigma_2 = 1.59$. These observations are expected: (4.37) and (4.38) are no longer valid, since σ_1 and σ_2 are not approximately zero. As σ_1 and σ_2 reaches thresholds $\rho_1 = 7.087$ and $\rho_2 = 1.969$, respectively, the number of switching becomes unbounded, which is identical to the case of Hybrid CCM System Control Strategy 1 in Section 4.2.

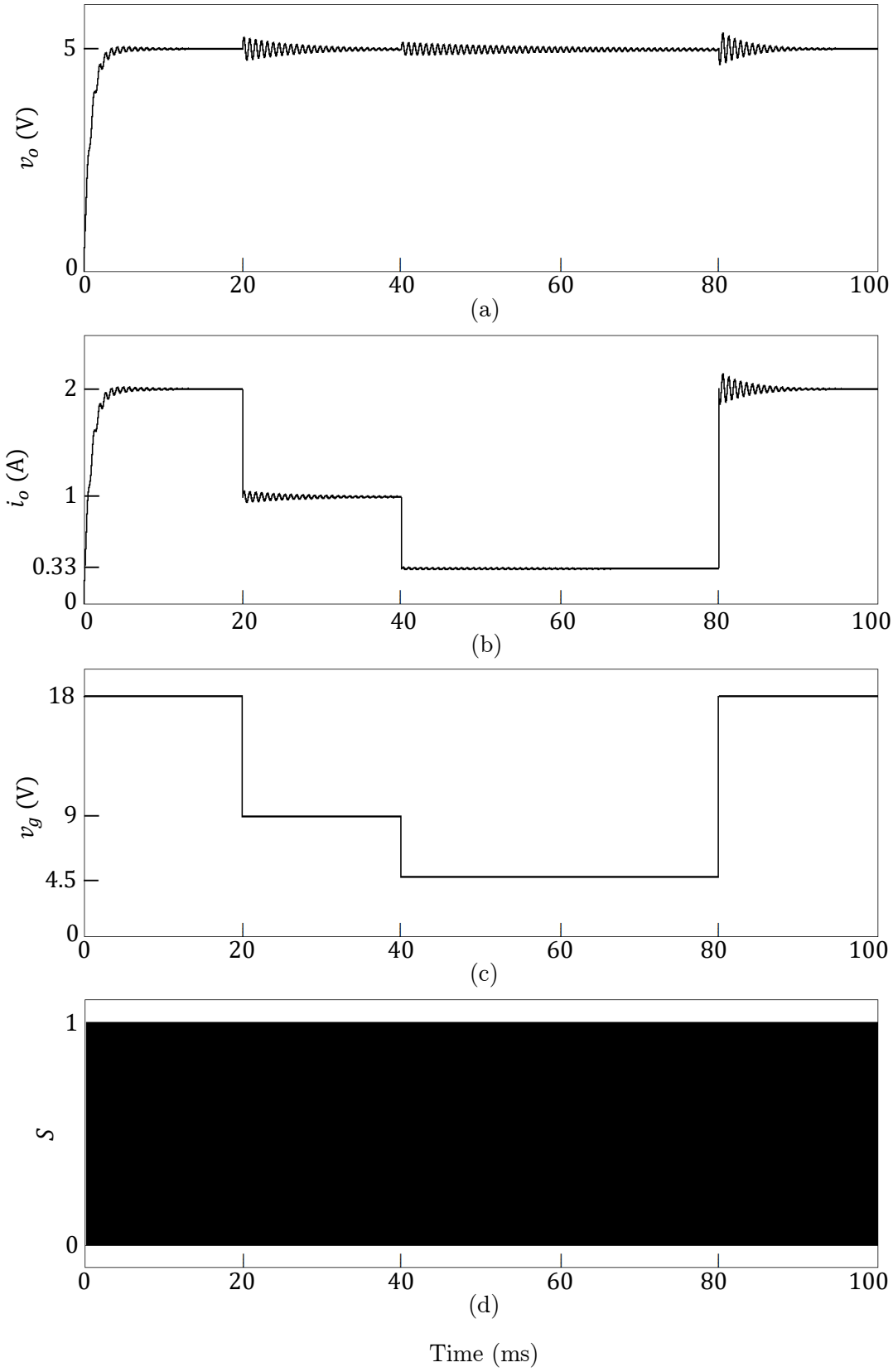

Figure 4.3: Simulated response in CCM operation under input voltage v_g and load R perturbations for $\sigma_1 \approx 0$ and $\sigma_2 \approx 0$. Variations in (a) output voltage v_o, (b) load current i_o, (c) input voltage v_g, and (d) switching S.

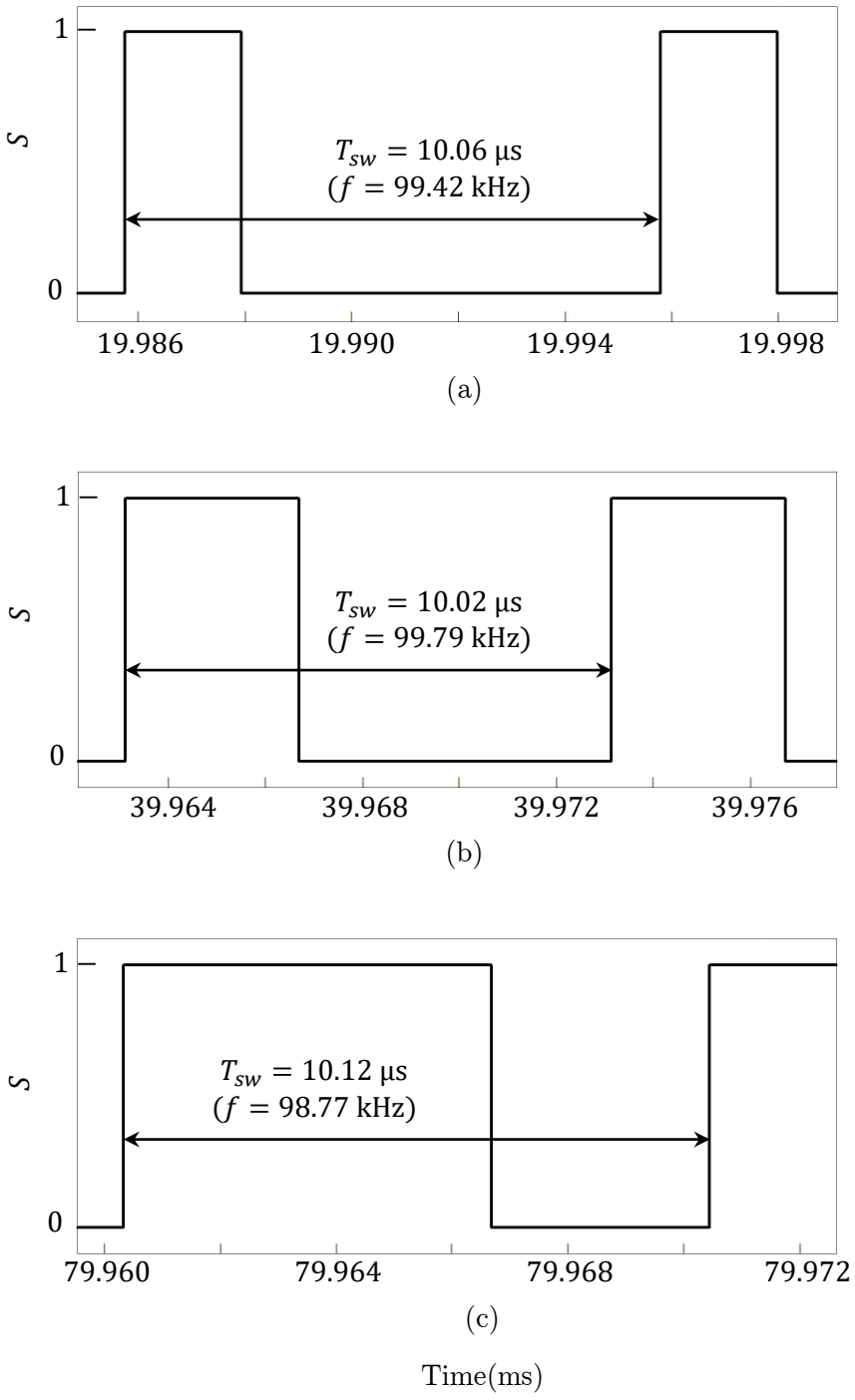

Figure 4.4: Close view of switching S for $\sigma_1 \approx 0$ and $\sigma_2 \approx 0$ at the operating point in CCM operation under (a) $v_g = 18\,\text{V}$ and $R = 2.5\,\Omega$, (b) $v_g = 9\,\text{V}$ and $R = 5\,\Omega$, and (c) $v_g = 3\,\text{V}$ and $R = 15\,\Omega$.

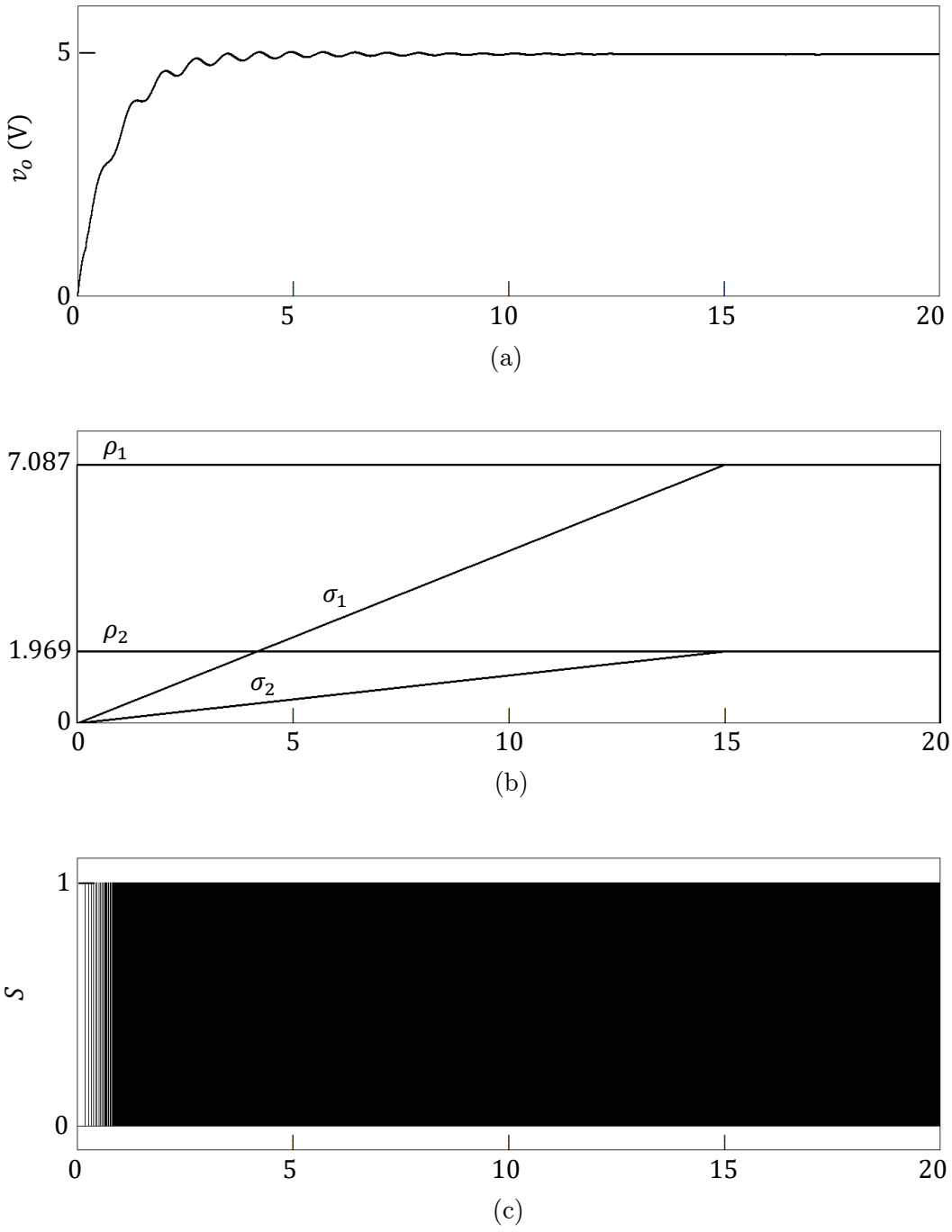

Figure 4.5: Simulated response for $\sigma_1 > 0$ and $\sigma_2 > 0$. Variations in (a) output voltage v_o, (b) penalty functions σ_1 and σ_2, and (c) switching S.

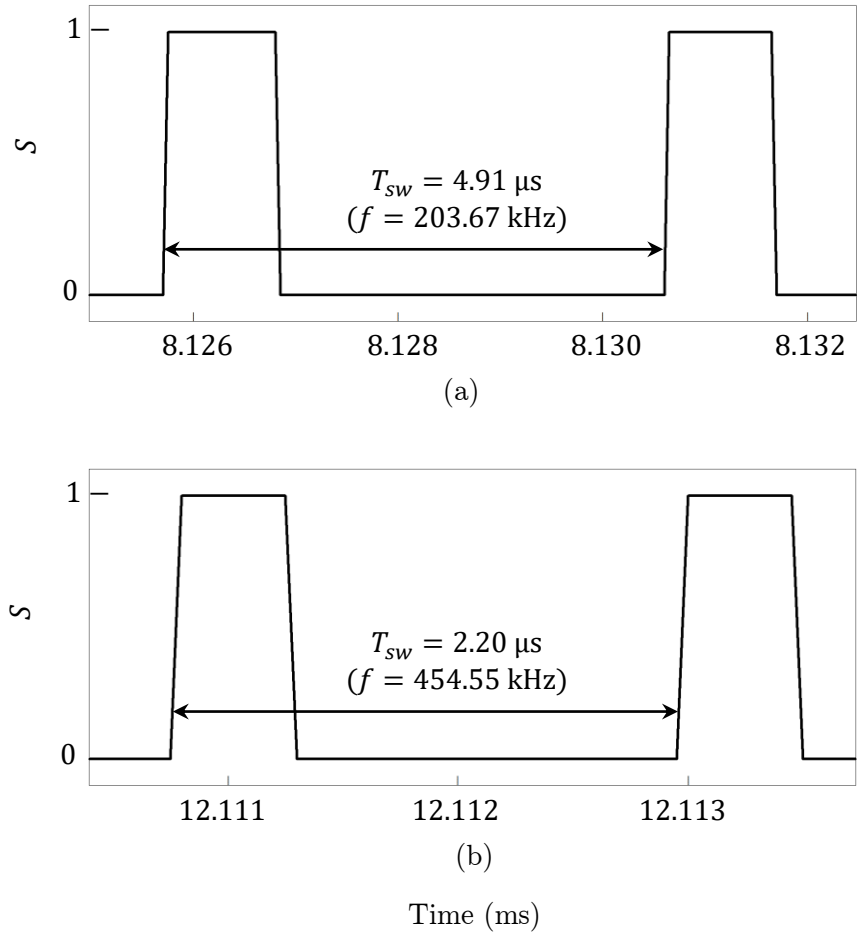

Figure 4.6: Close view of switching S under $v_g = 18\,\text{V}$ and $R = 2.5\,\Omega$, for (a) $\sigma_1 = 3.84$, $\sigma_2 = 1.07$, and (b) $\sigma_1 = 5.72$, $\sigma_2 = 1.59$.

4.5 Summary

In this chapter, a hybrid system control strategy for the stabilization of a DC-DC Zeta converter operating in continuous conduction mode (CCM) is proposed. The hybrid system control strategy is based on a Lyapunov functional candidate for a four-dimensional Zeta converter model. The local asymptotical stability of the operating point is established using LaSalle's invariance principle for differential inclusion. By applying spatial regularization, a modified hybrid system control strategy reduces the switching frequency and keeps the state-trajectory around a neighborhood of the operating point. Furthermore, by approximating the state-trajectory near the operating point, an explicit relation between the modified hybrid system control strategy and the switching frequency is obtained, which allows one to choose systematically the desired switching frequency for the converter to operate. The method works well even if the operation point changes significantly and it is valid for both step-up and step-down operations.

Chapter 5

Hybrid DC-DC Zeta Converter Control Operating in DCM

5.1 Hybrid Three-mode System Control

In this section, we propose a hybrid system control strategy based on a control Lyapunov function (CLF) candidate for a three-mode system, which is a model for DC-DC Zeta converter operating under discontinuous conduction mode (DCM).

Consider the state vector $x = [i_{L1}\ i_{L2}\ v_{C1}\ v_{C2}]^T$ and the input $u = v_g$. Then, the state-space equations of a Zeta converter in DCM operation, as derived in Section 2.3, for mode 1, mode 2, and mode 3 are represented respectively by

$$\frac{dx}{dt} = A_1 x + B_1 u, \tag{5.1}$$

$$\frac{dx}{dt} = A_2 x + B_2 u, \tag{5.2}$$

$$\frac{dx}{dt} = A_3 x + B_3 u, \tag{5.3}$$

where

$$A_1 = \begin{bmatrix} 0 & 0 & 0 & 0 \\ 0 & 0 & \frac{1}{L_2} & -\frac{1}{L_2} \\ 0 & -\frac{1}{C_1} & 0 & 0 \\ 0 & \frac{1}{C_2} & 0 & -\frac{1}{RC_2} \end{bmatrix}, \quad B_1 = \begin{bmatrix} \frac{1}{L_1} \\ \frac{1}{L_2} \\ 0 \\ 0 \end{bmatrix}, \tag{5.4}$$

$$A_2 = \begin{bmatrix} 0 & 0 & -\frac{1}{L_1} & 0 \\ 0 & 0 & 0 & -\frac{1}{L_2} \\ \frac{1}{C_1} & 0 & 0 & 0 \\ 0 & \frac{1}{C_2} & 0 & -\frac{1}{RC_2} \end{bmatrix}, \quad B_2 = \begin{bmatrix} 0 \\ 0 \\ 0 \\ 0 \end{bmatrix}, \tag{5.5}$$

$$A_3 = \begin{bmatrix} 0 & 0 & -\frac{1}{L_1+L_2} & \frac{1}{L_1+L_2} \\ 0 & 0 & \frac{1}{L_1+L_2} & -\frac{1}{L_1+L_2} \\ \frac{1}{C_1} & 0 & 0 & 0 \\ 0 & \frac{1}{C_2} & 0 & -\frac{1}{RC_2} \end{bmatrix}, \quad B_3 = \begin{bmatrix} 0 \\ 0 \\ 0 \\ 0 \end{bmatrix}. \tag{5.6}$$

Note that under mode 3, $i_{L1} + i_{L2} = 0$ and $i_{L2} > 0$ hold, which means that the currents of the inductors are not independent. Therefore, the state of mode 3 is restricted in a three-dimensional subspace.

Consider the operating point x^* of the DC-DC Zeta converter under DCM operation given by

$$x^* = \begin{bmatrix} i_{L1}^* \\ i_{L2}^* \\ v_{C1}^* \\ v_{C2}^* \end{bmatrix} = \begin{bmatrix} \frac{v_{ref}^2}{Rv_g} \\ \frac{v_{ref}}{R} \\ v_{ref} \\ v_{ref} \end{bmatrix}. \tag{5.7}$$

The control aims to produce an output voltage v_o that follows a reference voltage v_{ref}. For that, based on the sum of energies available in a Zeta converter, a CLF candidate is chosen as following

$$V(x) = (x - x^*)^T P (x - x^*),$$
$$P := \begin{bmatrix} \frac{L_1}{2} & 0 & 0 & 0 \\ 0 & \frac{L_2}{2} & 0 & 0 \\ 0 & 0 & \frac{C_1}{2} & 0 \\ 0 & 0 & 0 & \frac{C_2}{2} \end{bmatrix}. \tag{5.8}$$

Under mode 1, mode 2, and mode 3 of the Zeta converter in DCM operation, let the respective derivative of $V(x)$ along the trajectory denoted by $\alpha_1(x)$, $\alpha_2(x)$ and $\alpha_3(x)$ be defined by

$$\alpha_1(x) \coloneqq \left(A_1x + B_1v_g\right)^T P(x - x^*) + (x - x^*)^T P\left(A_1x + B_1v_g\right)$$
$$= -\frac{1}{R}(v_{C2}^* - v_{C2})^2 + v_g(i_{L1} - i_{L1}^*) + v_g(i_{L2} - i_{L2}^*) - \frac{v_{ref}}{R}(v_{C1} - v_{C1}^*), \quad (5.9)$$

$$\alpha_2(x) \coloneqq \left(A_2x + B_2v_g\right)^T P(x - x^*) + (x - x^*)^T P\left(A_2x + B_2v_g\right)$$
$$= -\frac{1}{R}(v_{C2}^* - v_{C2})^2 - v_{ref}(i_{L1} - i_{L1}^*) - v_{ref}(i_{L2} - i_{L2}^*) + \frac{v_{ref}^2}{Rv_g}(v_{C1} - v_{C1}^*), \quad (5.10)$$

$$\alpha_3(x) \coloneqq \left(A_3x + B_3v_g\right)^T P(x - x^*) + (x - x^*)^T P\left(A_3x + B_3v_g\right)$$
$$= -\frac{1}{R}(v_{C2}^* - v_{C2})^2 + (i_{L2} - i_{L2}^*)(v_{C2} - v_{C2}^*) + \frac{v_{ref}^2}{Rv_g}(v_{C1} - v_{C1}^*). \quad (5.11)$$

Subsequently, a switching control mechanism for the stabilization of the converter which is based on CLF (5.8), is proposed as following.

Hybrid DCM System Control Strategy 1

- If the system is operating in mode 1 and reaches $\alpha_1^{-1}(0)$, then it switches to mode 2.
- If the system is operating in mode 2 and reaches $\alpha_2^{-1}(0)$, then it switches to mode 1.
- If the system is operating in mode 3 and reaches $\alpha_3^{-1}(0)$, then it switches to mode 1.

5.2 Stability of Zeta Converter in DCM

In this section, we analyze the stability of the Hybrid DCM System Control Strategy 1 defined in Section 5.1. It is important to highlight that the switching control mechanism for the DCM operation follows the similar line with the one in the CCM operation, except that for the later, the third mode does not exist, and the transitions from mode 2 to mode 3, and from mode 3 to mode 1, are not defined. Nevertheless, the local stability of the DCM operation is derived from that of the CCM operation.

Theorem 1. The operating point x^* is locally asymptotic stable under the Hybrid DCM System Control Strategy 1.

Proof. Let $\gamma_1 = \min V(x)$ subject to $i_{L1} + i_{L2} = 0$. Then the minimum is achieved by

$$x^{\dagger} = \begin{bmatrix} \frac{L_1 i_{L1}^* - L_2 i_{L2}^*}{L_1 + L_2} \\ \frac{-L_1 i_{L1}^* + L_2 i_{L2}^*}{L_1 + L_2} \\ v_{C1}^* \\ v_{C2}^* \end{bmatrix}, \tag{5.12}$$

and the optimal value is

$$\gamma_1 = V(x^{\dagger}) = \frac{L_1 L_2 v_{ref}^2 (v_{ref} + v_g)^2}{2(L_1 + L_2) R^2 v_g^2}. \tag{5.13}$$

The set $\{x: V(x) < \gamma_1\}$ is invariant under the Hybrid DCM System Control Strategy 1 and does not contain mode 3. From Theorem 1 of CCM operation in Section 4.2.1 which uses LaSalle's invariance principle for hybrid systems, the locally asymptotical stability of the operation point follows. ■

Remark 1. Under the Hybrid DCM System Control Strategy 1, mode 3 does not emerge if a trajectory starts within the invariant set $\{x: V(x) < \gamma_1\}$.

Remark 2. The proof of Theorem 1 does not say that $x^{\dagger}$ is reachable in a standard operation. Instead, it merely says that once the value of the Lyapunov function $V(x)$ becomes smaller than γ_1, then mode 3 will never emerge.

5.3 Modified Hybrid DCM Zeta Converter Control Strategy

Under the Hybrid DCM System Control Strategy 1, the DCM operation is not guaranteed. In fact, as the state-trajectory approaches the operating point, the switching becomes arbitrarily fast such that mode 3 is lost, thus the DCM operation cannot be achieved. To maintain the DCM operation, the hybrid system control strategy needs to be modified, which is discussed in this section.

To reduce the switching frequency, the switching timing needs to be relaxed and the distance from the operating point needs to be penalized. For that, let $\rho_1,\ \rho_2,\ \rho_3 > 0$ which satisfy

$$\alpha_1^{-1}(\mathbb{R}_{>\rho_1}) \subset \alpha_2^{-1}(\mathbb{R}_{<0}),\ \ \alpha_2^{-1}(\mathbb{R}_{>\rho_2}) \subset \alpha_3^{-1}(\mathbb{R}_{<0}),\ \ \alpha_3^{-1}(\mathbb{R}_{>\rho_3}) \subset \alpha_1^{-1}(\mathbb{R}_{<0}). \tag{5.14}$$

Based on (5.14), we propose the following modified switching control mechanism.

Hybrid DCM System Control Strategy 2

- If the system is operating in mode 1 and reaches $\alpha_1^{-1}(\rho_1)$, then it switches to mode 2.
- If the system is operating in mode 2 and reaches $i_{L1} + i_{L2} = 0$, then it switches to mode 3.
- If the system is operating in mode 3 and reaches $\alpha_3^{-1}(\rho_3)$, then it switches to mode 1.

Remark 3. Under mode 3, $i_{L1} + i_{L2} = 0$ holds. Hence, $i_{L1} + i_{L2} = 0$ is defined in the switching mechanism instead of $\alpha_2^{-1}(\rho_2)$. Nonetheless, the transition from mode 2 to mode 3 is due to endogenous switching, thus neither of the two conditions contribute to the external switching. Therefore, in the next section, finding ρ_2 will be omitted

5.4 Switching Frequency Estimation in DCM Operation

To estimate the switching frequency, as shown in Figure 5.1, the state-trajectory is assumed to have the following properties.

- It is close (near) to the operating point.
- It moves in a piecewise linear line.
- It evolves periodically.

Define

$$\rho_1 \coloneqq \alpha_1(x^* + \Delta x_1), \tag{5.15}$$

$$\rho_3 \coloneqq \alpha_3(x^* + \Delta x_3), \tag{5.16}$$

where $\Delta x_1 \coloneqq \left[\Delta i_{L1,1}\ \Delta i_{L2,1}\ \Delta v_{C1,1}\ 0\right]^T$ and $\Delta x_3 \coloneqq \left[\Delta i_{L1,3}\ \Delta i_{L2,3}\ \Delta v_{C1,3}\ 0\right]^T$ are the difference of the approximated state-trajectory from the operating point at switching instants for mode 1 and mode 3, respectively, as depicted in Figure 5.1.

Substituting (5.7) and from (5.9) and (5.11), ρ_1 and ρ_2 in (5.15) and (5.16), respectively, can be rewritten as follows:

$$\rho_1 = v_g\left(\Delta i_{L1,1} + \Delta i_{L2,1}\right) - \frac{v_{ref}}{R}\Delta v_{C1,1}, \tag{5.17}$$

$$\rho_3 = \frac{v_{ref}^2}{R v_g}\Delta v_{C1,3}. \tag{5.18}$$

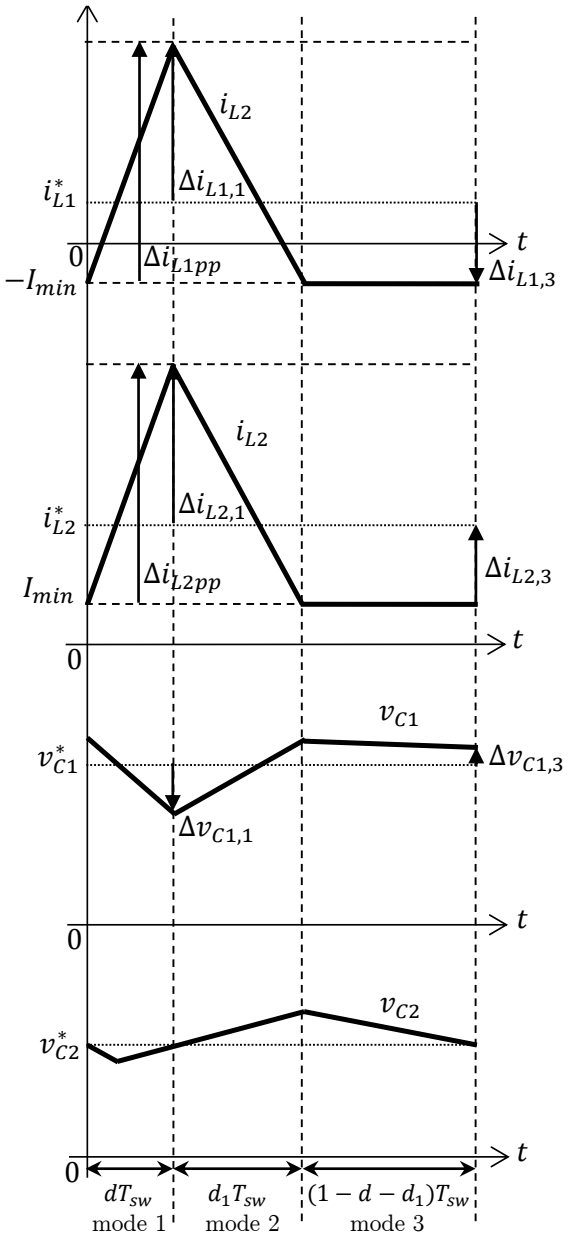

Figure 5.1: Approximate state-trajectory at the operating point
for a DC-DC Zeta converter in DCM operation.

For the following analysis, the dynamics in (5.4) and (5.5), and Figure 5.1 are referred.

$$\begin{aligned}\Delta i_{L1,1} &= \Delta i_{L1pp} - i_{L1}^* - I_{min} \\ &= \frac{dv_g}{fL_1} - \frac{v_{ref}^2}{Rv_g} - I_{min}.\end{aligned} \tag{5.19}$$

$$\begin{aligned}\Delta i_{L2,1} &= \Delta i_{L2pp} - i_{L2}^* + I_{min} \\ &= \frac{dv_g}{fL_2} - \frac{v_{ref}}{R} + I_{min}.\end{aligned} \tag{5.20}$$

$$\Delta v_{C1,1} = -\frac{1}{2C_1}\Delta i_{L2,1}\left(\frac{L_1}{v_g}\Delta i_{L2,1}\right)$$
$$= \frac{L_1}{2C_1 v_g}\left(\frac{dv_g}{fL_2} - \frac{v_{ref}}{R} + I_{min}\right)^2. \quad (5.21)$$

$$\Delta v_{C1,3} = \frac{1}{2C_1}(i_{L2}^* - I_{min})\left(\frac{L_2}{v_g}(i_{L2}^* - I_{min})\right)$$
$$= \frac{L_2}{2C_1 v_g}\left(\frac{v_{ref}}{R} - I_{min}\right)^2. \quad (5.22)$$

From above, $f = \frac{1}{T_{sw}}$ is the switching frequency and d is the duty ratio.

Under mode 3, $I_{min} = i_{L2min}$ (see Figure 5.1) and the minimum is also achieved by $x^\dagger$ (5.12). Comparing i_{L2min} with the second row of $x^\dagger$, one finds

$$I_{min} = \frac{-L_1 i_{L1}^* + L_2 i_{L2}^*}{L_1 + L_2} = \frac{L_2 v_g v_{ref} - L_1 v_{ref}^2}{R v_g (L_1 + L_2)}. \quad (5.23)$$

To find d, Δi_{L1pp} in mode 1 and mode 2 is observed and is given by

$$\Delta i_{Lpp} = \frac{dv_g}{fL_1} = \frac{d_1 v_{ref}}{fL_1}. \quad (5.24)$$

Then, solving for d in (5.24), one gets the following

$$d = \frac{v_{ref}}{v_g} d_1, \quad (5.25)$$

where d_1 is the duty ratio of mode 2.

On the other hand, the average inductor currents of i_{L1}^* and i_{L2}^* can be expressed by

$$i_{L1}^* = \frac{dv_g(d+d_1)}{2L_1 f} - I_{min}, \quad (5.26)$$
$$i_{L2}^* = \frac{dv_g(d+d_1)}{2L_2 f} + I_{min}. \quad (5.27)$$

With (5.25), by summing (5.26) and (5.27) and solving for d_1, one yield

$$d_1 = \sqrt{\frac{2L_1 L_2 f}{(L_1 + L_2)R}}. \quad (5.28)$$

By substituting (5.23), (5.25), and (5.28) into (5.19), (5.20), (5.21) and (5.22), respectively, $\Delta i_{L1,1}$, $\Delta i_{L2,1}$, $\Delta v_{C1,1}$, and $\Delta v_{C1,3}$ can be rewritten as follows:

$$\Delta i_{L1,1} = \frac{v_{ref}}{Rv_g}\left(\sqrt{\frac{2L_2R}{fL_1(L_1+L_2)}} + \frac{L_1v_{ref}-L_2v_g}{L_1+L_2} - v_{ref}\right), \tag{5.29}$$

$$\Delta i_{L2,1} = \frac{v_{ref}}{Rv_g}\left(\sqrt{\frac{2L_1R}{fL_2(L_1+L_2)}} - \frac{L_1v_{ref}-L_2v_g}{L_1+L_2} - v_g\right), \tag{5.30}$$

$$\Delta v_{C1,1} = \frac{L_1v_{ref}^2}{2C_1Rv_g^2}\left(\sqrt{\frac{2L_1R}{fL_2(L_1+L_2)}} - \frac{L_1v_{ref}-L_2v_g}{L_1+L_2} - v_g\right)^2, \tag{5.31}$$

$$\Delta v_{C1,3} = \frac{L_2v_{ref}^2}{2C_1R^2v_g}\left(1 + \frac{L_1v_{ref}-L_2v_g}{v_g(L_1+L_2)}\right)^2. \tag{5.32}$$

Furthermore, ρ_1 is computed by substituting (5.29) to (5.32) into (5.17) while ρ_3 is found by inserting (5.32) into (5.18). It is worthwhile to highlight that the steady-state switching frequency f appears in the function (5.29) to (5.31), of which, an inverse proportional relationship is shown. Therefore, by pre-defined f, one can systematically decide the steady-state switching frequency for the Zeta converter to operate.

5.5 Simulation Results

In this section, to verify the effectiveness of the proposed Hybrid DCM System Control Strategy 2, a circuit-based simulation is conducted under PSIM environment. The simulation circuit for the DC-DC Zeta converter with the hybrid control is constructed as in Figure 5.2, using circuit parameters tabulated in Table 5.1. Internal resistance for each of the parameters is assumed small and therefore neglected.

To provide the data for the online switching control computation, besides the four state-variables i_{L1}, i_{L2}, v_{C1}, and v_{C2}, an additional two variables are sensed from the circuit, namely, the input voltage v_g and the load current i_o, to increase the controller's robustness. Notice that load current i_o is measured to monitor the change of load R using the following equality $R = \frac{v_{C2}}{i_o}$. To minimize the online computational burden, the switching functions α_1 (5.9) and α_3 (5.11), and the thresholds functions ρ_1 (5.17) and ρ_3 (5.18) are pre-computed offline using parameters in Table 5.1, which can be rewritten as

$$\alpha_1 = v_g(i_{L1} + i_{L2}) - i_o\left(\frac{5}{v_{C2}}(v_{C1} + v_g + 5) + v_{C2} - 10\right), \tag{5.33}$$

$$\alpha_3 = \frac{i_o}{2}\left(\frac{25}{v_g}\left(\frac{v_{C1}}{v_{C2}} - 1\right) - 2v_{C2} - \frac{5v_{C1}}{v_{C2}} + 15\right), \tag{5.34}$$

$$\rho_1 = \frac{5v_g i_o}{v_{C2}}\left(\sqrt{\frac{2v_{C2}}{i_o}} - \frac{5}{v_g} - 1\right)\left(\frac{25i_o^2}{8v_g^2 v_{C2}^2}\left(\sqrt{\frac{2v_{C2}}{i_o}} - \frac{5}{v_g} - 1\right) + 1\right), \tag{5.35}$$

$$\rho_3 = -\frac{625i_o^3}{8v_{C2}^3 v_g^2}\left(1 + \frac{5}{v_g}\right)^2. \tag{5.36}$$

respectively.

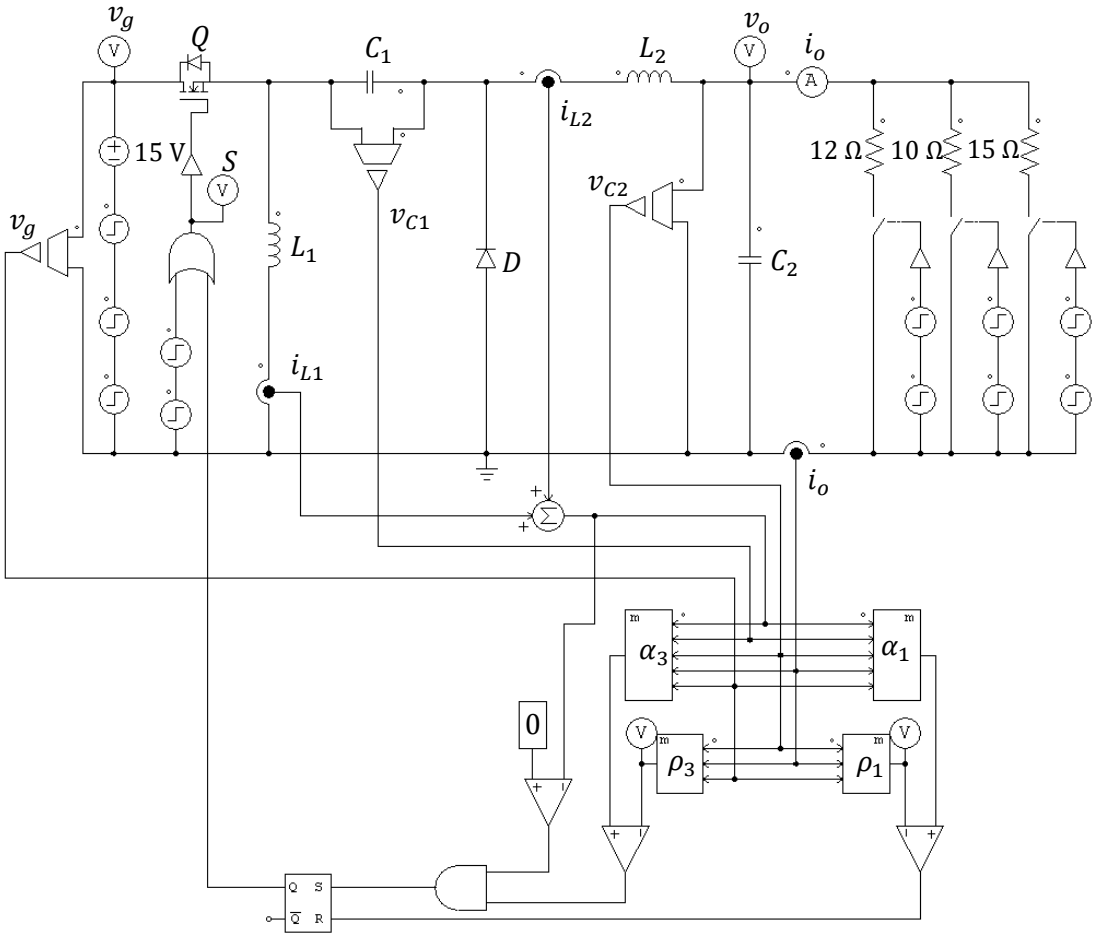

Figure 5.2: Simulation circuit of a DC-DC Zeta converter hybrid system control in DCM operation.

The simulation results under the input voltage v_g and the load R perturbations are illustrated in Figure 5.3. The variations of the output voltage v_o, the load current i_o, the input voltage v_g, and the switching S are shown in Figure 5.3(a), Figure 5.3(b), Figure 5.3(c), and Figure 5.3(d), respectively. Under nominal input voltage $15\ \mathrm{V}$ and load $12\ \Omega$ (implies $i_o = 0.42\ \mathrm{A}$), no overshoot is seen at the output voltage and the load current during start-up, albeit some oscillations are observed, and they settled approximately

under $25\,\text{ms}$. At $t = 30\,\text{ms}$, the input voltage is increased by $+20\,\%$, and the load is decreased by $-16.7\,\%$, to settle at $18\,\text{V}$ and $10\,\Omega$ ($i_o = 0.5\,\text{A}$), respectively. As can be seen in the figure, both the output voltage and the load current transient responses can be considered negligible. Moreover, at $t = 60\,\text{ms}$, the input voltage is dropped to $10\,\text{V}$ ($-44.4\,\%$) and the load is increased by $+50\,\%$ to $15\,\Omega$ ($i_o = 0.33\,\text{A}$). Due to the large perturbations, an oscillation is observed at the output voltage and the load current. Finally, at $t = 90\,\text{ms}$, the input voltage and the load are returned to their nominal value $15\,\text{V}$ ($+50\,\%$) and $12\,\Omega$ ($+20\,\%$), respectively. Despite considerably large perturbations, the switching control has no problem in regulating the output voltage.

In Figure 5.4, the close view of the inductor currents i_{L1} and i_{L2}, and the switching S, see, respectively, top and bottom of Figure 5.4(a), Figure 5.4(b), and Figure 5.4(c), at the operating point is presented . As observed in the three figures, under three combinations of the input voltage $15\,\text{V}$, $18\,\text{V}$, and $10\,\text{V}$, and load $12\,\Omega$, $15\,\Omega$, and $10\,\Omega$, respectively, the switching control is able maintain the DCM operation for the three conditions, as can be observed by the discontinuity of both steady-state inductor currents. On the other hand, by looking at the switching signal, the switching frequencies generated by the hybrid system control under $v_g = 15\,\text{V}$ and $R = 12\,\Omega$ (see bottom of Figure 5.4(a)), $v_g = 18\,\text{V}$ and $R = 10\,\Omega$ (bottom of Figure 5.4(b)), and (c) $v_g = 10\,\text{V}$ and $R = 15\,\Omega$ (bottom of Figure 5.4(c)), are given by $20.11\,\text{kHz}$, $19.82\,\text{kHz}$, and $19.18\,\text{kHz}$, respectively. Since the desired switching frequency is $20\,\text{kHz}$, there are slight discrepancies of $+0.55\,\%$, $-0.90\,\%$, and $-4.10\,\%$, respectively.

Table 5.1: The DC-DC Zeta converter parameters in DCM operation.

Parameter	**Value**
v_g	15 V
$v_o(v_r)$	5 V
R	12 Ω
L_1	100 μH
L_2	100 μH
C_1	100 μF
C_2	220 μF
f	20 kHz

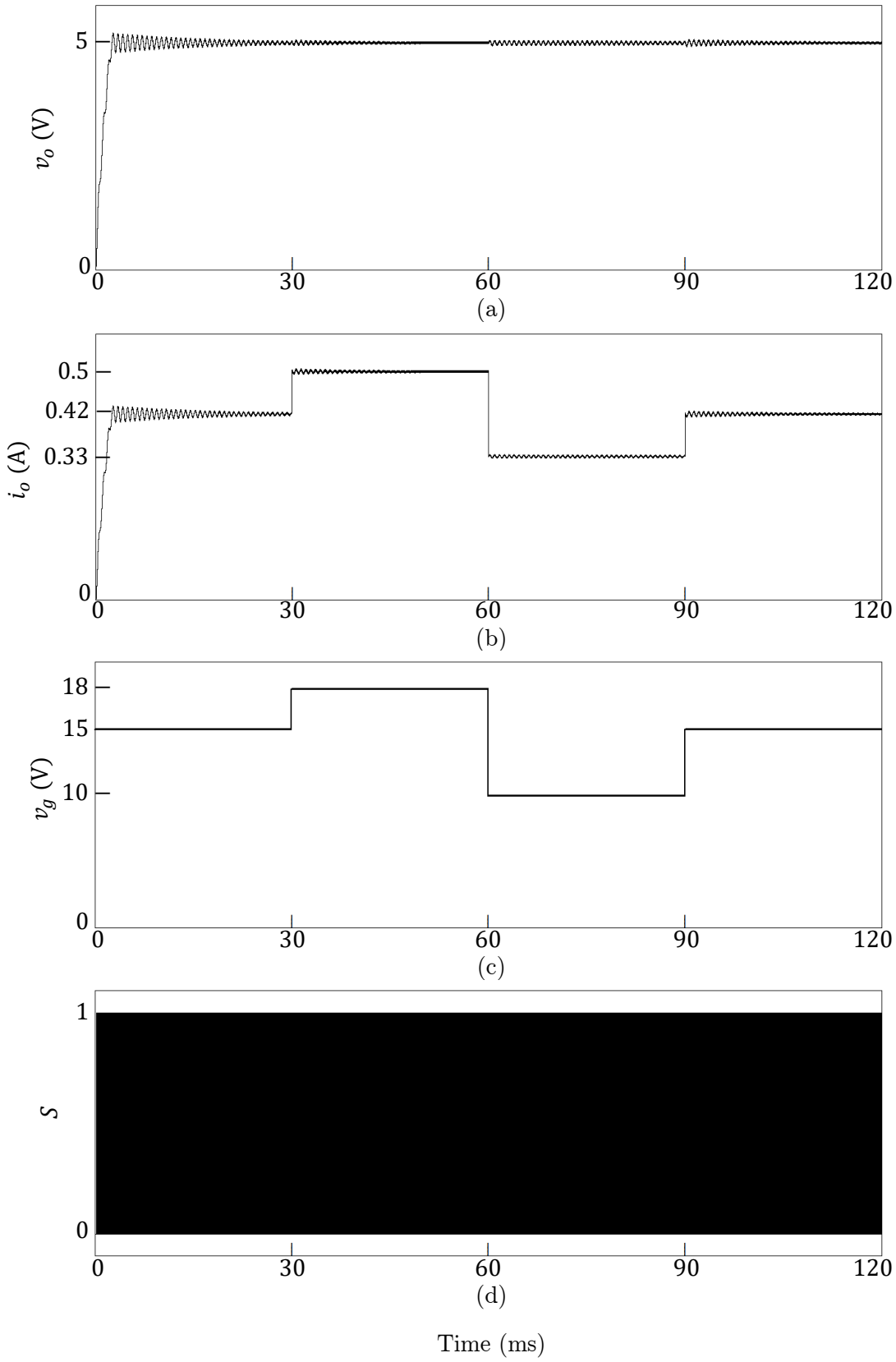

Figure 5.3: Simulated response in DCM operation under input voltage v_g and load R perturbations. Variations in (a) output voltage v_o, (b) load current i_o, (c) input voltage v_g, and (d) switching S.

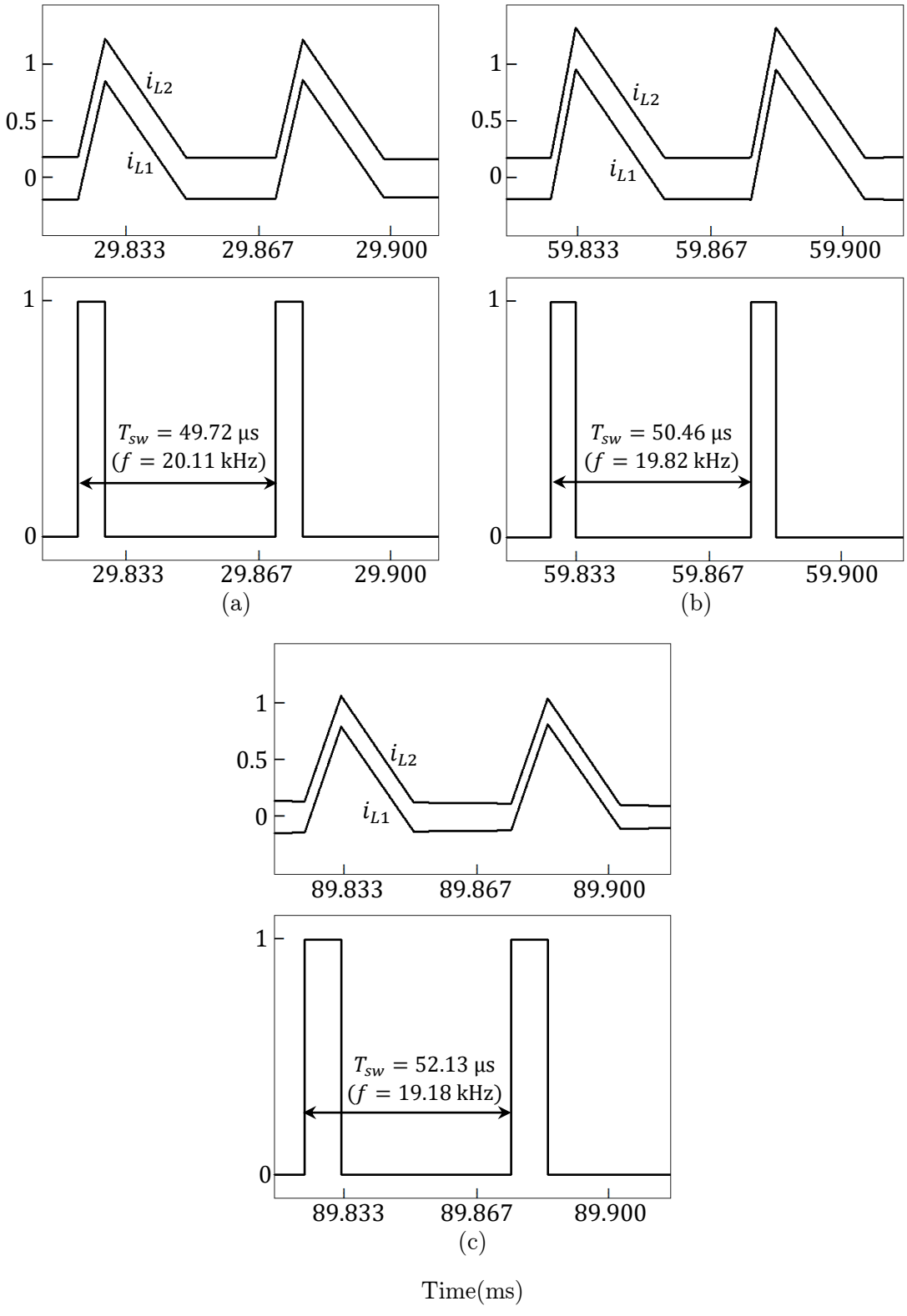

Figure 5.4: Close view of inductor currents i_{L1} and i_{L2}, and switching S at the operating point in DCM operation under (a) $v_g = 15\,\text{V}$ and $R = 12\,\Omega$, (b) $v_g = 18\,\text{V}$ and $R = 10\,\Omega$, and (c) $v_g = 10\,\text{V}$ and $R = 15\,\Omega$.

5.6 Summary

In this chapter, we propose a hybrid system control strategy for the stabilization of a DC-DC Zeta converter operating in discontinuous conduction mode (DCM). In essence, the hybrid three-mode system control strategy presented in this chapter is the extension of a hybrid two-mode system control discussed in Chapter 4. We give a stability analysis that is simple but sufficient to prove the stability of the hybrid control system strategy in DCM operation. We analyze the states waveforms in DCM operation and find an explicit relation between the hybrid system control strategy and the switching frequency. Overall, the hybrid system control strategy works well in regulating the output voltage and maintaining the DCM operation even under large operating point deviations while producing the desired steady-state switching frequency.

Chapter 6

Conclusion

6.1 Conclusion

We have presented the control techniques for the stabilization of a DC-DC Zeta converter based on two distinctive systems; average-based system and hybrid system. The average-based system control technique is applied to a Zeta converter operating in continuous conduction mode (CCM). The design of the controller is based on state-space averaging (SSA) approach and corresponding linear approximation model. In SSA approach, the dynamics of the two-mode system is averaged over a switching period, to produce a Zeta converter model with a single system representation. On the other hand, a hybrid system control is realized to a Zeta converter under CCM and discontinuous conduction mode (DCM) operation. In hybrid system, the continuous and discrete dynamics of the Zeta converter are considered. For each mode of the two-mode and three-mode system operating in CCM and DCM respectively, a switching function based on the continuous dynamics of the converter is defined, consequently, is used to enforce the discrete switching action of the hybrid control.

The first contribution of this thesis was given in Chapter 3, where the main result has been published in [37]. Using average-based system control technique, we have proposed a state-feedback control of the uncertain DC-DC Zeta converter operating in CCM. We have chosen the input voltage and the load as uncertain parameters. We have produced two versions of convex polytope of uncertainty; formed by 16 vertices and eight vertices. We have represented linear quadratic regulator (LQR) problem in the form of linear matrix inequality (LMI), denoted as LMI-LQR. With the help of Matlab LMI solver, we have calculated two state-feedback gain vectors, denoted as K_{LMI16} and K_{LMI8}, which satisfies the LMI-LQR at all 16 and 8 vertices of the convex polytope of uncertainty. The conventional LQR controller K_{LQR} is also added for comparison

purpose. From the simulated response, we have found that controllers K_{LMI16} and K_{LMI8} are highly robust albeit significant changes in the operating point, and that controller K_{LQR} was failed to bring back the operating point. However, we have identified that controller K_{LMI8} is the viable option in practice to avoid pulse width modulation (PWM) circuitry problem. From this observation, we have shown the importance of having a reduce convex polytope covering in the control design.

Chapter 4 has discussed the second contribution of this thesis, with a paper published in [39]. We have presented a hybrid system control strategy for a DC-DC Zeta converter in CCM operation, where the Zeta converter is modelled by a class of differential inclusions. We have proposed two switching functions by exploiting the derivative of Lyapunov function along the trajectories $\dot{V}(x)$. We have defined a Hybrid CCM System Control Strategy 1, based on the signs of $\dot{V}(x)$, and analyzed the local asymptotic stability using LaSalle's invariance principle for a class of differential inclusions. Because the current control strategy produces unbounded number of switching, we have proposed a modified control strategy defined by Hybrid CCM System Control Strategy 2, where we allowed $\dot{V}(x)$ to be positive, and we have proven $\dot{V}(x)$ can be bounded by a positive threshold ρ. Furthermore, we have analyzed the approximated CCM states waveform at the operating point, and we have found that ρ is inversely proportional to the switching frequency. We have verified, through simulation, the effectiveness of our hybrid system switching control strategy. We have shown that the Zeta converter can be stabilized even with the existence of large input voltage and load perturbations, and the simulated switching frequency is approximately equal to the predefined switching frequency.

For the final contribution of this thesis, the result has been published in [42] and was presented in Chapter 5. We have proposed a hybrid DC-DC Zeta converter control strategy under DCM operation. We have extended the method used in Chapter 4, by defining a third switching function for the third mode based on the control Lyapunov function candidate. We have analyzed the local asymptotic stability of the differential equations of the three-mode Zeta converter model under the defined Hybrid DCM System Control Strategy 1. Similarly, we have improved the current hybrid control to alleviate the infinite switching issue with the introduction of Hybrid DCM System Control Strategy 2. To ensure the Zeta converter operates at the desired DCM switching frequency, we established an explicit relation between the Hybrid DCM System Control Strategy 2 and the switching frequency. To achieve this, we have analyzed the approximated steady-state states waveform operating in DCM. Based on the outcome of the simulation, we have proved that the proposed method is able to regulate the output voltage of the Zeta converter and produce the desired switching frequency.

6.2 Recommendation

For the average-based system control, it is immediate to propose the extension of the LMI-LQR control method to a DC-DC Zeta converter under DCM operation. Furthermore, a linear parameter-varying (LPV) system with specific transient performance criteria such as maximum output voltage overshoot and settling time can be considered.

In Chapter 5, through simulation, the three-mode system of the Zeta converter is proven to be stable under the improved hybrid system control strategy. However, the theoretical stability analysis has not been carried out. Therefore, a theoretical analysis could be established to prove the practical stability of the hybrid control operating in DCM. Moreover, a practical stability analysis under a unified hybrid system control strategy for both CCM and DCM operation may be established.

As for the DC-DC Zeta converter, the parameters are assumed ideal. If the proposed average-based and hybrid system controllers are to be implemented in practice, a lower operating point level is expected due to the Zeta converter model inaccuracy. Thus, it is recommended to consider internal resistance, and the diode could be replaced with a MOSFET, to achieve better efficiency. Moreover, a discrete hybrid system control with a model predictive control that produces fast online computation can be studied.

Bibliography

[1] R. L. Boylestad and L. Nashelsky, *Electronic Devices and Circuit Theory*, Eleventh Edition, Pearson, 2013.

[2] T. L. Flyod, *Electronic Devices (Conventional Current Version)*, Ninth Edition, Prentice Hall, 2012.

[3] M. H. Rashid, *Power Electronics Handbook*, Academic Press, 2001.

[4] G. Pepermans, J. Driesen, D. Haeseldonckx, R. Belmans, and W. Dhaeseleer, "Distributed generation: definition, benefits and issues", *Energy Policy*, *Elsevier*, vol. 33, no. 6, pp. 787–798, 2005.

[5] M. Prauzek, J. Konecny, M. Borova, K. Janosova, J. Hlavica, and P. Musilek, "Energy Harvesting Sources, Storage Devices and System Topologies for Environmental Wireless Sensor Networks: A Review", *Sensors*, *MDPI*, vol. 18, no. 8, pp. 1–22, 2018.

[6] H. Nagayoshi, "I–V curve simulation by multi-module simulator using I–V magnifier circuit", *Solar Energy Materials and Solar Cells*, vol. 82, pp. 159–167, 2004.

[7] K. V. G. Raghavendra, K. Zeb, A. Muthusamy, T. N. V. Krishna, S. V. P. Kumar, D. H. Kim, M. S. Kim, H. G. Cho, and H. J. Kim, "A Comprehensive Review of DC–DC Converter Topologies and Modulation Strategies with Recent Advances in Solar Photovoltaic Systems", *Electronics*, *MDPI*, vol. 9, no. 31, pp. 1–41, 2019.

[8] Z. Li and D. Pommerenke, "EMI specifics of synchronous DC-DC buck converters", *in Proceedings of the 2005 International Symposium on Electromagnetic Compatibility,* pp. 711–714, Chicago, USA, August 8–12, 2005.

[9] W.T Yan, C.N.M Ho, H.S.H Chung, and K.T.K. Au, "Fixed-Frequency Boundary Control of Buck Converter With Second-Order Switching Surface", *IEEE Transactions on Power Electronics*, vol. 24, no. 9, pp. 2193–2201, 2009.

[10] C.C. Chan and K.T. Chau, "A new zero-voltage switching DC/DC boost converter", *IEEE Transactions on Aerospace and Electronic Systems*, vol. 29, no. 1, pp. 125–134, 1993.

[11] E. Lefeuvre, D. Audigier, C. Richard, and D. Guyomar, "Buck-Boost Converter for Sensorless Power Optimization of Piezoelectric Energy Harvester", *IEEE Transactions on Power Electronics*, vol. 22, no. 5, pp. 2018–2025, 2007.

[12] K.M. Smedley and S. Cuk, "Dynamics of one-cycle controlled Cuk converters", *IEEE Transactions on Power Electronics*, vol. 10, no. 6, pp. 634–639, 1995.

[13] A. Peres, D.C. Martins, and I. Barbi, "ZETA converter applied in power factor correction", *in Proceedings of 1994 Power Electronics Specialists Conference*, pp. 1152–1157, Taipei, Taiwan, June 20–25, 1994.

[14] D. Maksimovic and S. Cuk, "Switching converters with wide DC conversion range", *IEEE Transactions on Power Electronics,* vol. 6, no. 1, pp. 151–157, 1991.

[15] F. Bayat, M. Karimi, and A. Taheri, Robust output regulation of Zeta converter with load/input variations: LMI approach", *Control Engineering Practice*, *Elsevier*, vol. 84, no. 3, pp. 102–111, 2019.

[16] R. W. Erickson and D. Maksimovic, *Fundamentals of Power Electronics*, Second Edition. Kluwer Academic Publishers Group, 2000.

[17] H. K. Khalil, *Nonlinear Systems*, Third Edition. Prentice Hall, 2002.

[18] C. Sreekumar and V. Agarwal, "Hybrid control approach for the output voltage regulation in buck type DC–DC converter", *IET Electric Power Applications*, vol. 1 no. 6, pp. 897–906, 2007.

[19] E. Vuthchhay and C. Bunlaksananusorn, "Modeling and Control of a Zeta Converter", *in Proceedings of The 2010 International Power Electronics Conference*, pp. 612–619, Sapporo, Japan, June 21–24, 2010.

[20] M. M. Garg, Y. V. Hote, and M. K. Pathak, "PI Controller Design of a dc-dc Zeta Converter for Specific Phase Margin and Cross-over Frequency", *in Proceeding of the 10th Asian Control Conference*, pp. 1–6, Kota Kinabalu, Malaysia, May 31– June 23, 2015.

[21] P.R. Babu, S.R. Prasath, and R. Kiruthika, "Simulation and Performance Analysis of CCM Zeta Converter with PID Controller", *in Proceedings of 2015 International Conference on Circuit, Power and Computing Technologies*, pp. 1–7, Nagercoil, India, March 19–20, 2015.

[22] S. Arun and T. Manigandan, "Design of ACO based PID controller for zeta converter using reduced order methodology", *Microprocessors and Microsystems*, *Elsevier*, vol. 81, pp. 1–11, 2021.

[23] A. Izadian and P. Khayyer, "Complementary adaptive control of Zeta converters", *in Proceedings of the 2013 International Electric Machines & Drives Conference*, pp. 1338–134, Chicago, USA, May 12-15, 2013.

[24] B. Moaveni, H. Abdollahzadeh, and M. Mazoochi, "Adjustable Output Voltage Zeta Converter Using Neural Network Adaptive Model Reference Control", *in Proceedings of 2011 2nd International Conference on Control, Instrumentation and Automation*, pp. 552–557, Nagercoil, India, March 19–20, 2015.

[25] N. Priyadarshi, K. Yadav, V. Kumar, and M. Vardia, *An experimental study on zeta buck–boost converter for application in pv system.* In Handbook of distributed generation (pp. 393–406). Springer, 2017.

[26] H. Sarkawi, M. H. Jali, T. A. Izzuddin, and M. Dahari, "Dynamic Model of Zeta Converter with Full-state Feedback Controller Implementation", *International Journal of Research in Engnieering and Technology, eSAT*, vol. 2, no. 8, pp. 34–43, 2013.

[27] H. Sarkawi and Y. Ohta, "Optimal state-feedback and Proportional-Integral Controller Performance Comparison for Dc-dc Zeta Converter Operating in Continuous Conduction Mode", *in Proceedings of the SICE Annual Conference 2016,* pp. 448–451, Tsukuba, Japan, September 20–23, 2016.

[28] C. Sreekumar and V. Agarwal, "A Hybrid Control Algorithm for Voltage Regulation in DC–DC Boost Converter", *IEEE Transactions on Industrial Electronics*, vol. 55, no. 6, pp. 2530–2538, 2008.

[29] M. Hongbo and F. Quanyuan, "Hybrid Modeling and Control for Buck-Boost Switching Converters", *in Proceeding of International Conference on Communications, Circuits and Systems*, pp. 678–682, Milpitas, CA, USA, July 23–25, 2009.

[30] P. Gupta and A. Patra, "Hybrid Mode-Switched Control of DC–DC Boost Converter Circuits", *IEEE Transactions on Circuits and Systems-II: Express Briefs*, vol. 52, no. 11, pp. 734–738, 2005.

[31] G.S. Deaecto, J.C. Geromel, F.S. Garcia, and J.A. Pomilio, "Switched affine systems control design with application to DC–DC converters", *Control Theory & Applications*, *IET*, vol. 4, no. 7, pp. 1201–1210, 2010.

[32] C. Albea, G. Garcia, and L. Zaccarian, "Hybrid dynamic modeling and control of switched affine systems: application to DC-DC converters", *in IEEE 54th Annual Conference on Decision and Control (CDC)*, pp. 2264–2269, Osaka, Japan, December 15–18, 2015.

[33] T. A. F. Theunisse, J. Chai, R. Sanfelice, and W. P. M. H. Heemels, "Robust Global Stabilization of the DC-DC Boost Converter via Hybrid Control", *IEEE Transactions on Circuit and Systems–I: Regular Papers*, vol. 62, no. 4, pp. 1052–1061, 2015.

[34] L. Hetel and E. Fridman, "Robust sampled-data control of switched affine systems", *IEEE Transactions on Automatic Control*, vol. 58, no. 11, pp. 2922–2928, 2013.

[35] X. Yan, Z. Shu, S. M. Sharkh, Z. G. Wu, and M. Z. Q. Chen, "Sampled-data control with adjustable switching frequency for dc-dc converters", *IEEE Transactions on Industrial Electronics*, vol. 66, no. 10, pp. 8060–8071, 2019.

[36] H. Sarkawi and Y. Ohta, "Comparison of Conventional LQR and LMI based LQR Controller Performance on the Dc-dc Zeta Converter with Parameters Uncertainty", *in Proceedings of the 4th SICE Multi-symposium on Control System,* pp. 642–647, Okayama, Japan, March 6–9, 2017.

[37] H. Sarkawi and Y. Ohta, "Uncertain Dc-dc Zeta Converter Control in Convex Polytope Model Based on LMI Approach", *International Journal of Power Electronics and Drive System*, *IAES*, vol. 9, no. 2, pp. 829–838, 2018.

[38] H. Sarkawi, Y. Ohta, and P. Rapisarda "Preliminary Finding on the Switching Control Algorithm for the Stabilization of the Dc-dc Zeta Converter", *in Proceedings of the SICE Annual Conference 2018,* pp. 971–974, Nara, Japan, September 11–14, 2018.

[39] H. Sarkawi, Y. Ohta, and P. Rapisarda, "On the switching control of the DC–DC zeta converter operating in continuous conduction mode", *Control Theory & Applications*, *IET*, vol. 15, no. 9, pp. 1185–1198, 2021.

[40] H. Sarkawi, Y. Ohta, and P. Rapisarda, "Comparative Study of PWM-based versus Hybrid Control for the DC-DC Zeta Converter Voltage Regulation", *in Proceedings of the SICE International Symposium of Control System 2019*, pp. 498–504, Kumamoto, Japan, March 7–9, 2019.

[41] H. Sarkawi, Y. Ohta, and P. Rapisarda, "On the Hybrid Control of the Dc-dc Zeta Converter in Discontinuous Conduction Mode: Preliminary Finding", *in Proceedings of the 61st Japan Joint Automatic Control Conference*, pp. 126–130, Nagoya, Japan, November 17–18, 2018.

[42] H. Sarkawi and Y. Ohta, "The DC-DC Zeta Converter Hybrid Control Operating in Discontinuous Conduction Mode", *in Proceedings of the 2019 IEEE Conference on Control Technology and Applications (CCTA),* pp. 112–117, Hong Kong, China, August 19–21, 2019.

[43] C. Olalla, R. Leyva, A. E. Aroudi, and S. Queinnec, "Robust LQR Control for PWM Converters: An LMI Approach", *IEEE Transactions on Industrial Electronics*, vol. 56, no. 7, pp. 2548–2558, 2009.

[44] S. Boyd, L. E. Ghaoui, E. Feron, and V. Balakrishnan, *Linear Matrix Inequalities in Systems and Control Theory*, SIAM Studies in Applied and Numerical Mathematics, vol. 15. Philadelphia, PA: SIAM, 1994.

[45] K. Ogata, *Modern Control Engineering*, Second Edition, Prentice Hall, 2002.

[46] B. D. O. Anderson and J. B. Moore, *Optimal Control: Linear Quadratic Methods*, New Edition, Prentice Hall, 1990.

[47] A. E. Aroudi, E. Alarcon, E. Rodriguez, R. Leyva, G. Villar, F. Guinjoan, and A. Poveda, "Ripple based index for predicting fast-scale instability of dc–dc converters in CCM and DCM", *in Proceedings of IEEE International Conference on Industrial Technology*, pp. 1949–1953, Mumbai, India, December 15–17, 2006.

[48] E. Rodriguez, G. Villar, F. Guinjoan, A. Poveda, A. El Aroudi, and E. Alarcon, "General-purpose ripple-based fast-scale instability prediction in switching power regulators", *in Proceedings of IEEE International Symposium on Circuits and Systems*, pp. 2423–2426, New Orleans, LA, USA, May 27–30, 2007.

[49] P. Gahinet, A. Nemirovski, A. J. Laub, and M. Chilali, *LMI Control Toolbox for Use with Matlab.* Natick, MA: The MathWorks, Inc., 1995.

[50] M. Vidyasagar, *Nonlinear Systems Analysis,* Second Edition. Englewood Cliffs, New Jersey: Prentice-Hall, 1993.

[51] J.P. Aubin and A. Cellina, *Differential Inclusions,* First Edition. Berlin Heidelberg: Springer-Verlag, 1984.

Appendix A: List of Author's Work

Journals

1. Hafez Sarkawi and Yoshito Ohta, "Uncertain Dc-dc Zeta Converter Control in Convex Polytope Model Based on LMI Approach", *International Journal of Power Electronics and Drive System*, *IAES*, vol. 9, no. 2, pp. 829–838, 2018.
2. Hafez Sarkawi, Yoshito Ohta, and Paolo Rapisarda, "On the switching control of the DC–DC zeta converter operating in continuous conduction mode", *Control Theory & Applications*, *IET*, vol. 15, no. 9, pp. 1185–1198, 2021.

Conference Proceedings

1. Hafez Sarkawi and Yoshito Ohta, "Optimal state-feedback and Proportional-Integral Controller Performance Comparison for Dc-dc Zeta Converter Operating in Continuous Conduction Mode", *in Proceedings of the SICE Annual Conference 2016 (SICE 2016),* pp. 448–451, Tsukuba, Japan, September 20–23, 2016.
2. Hafez Sarkawi and Yoshito Ohta, "Comparison of Conventional LQR and LMI based LQR Controller Performance on the Dc-dc Zeta Converter with Parameters Uncertainty", *in Proceedings of the 4th SICE Multi-symposium on Control System (MSCS 2017),* pp. 642–647, Okayama, Japan, March 6–9, 2017.
3. Hafez Sarkawi, Yoshito Ohta, and Paolo Rapisarda "Preliminary Finding on the Switching Control Algorithm for the Stabilization of the Dc-dc Zeta Converter", *in Proceedings of the SICE Annual Conference 2018 (SICE 2018),* pp. 971–974, Nara, Japan, September 11–14, 2018.

4. Hafez Sarkawi, Yoshito Ohta, and Paolo Rapisarda, "On the Hybrid Control of the Dc-dc Zeta Converter in Discontinuous Conduction Mode: Preliminary Finding", *in Proceedings of the 61st Japan Joint Automatic Control Conference*, pp. 126–130, Nagoya, Japan, November 17–18, 2018.

5. Hafez Sarkawi, Yoshito Ohta, and Paolo Rapisarda, "Comparative Study of PWM-based versus Hybrid Control for the DC-DC Zeta Converter Voltage Regulation", *in Proceedings of the SICE International Symposium of Control System 2019 (SICE ISCS 2019)*, pp. 498–504, Kumamoto, Japan, March 7–9, 2019.

6. Hafez Sarkawi and Yoshito Ohta, "The DC-DC Zeta Converter Hybrid Control Operating in Discontinuous Conduction Mode", *in Proceedings of the 2019 IEEE Conference on Control Technology and Applications (CCTA 2019),* pp. 112–117, Hong Kong, China, August 19–21, 2019.

Appendix B: Matlab Code for State-feedback Controller K_{LQR}

```
%Define nominal matrix A and B
A = [0 0 -6.25E+03 0 0; 0 0 6.82E+03 -1.82E+04 0; 6.25E+03 -3.75E+03
0 0 0; 0 5.00E+03 0 -3.33E+03 0; 0 0 0 -1 0];
B = [2.40E+05; 4.36E+05; -9.6E+04; 0; 0];


%Define LQR performance index
Q = [0 0 0 0 0; 0 1E-4 0 0 0; 0 0 0 0 0; 0 0 0 1E-4 0; 0 0 0 0 5E+06];
R = 1;


setlmis([]);   %LMI system initialization


%Define variable matrices
P = lmivar(1,[5 1]);
X = lmivar(1,[1 1]);
Y = lmivar(2,[1 5]);


%Define LMI constraint AP+PA'-BY-Y'B+I<0 for the nominal plant
lmiterm([1 1 1 P],A,1,'s'); lmiterm([1 1 1 Y],-B,1,'s');  lmiterm([1
1 1 0],1);


%Define LMI constraint [X (R^0.5)Y; Y'(R^0.5) P]>0
lmiterm([-2 1 1 X],1,1);
lmiterm([-2 2 1 -Y],1,R^0.5);
lmiterm([-2 2 2 P],1,1);


%Define constraint P>0
lmiterm([-3 1 1 P],1,1);

LMIs = getlmis;   %LMI system internal description

%Find and set the storage size based on number of uncertain plants
n = decnbr(LMIs);
c = zeros(n,1);
```

```
%Objective function
for j=1:n,
    [Pj,Xj,Yj] = defcx(LMIs,j,P,X,Y);
    c(j) = trace(Q*Pj) + trace(Xj);
end

options = [1e-6,0,0,0,0];
[copt,xopt] = mincx(LMIs,c,options);

Popt = dec2mat(LMIs,xopt,P);    %Find the optimal P matrix
Yopt = dec2mat(LMIs,xopt,Y);    %Find the optimal Y matrix

K_LQR = Yopt*(inv(Popt))       %Compute controller K_LQR
```

Appendix C: Matlab Code for State-feedback Controller K_{LMI16}

```
%Define 16 matrices of the convex polytope
A1 = [0 0 -6.25E+03 0 0; 0 0 6.82E+03 -1.82E+04 0; 6.25E+03 -3.75E+03
0 0 0; 0 5.00E+03 0 -1.67E+03 0; 0 0 0 -1 0];
B1 = [2.40E+05; 4.36E+05; -4.80E+04; 0; 0];

A2 = [0 0 -6.25E+03 0 0; 0 0 6.82E+03 -1.82E+04 0; 6.25E+03 -3.75E+03
0 0 0; 0 5.00E+03 0 -3.33E+03 0; 0 0 0 -1 0];
B2 = [2.40E+05; 4.36E+05; -4.80E+04; 0; 0];

A3 = [0 0 -6.25E+03 0 0; 0 0 6.82E+03 -1.82E+04 0; 6.25E+03 -3.75E+03
0 0 0; 0 5.00E+03 0 -1.67E+03 0; 0 0 0 -1 0];
B3 = [2.40E+05; 4.36E+05; -3.75E+05; 0; 0];

A4 = [0 0 -6.25E+03 0 0; 0 0 6.82E+03 -1.82E+04 0; 6.25E+03 -3.75E+03
0 0 0; 0 5.00E+03 0 -3.33E+03 0; 0 0 0 -1 0];
B4 = [2.40E+05; 4.36E+05; -3.75E+05; 0; 0];

A5 = [0 0 -6.25E+03 0 0; 0 0 6.82E+03 -1.82E+04 0; 6.25E+03 -3.75E+03
0 0 0; 0 5.00E+03 0 -1.67E+03 0; 0 0 0 -1 0];
B5 = [3.75E+05; 6.82E+05; -4.80E+04; 0; 0];

A6 = [0 0 -6.25E+03 0 0; 0 0 6.82E+03 -1.82E+04 0; 6.25E+03 -3.75E+03
0 0 0; 0 5.00E+03 0 -3.33E+03 0; 0 0 0 -1 0];
B6 = [3.75E+05; 6.82E+05; -4.80E+04; 0; 0];

A7 = [0 0 -6.25E+03 0 0; 0 0 6.82E+03 -1.82E+04 0; 6.25E+03 -3.75E+03
0 0 0; 0 5.00E+03 0 -1.67E+03 0; 0 0 0 -1 0];
B7 = [3.75E+05; 6.82E+05; -3.75E+05; 0; 0];

A8 = [0 0 -6.25E+03 0 0; 0 0 6.82E+03 -1.82E+04 0; 6.25E+03 -3.75E+03
0 0 0; 0 5.00E+03 0 -3.33E+03 0; 0 0 0 -1 0];
B8 = [3.75E+05; 6.82E+05; -3.75E+05; 0; 0];

A9 = [0 0 -4.00E+03 0 0; 0 0 1.09E+04 -1.82E+04 0; 4.00E+03 -6.00E+03
0 0 0; 0 5.00E+03 0 -1.67E+03 0; 0 0 0 -1 0];
B9 = [2.40E+05; 4.36E+05; -4.80E+04; 0; 0];

A10 = [0 0 -4.00E+03 0 0; 0 0 1.09E+04 -1.82E+04 0; 4.00E+03 -6.00E+03
0 0 0; 0 5.00E+03 0 -3.33E+03 0; 0 0 0 -1 0];
B10 = [2.40E+05; 4.36E+05; -4.80E+04; 0; 0];
```

```
A11 = [0 0 -4.00E+03 0 0; 0 0 1.09E+04 -1.82E+04 0; 4.00E+03 -6.00E+03
0 0 0; 0 5.00E+03 0 -1.67E+03 0; 0 0 0 -1 0];
B11 = [2.40E+05; 4.36E+05; -3.75E+05; 0; 0];

A12 = [0 0 -4.00E+03 0 0; 0 0 1.09E+04 -1.82E+04 0; 4.00E+03 -6.00E+03
0 0 0; 0 5.00E+03 0 -3.33E+03 0; 0 0 0 -1 0];
B12 = [2.40E+05; 4.36E+05; -3.75E+05; 0; 0];

A13 = [0 0 -4.00E+03 0 0; 0 0 1.09E+04 -1.82E+04 0; 4.00E+03 -6.00E+03
0 0 0; 0 5.00E+03 0 -1.67E+03 0; 0 0 0 -1 0];
B13 = [3.75E+05; 6.82E+05; -4.80E+04; 0; 0];

A14 = [0 0 -4.00E+03 0 0; 0 0 1.09E+04 -1.82E+04 0; 4.00E+03 -6.00E+03
0 0 0; 0 5.00E+03 0 -3.33E+03 0; 0 0 0 -1 0];
B14 = [3.75E+05; 6.82E+05; -4.80E+04; 0; 0];

A15 = [0 0 -4.00E+03 0 0; 0 0 1.09E+04 -1.82E+04 0; 4.00E+03 -6.00E+03
0 0 0; 0 5.00E+03 0 -1.67E+03 0; 0 0 0 -1 0];
B15 = [3.75E+05; 6.82E+05; -3.75E+05; 0; 0];

A16 = [0 0 -4.00E+03 0 0; 0 0 1.09E+04 -1.82E+04 0; 4.00E+03 -6.00E+03
0 0 0; 0 5.00E+03 0 -3.33E+03 0; 0 0 0 -1 0];
B16 = [3.75E+05; 6.82E+05; -3.75E+05; 0; 0];


%Define LQR performance index
Q = [0 0 0 0 0; 0 1E-4 0 0 0; 0 0 0 0 0; 0 0 0 1E-4 0; 0 0 0 0 5E+06];
R = 1;


setlmis([]);   %LMI system initialization


%Define variable matrices
P = lmivar(1,[5 1]);
X = lmivar(1,[1 1]);
Y = lmivar(2,[1 5]);


%Define LMI constraint AP+PA'-BY-Y'B+I<0 for 16 uncertain plants
lmiterm([1 1 1 P],A1,1,'s'); lmiterm([1 1 1 Y],-B1,1,'s');
lmiterm([1 1 1 0],1);

lmiterm([2 1 1 P],A2,1,'s'); lmiterm([2 1 1 Y],-B2,1,'s');
lmiterm([2 1 1 0],1);

lmiterm([3 1 1 P],A3,1,'s'); lmiterm([3 1 1 Y],-B3,1,'s');
lmiterm([3 1 1 0],1);

lmiterm([4 1 1 P],A4,1,'s'); lmiterm([4 1 1 Y],-B4,1,'s');
lmiterm([4 1 1 0],1);

lmiterm([5 1 1 P],A5,1,'s'); lmiterm([5 1 1 Y],-B5,1,'s');
lmiterm([5 1 1 0],1);

lmiterm([6 1 1 P],A6,1,'s'); lmiterm([6 1 1 Y],-B6,1,'s');
lmiterm([6 1 1 0],1);

lmiterm([7 1 1 P],A7,1,'s'); lmiterm([7 1 1 Y],-B7,1,'s');
lmiterm([7 1 1 0],1);
```

```
lmiterm([8 1 1 P],A8,1,'s'); lmiterm([8 1 1 Y],-B8,1,'s');
lmiterm([8 1 1 0],1);

lmiterm([9 1 1 P],A9,1,'s'); lmiterm([9 1 1 Y],-B9,1,'s');
lmiterm([9 1 1 0],1);

lmiterm([10 1 1 P],A10,1,'s'); lmiterm([10 1 1 Y],-B10,1,'s');
lmiterm([10 1 1 0],1);

lmiterm([11 1 1 P],A11,1,'s'); lmiterm([11 1 1 Y],-B11,1,'s');
lmiterm([11 1 1 0],1);

lmiterm([12 1 1 P],A12,1,'s'); lmiterm([12 1 1 Y],-B12,1,'s');
lmiterm([12 1 1 0],1);

lmiterm([13 1 1 P],A13,1,'s'); lmiterm([13 1 1 Y],-B13,1,'s');
lmiterm([13 1 1 0],1);

lmiterm([14 1 1 P],A14,1,'s'); lmiterm([14 1 1 Y],-B14,1,'s');
lmiterm([14 1 1 0],1);

lmiterm([15 1 1 P],A15,1,'s'); lmiterm([15 1 1 Y],-B15,1,'s');
lmiterm([15 1 1 0],1);

lmiterm([16 1 1 P],A16,1,'s'); lmiterm([16 1 1 Y],-B16,1,'s');
lmiterm([16 1 1 0],1);


%Define LMI constraint [X (R^0.5)Y; Y'(R^0.5) P]>0
lmiterm([-17 1 1 X],1,1);
lmiterm([-17 2 1 -Y],1,R^0.5);
lmiterm([-17 2 2 P],1,1);


%Define constraint P>0
lmiterm([-18 1 1 P],1,1);

LMIs = getlmis;   %LMI system internal description

%Find and set the storage size based on number of uncertain plants
n = decnbr(LMIs);
c = zeros(n,1);

%Objective function
for j=1:n,
    [Pj,Xj,Yj] = defcx(LMIs,j,P,X,Y);
    c(j) = trace(Q*Pj) + trace(Xj);
end

options = [1e-6,0,0,0,0];
[copt,xopt] = mincx(LMIs,c,options);

Pcom = dec2mat(LMIs,xopt,P);   %Find the common P matrix
Ycom = dec2mat(LMIs,xopt,Y);   %Find the common Y matrix

K_LMI16 = Ycom*(inv(Pcom))    %Compute controller K_LMI16
```

Appendix D: Matlab Code for State-feedback Controller K_{LMI8}

```
%Define 8 matrices of the convex polytope
A1 = [0 0 -6.25E+03 0 0; 0 0 6.82E+03 -1.82E+04 0; 6.25E+03 -3.75E+03
0 0 0; 0 5.00E+03 0 -1.67E+03 0; 0 0 0 -1 0];
B1 = [2.40E+05; 4.36E+05; -4.80E+04; 0; 0];

A2 = [0 0 -6.25E+03 0 0; 0 0 6.82E+03 -1.82E+04 0; 6.25E+03 -3.75E+03
0 0 0; 0 5.00E+03 0 -3.33E+03 0; 0 0 0 -1 0];
B2 = [2.40E+05; 4.36E+05; -4.80E+04; 0; 0];

A3 = [0 0 -4.80E+03 0 0; 0 0 9.45E+03 -1.82E+04 0; 4.80E+03 -5.20E+03
0 0 0; 0 5.00E+03 0 -1.67E+03 0; 0 0 0 -1 0];
B3 = [2.96E+05; 5.37E+05; -8.90E+04; 0; 0];

A4 = [0 0 -4.80E+03 0 0; 0 0 9.45E+03 -1.82E+04 0; 4.80E+03 -5.20E+03
0 0 0; 0 5.00E+03 0 -3.33E+03 0; 0 0 0 -1 0];
B4 = [2.96E+05; 5.37E+05; -1.78E+05; 0; 0];

A5 = [0 0 -4.80E+03 0 0; 0 0 9.45E+03 -1.82E+04 0; 4.80E+03 -5.20E+03
0 0 0; 0 5.00E+03 0 -1.67E+03 0; 0 0 0 -1 0];
B5 = [3.02E+05; 5.48E+05; -8.90E+04; 0; 0];

A6 = [0 0 -4.80E+03 0 0; 0 0 9.45E+03 -1.82E+04 0; 4.80E+03 -5.20E+03
0 0 0; 0 5.00E+03 0 -3.33E+03 0; 0 0 0 -1 0];
B6 = [3.02E+05; 5.48E+05; -1.78E+05; 0; 0];

A7 = [0 0 -4.00E+03 0 0; 0 0 1.09E+04 -1.82E+04 0; 4.00E+03 -6.00E+03
0 0 0; 0 5.00E+03 0 -1.67E+03 0; 0 0 0 -1 0];
B7 = [3.75E+05; 6.82E+05; -3.75E+05; 0; 0];

A8 = [0 0 -4.00E+03 0 0; 0 0 1.09E+04 -1.82E+04 0; 4.00E+03 -6.00E+03
0 0 0; 0 5.00E+03 0 -3.33E+03 0; 0 0 0 -1 0];
B8 = [3.75E+05; 6.82E+05; -3.75E+05; 0; 0];


%Define LQR performance index
Q = [0 0 0 0 0; 0 1E-4 0 0 0; 0 0 0 0 0; 0 0 0 1E-4 0; 0 0 0 0 5E+06];
R = 1;


setlmis([]);   %LMI system initialization
```

```
%Define variable matrices
P = lmivar(1,[5 1]);
X = lmivar(1,[1 1]);
Y = lmivar(2,[1 5]);



%Define LMI constraint AP+PA'-BY-Y'B+I<0 for 8 uncertain plants
lmiterm([1 1 1 P],A1,1,'s'); lmiterm([1 1 1 Y],-B1,1,'s');  lmiterm([1
1 1 0],1);

lmiterm([2 1 1 P],A2,1,'s'); lmiterm([2 1 1 Y],-B2,1,'s'); lmiterm([2
1 1 0],1);

lmiterm([3 1 1 P],A3,1,'s'); lmiterm([3 1 1 Y],-B3,1,'s'); lmiterm([3
1 1 0],1);

lmiterm([4 1 1 P],A4,1,'s'); lmiterm([4 1 1 Y],-B4,1,'s'); lmiterm([4
1 1 0],1);

lmiterm([5 1 1 P],A5,1,'s'); lmiterm([5 1 1 Y],-B5,1,'s'); lmiterm([5
1 1 0],1);

lmiterm([6 1 1 P],A6,1,'s'); lmiterm([6 1 1 Y],-B6,1,'s'); lmiterm([6
1 1 0],1);

lmiterm([7 1 1 P],A7,1,'s'); lmiterm([7 1 1 Y],-B7,1,'s'); lmiterm([7
1 1 0],1);

lmiterm([8 1 1 P],A8,1,'s'); lmiterm([8 1 1 Y],-B8,1,'s'); lmiterm([8
1 1 0],1);


%Define LMI constraint [X (R^0.5)Y; Y'(R^0.5) P]>0
lmiterm([-9 1 1 X],1,1);
lmiterm([-9 2 1 -Y],1,R^0.5);
lmiterm([-9 2 2 P],1,1);


%Define constraint P>0
lmiterm([-10 1 1 P],1,1);

LMIs = getlmis;   %LMI system internal description

%Find and set the storage size based on number of uncertain plants
n = decnbr(LMIs);
c = zeros(n,1);

%Objective function
for j=1:n,
    [Pj,Xj,Yj] = defcx(LMIs,j,P,X,Y);
    c(j) = trace(Q*Pj) + trace(Xj);
end

options = [1e-6,0,0,0,0];
[copt,xopt] = mincx(LMIs,c,options);

Pcom = dec2mat(LMIs,xopt,P);    %Find the common P matrix
Ycom = dec2mat(LMIs,xopt,Y);    %Find the common Y matrix

K_LMI8 = Ycom*(inv(Pcom))     %Compute controller K_LMI8
```